UNIVERSITY OF OKLAHOMA
GRADUATE COLLEGE

BARYON CONTENT TO THE OUTSKIRTS OF LOW-TEMPERATURE POOR GALAXY GROUPS

A DISSERTATION
SUBMITTED TO THE GRADUATE FACULTY
in partial fulfillment of the requirements for the
Degree of
DOCTOR OF PHILOSOPHY

By

JENNA NUGENT
Norman, Oklahoma
2019

BARYON CONTENT TO THE OUTSKIRTS OF LOW-TEMPERATURE POOR GALAXY GROUPS

A DISSERTATION APPROVED FOR THE
HOMER L. DODGE DEPARTMENT OF PHYSICS AND ASTRONOMY

BY THE COMMITTEE CONSISTING OF

Dr. Xinyu Dai, Chair

Dr. Richard Henry

Dr. Karen Leighly

Dr. Howard Baer

Dr. Trina Hope

Dedicated to my late father, Dr. Litton Bryan Nugent.

Acknowledgements

This Dissertation is based on a paper authored by myself, with advisor Xinyu Dai and collaborator Ming Sun, called "*Suzaku* Measurements of Hot Halo Emission at Outskirts for Two Poor Galaxy Groups: NGC 3402 and NGC 5129". A previous version of that paper has been posted to the arxiV, will be updated there and then submitted to a journal in the near future. I would like to thank them for their help with this work.

We thank Ewan O'Sullivan for providing the updated *XMM-Newton* and *Chandra* inner temperature profiles of NGC 3402 and for his helpful comments. Also, we appreciate Eric Miller for his assistance in the stray light issue and for answering several questions regarding the inner workings of `Xspec`, `xissim` and `xissimarfgen`. We would also like to thank the anonymous referee for their extremely helpful comments. Furthermore, we thank NASA and the NSF for awarding generous grants that funded this research.

I would like to thank every member of my Committee. Dr. Dai, thank you for being an amazing advisor and for being so patient with me. It's been a long several years and I truly value all the advice and support you've given me. Dr. Henry, thank you for the encouragement and discussions we had about classes and the specialist exam. Dr. Leighly, thank you for your support when I was struggling with anxiety and for the Observational Methods class. Those notes very helpful for this research! Dr. Hope, thank you for being on my committee and for your encouragement as the defense date kept being delayed. Dr. Ronald Kantowski, thank you for staying on my committee as long as you could and for all the help with E&M qual and class questions. Dr. Baer, thank you for agreeing at the last minute to join my committee.

In my time at OU, I gained so many irreplaceable friends and have wonderful memories. Thank you Brent, Paul, Sara, Tom, Sean, Jeremy, Brian, Erin, Elizabeth, Kyra, Evan, James, Scarlet, Shayne, Callie, David, Malia, Dylan and many more! Y'all made this experience so much more fun than it could have been. Rhi, it was great being in the same research group and going on observing runs with you. Thanks for keeping me sane when I had to re-do this project so many times. Hora, it's been great having you as a daughter and Renae, I'm so blessed to have you as a sister in Christ and as a surrogate little sister. You were both invaluable as my time at OU came to a close. Every last one of you helped this Dissertation come to fruition in some way.

OU is also where I met my husband, Tim. What started as friendship and study sessions soon turned into love. This Dissertation would not have been possible without the strength, comfort and patience you provided. You calmed my panic when I had to re-do or completely change some aspect of the analysis and have seen first hand the extreme difficulty of working with *Suzaku* data. Thank you for being so incredibly wonderful and helping make this Ph.D. a reality. I also appreciate the encouragement I received from my in-laws: Ma, Pa, Ben and Adam. In addition, I would like to thank Tim's VT postdoc advisor Dr. Nahum Arav, colleague Dr. Danielle Lucero, grad students Xinfeng and Doyee, and friends Becca, Jon and Yijun for listening to and keeping me motivated. Furthermore, I am forever grateful to my Aunt Mittie and Uncle George, who helped me settle into Norman and were always such a blessing during my time there and afterward.

To my two best friends since middle school, Evanna and Catina, you also contributed greatly to this work. You believed in and supported me through many a phone call about quals, classes, and all the hurdles I've faced in completing this research. The same goes to my closest friends from high school, Lauren and Kristine.

Particularly important to this work and to me are my mother, late father and brother for their loving support all these years. Bran, I've always looked up to your extremely hard working nature and it definitely motivated me to press onward towards this degree. Mama, thank you for the countless encouraging phone calls and being there for each tear-filled rant and small success. You have helped me in every way imaginable and your prayers kept me going. Daddy, I hope I've made you proud. You're the reason I became interested in physics and astronomy in the first place. You opened my eyes to how incredible our Universe is. Hence, I am here because of you. This work is dedicated to you and your memory.

Ultimately, I would not be here without my Creator, the Lord God Almighty. LORD, thank You for giving me the perseverance and mental acuity to complete this endeavor and for creating this fascinating Universe in which we live.

Table of Contents

1 Introduction **1**

2 Observations and Data Reduction **11**

3 Surface Brightness **22**
- 3.1 Direct Subtraction Method . . . 22
- 3.2 Spectral Analysis . . . 23
  - 3.2.1 Modeling Groundwork . . . 23
  - 3.2.2 Extragalactic, Galactic and Non-X-ray Background Modeling . . . 24
  - 3.2.3 Solar Wind Charge Exchange Modeling . . . 25
  - 3.2.4 Group Halo Emission Modeling . . . 29
  - 3.2.5 Spectral Analysis Results . . . 31
  - 3.2.6 PSF Smearing . . . 51
  - 3.2.7 Stray Light . . . 51
  - 3.2.8 Galactic and Extragalactic Background Variance . . . 53

4 Radial Profiles **56**
- 4.1 AtomDB . . . 56
- 4.2 Emission Weighted Radius . . . 56
- 4.3 Gas Temperature . . . 59
- 4.4 Surface Brightness . . . 60
- 4.5 Electron Number Density . . . 67
- 4.6 Entropy . . . 76

5 Mass Determination **84**
- 5.1 Hot Gaseous Halo and Stellar Masses . . . 84
- 5.2 Total Gravitational Mass . . . 88

6 Discussion and Conclusions **92**

7 References **100**

List of Tables

2 Observations and Data Reduction **11**
2.1 Observation Parameters 13

3 Surface Brightness **22**
3.1 Model Emission Lines and Their Candidates 27
3.2 Xspec Background Parameters and Normalizations for Spectral Analysis . 28
3.3 Xspec Group Parameters and Normalizations for Spectral Analysis 50

4 Radial Profiles **56**
4.1 Mean Surface Brightnesses and Electron Number Densities at R_{emw} . . . 66
4.2 2β–Model Fit Parameters 80

5.1 Derived Group Properties 90

6.1 Sun et al. [73] Groups and Properties 99

List of Figures

1 Introduction **1**

1.1 *XMM-Newton* X-ray false color image of the galaxy cluster XLSSC006 overlayed on optical CFHT-LS data. The central purple sphere is the hot gas halo. The small purple spots are background point sources. This composite image is credited to ESA/*XMM-Newton*, CFHT-LS and the XXL Survey. 2

1.2 Baryon fraction as a function of M_{200}, or mass enclosed by r_{200}. Plotted are the measurements from Sakamoto et al. [65], McGaugh [49], Flynn et al. [24], Vikhlinin et al. [79], Gavazzi et al. [29], Walker et al. [82], Stark et al. [72], Sun et al. [73], Dai et al. [18], Anderson & Bregman [3], converted from circular velocity to M_{200}. The blue solid line is the cosmological baryon fraction measured from the CMB, and the black dashed line is the best-fit broken power-law model for baryon losses. 5

1.3 A depiction of *Suzaku*'s orbital path and its altitude. This figure is from the *Suzaku* Technical Description. 6

1.4 Schematic representation of the XRTs onboard *Suzaku*. The view looking down towards the detectors is shown in part (a), whereas (b) illustrates a side view and the path X-rays take in the instrument. This figure is from Mori et al. [54]. 7

1.5 *Top: XMM-Newton* EPIC X-ray observation of USGC S152 (NGC 3402 Group). This figure is credited to Laganá et al. [46]. *Bottom: Chandra* ACIS X-ray observations of NGC 5129 group. This figure is courtesy of Eckmiller et al. [23]. 10

2 Observations and Data Reduction **11**

2.1 ROSAT images for (*a*) NGC 3402 and (*b*) NGC 5129 with overlaid extent of the *Chandra* spectral analysis from Sun et al. [73] (red circles), extent of r_{500} according to the electron number density profiles determined in this work (black circles), the *Suzaku* FOV for observations of the two groups (cyan squares) and their corresponding *Suzaku* background observations (blue squares). The cyan and blue squares are 17.8 arcminutes on each side. 16

2.2 *Suzaku* (*a*) XIS0, (*b*) XIS1 and (*c*) XIS3 3x3 and 5x5 combined formatted images for NGC 3402 outskirts pointing with inclusion and exclusion regions and the COR2 > 6 GV condition applied. 17

2.3 Same as in Figure 2.2, except for the NGC 3402 background pointing. . . 18

2.4 Same as in Figure 2.2, except for the NGC 5129 1st outskirts pointing. . . 19

2.5 Same as in Figure 2.2, except for the NGC 5129 2nd outskirts pointing. . 20

2.6 Same as in Figure 2.2, except for the NGC 5129 background pointing. . . 21

3 Surface Brightness **22**

3.1 Unfolded spectra for NGC 3402 FI off-center target (black) and background (red) observations. The solid lines are the best-fit theoretical model, not folded with the instrument response, while crosses are the corresponding binned spectral data. Bottom panel contains the residuals in units of standard deviation with error bars of 1σ. 33
3.2 Same as in Figure 3.1, except for the BI CCD. 34
3.3 Unfolded spectra for NGC 5129 1^{st} FI off-center target (black) and background (red) observations. The solid lines are the best-fit theoretical model, not folded with the instrument response, while crosses are the corresponding binned spectral data. Bottom panel contains the residuals in units of standard deviation with error bars of 1σ. 35
3.4 Same as in Figure 3.3, except for the BI CCD. 36
3.5 Normalized folded spectra for NGC 3402 FI off-center target (black) and background (red) observations. The solid lines are the best-fit theoretical model, folded with the instrument response, while crosses are the corresponding binned spectral data. Bottom panel contains the residuals in units of standard deviation with error bars of 1σ. 37
3.6 Same as in Figure 3.5, except for the BI CCD. 38
3.7 Normalized folded spectra for NGC 5129 1^{st} FI off-center target (black) and background (red) observations. The solid lines are the best-fit theoretical model, folded with the instrument response, while crosses are the corresponding binned spectral data. Bottom panel contains the residuals in units of standard deviation with error bars of 1σ. 39
3.8 Same as in Figure 3.7, except for the BI CCD. 40
3.9 Unfolded spectra for NGC 3402 off-center target observations, for both FI (black) and BI (red) CCDs. The solid lines are the best-fit theoretical model, not folded with the instrument response, while crosses are the corresponding binned spectral data. Bottom panel contains the residuals in units of standard deviation with error bars of 1σ. 41
3.10 Same as in Figure 3.9, except for the background observations. 42
3.11 Unfolded spectra for NGC 5129 1^{st} off-center target observations, for both FI (black) and BI (red) CCDs. The solid lines are the best-fit theoretical model, not folded with the instrument response, while crosses are the corresponding binned spectral data. Bottom panel contains the residuals in units of standard deviation with error bars of 1σ. 43
3.12 Same as in Figure 3.11, except for the background observations. 44
3.13 Normalized folded spectra for NGC 3402 off-center target observations, for both FI (black) and BI (red) CCDs. The solid lines are the best-fit theoretical model, folded with the instrument response, while crosses are the corresponding binned spectral data. Bottom panel contains the residuals in units of standard deviation with error bars of 1σ. 45
3.14 Same as in Figure 3.13, except for the background observations. 46

3.15 Normalized folded spectra for NGC 5129 1^{st} off-center target observations, for both FI (black) and BI (red) CCDs. The solid lines are the best-fit theoretical model, folded with the instrument response, while crosses are the corresponding binned spectral data. Bottom panel contains the residuals in units of standard deviation with error bars of 1σ. 47
3.16 Same as in Figure 3.15, except for the background observations. 48
3.17 Representations of stray light and normal reflection. The angle τ defines the "oblique angle of the primary reflector measured from the optical axis of the XRT"[54]. This figure is from Mori et al. [54]. 52

4 Radial Profiles **56**

4.1 *Chandra* projected temperature data from the AtomDB version prior to 2.0.2 (black squares) and post 2.0.2 (magenta diamonds) with their 1σ uncertainties. 57
4.2 Projected SB data lying beyond the radii that our *Suzaku* outskirts observations begin (black squares), the SBs obtained from our spectral analysis (red crosses and blue triangles for FI and BI CCDs, respectively) and their 1σ uncertainties, located at the pre-weighted observation center. Black lines are power-law fits to these data. 63
4.3 Projected temperature profiles with 1σ uncertainties in k_BT and emission weighted radial binsizes overlayed. Black squares are *Chandra* data retrieved from Sun et al. [73] and adjusted to AtomDB ver. 2.0.2, blue asterisks are projected XMM-Newton data (Ewan O'Sullivan, private communication) and red crosses are our *Suzaku* values. 64
4.4 Projected surface brightness profiles with 1σ uncertainties in SB and emission weighted radial binsizes overlayed. Black squares are *Chandra* data, while red crosses and blue triangles are our *Suzaku* FI and BI data, respectively. Note the surface brightness has not been divided by the effective area of the telescope, which is energy dependent. 65
4.5 Single β–model fits (black lines) to the deprojected *Chandra* data from Sun et al. [73]. 70
4.6 2β–model fits to the projected *Chandra* data (black squares) from Eckmiller et al. [23] plus our *Suzaku* data (red crosses). Red and blue dashed lines are the first and second β model components, respectively, while black is the sum of the two. 78
4.7 Quadratic fits (red dashed lines) to the 2β–model parameters (black solid lines) represented via their $\Delta\chi^2$ value over the 5-dimensional grid, from which their 1σ uncertainties were derived. 79
4.8 Sun et al. [73] n_e data (black squares) and our *Suzaku* data (red crosses) with radial bin-sizes plotted. The black line is the constrained fit to the data used to make the calibration, whereas the red and blue dashed lines are the un-calibrated and calibrated profiles for the full SB data set (Eckmiller et al. [23] and *Suzaku*), respectively. 81
4.9 Normalized probability distributions of the partial quantity for n_e described in Chapter 4.5 at r_{emw}. 82

4.10 Entropy profiles in which black squares are Chandra data from Sun et al. [73] (adjusted to the recent version of AtomDB) and red crosses are our *Suzaku* data with radial binsizes overlayed. The solid black lines are power-law fits to the data, whereas the dashed blue lines are the self-similar models as discussed in Chapter 4.6. 83

5.1 Normalized probability distributions of the partial quantity used to obtain the gas mass. 85
5.2 Composite J-H-K_s images of the groups' central galaxies. 88
5.3 Normalized probability distributions of the partial quantity used to obtain the total mass (in solar mass/eV). 91

6 Discussion **92**

6.1 Bolometric X-ray luminosity (0.1–100 keV) plotted versus global gas temperature for NGC 3402 and NGC 5129, along with their 1σ uncertainties. Also plotted are various L_X–T relations from the literature, corrected for our cosmology. 93
6.2 Baryon fraction as a function of M_{200}, or mass enclosed by r_{200}. Plotted are the measurements from Sakamoto et al. [65], McGaugh [49], Flynn et al. [24], Vikhlinin et al. [79], Gavazzi et al. [29], Walker et al. [82], Stark et al. [72], Sun et al. [73], Dai et al. [18], Anderson & Bregman [3] and this work, converted from circular velocity to M_{200}. The blue solid line is the cosmological baryon fraction measured from the CMB and the black dashed line is the best-fit broken power-law model for baryon losses. . . . 96
6.3 Baryon fraction out to r_{500} versus temperature, plotted for five galaxy groups with global gas temperatures less than 1.3 keV and whose baryon fractions were determined within $r \geq 0.62\, r_{500}$. The solid blue region is the Bayesian averaged f_b and 1σ uncertainty, whereas the red crosses are the results from this work and black squares are the data from Sun et al. [73]. 97

Abstract

We present *Suzaku* off-center observations of two poor galaxy groups, NGC 3402 and NGC 5129, with temperatures below 1 keV. Through spectral decomposition, we measured their surface brightnesses and temperatures out to 530 and 1430 times the critical density of the universe for NGC 3402 and NGC 5129, respectively. These quantities are consistent with extrapolations from existing inner measurements of the two groups.

With the refined bolometric X-ray luminosities, both groups prefer L_X–T relations without a break in the group regime.

Furthermore, we have determined the electron number densities and hydrostatic masses at these radii. We found that the surface brightness and electron number density profiles require two β model components, as well as the indication that a third β model may be needed for NGC 3402.

Adding the gas mass measured from the X-ray data and stellar mass from group galaxy members, we computed baryon fractions of $f_b = 0.0693 \pm 0.0068$ and $f_b = 0.095 \pm 0.014$ for NGC 3402 and NGC 5129, respectively.

Combining other poor groups with well-measured X-ray emission to the outskirts, we found an average baryon fraction extrapolated to r_{500} of $\overline{f_{b,500}} = 0.0912 \pm 0.0050$ for X-ray bright groups with temperatures between 0.8–1.3 keV, extending existing constraints to lower mass systems and indicating that significant baryon losses exist below approximately r_{500}.

Chapter 1

Introduction

Galaxy clusters are the most massive gravitationally bound structures in the Universe, consisting of between 50 to well over 1,000 member galaxies. Their composition includes cold and hot gas, stars, and dark matter. The three aforementioned quantities excluding dark matter are the clusters' main baryonic components. In the astrophysical community, baryonic matter is considered to be protons, neutrons, and all matter derived from them, including black holes. This material can interact via the electromagnetic force. However, dark matter does not and is therefore invisible. Together, the dark and baryonic components combine to produce the total dynamical mass of galaxy clusters. This mass under dynamical equilibrium has been measured for clusters to be approximately $10^{14} - 10^{15} M_{\odot}$, where $M_{\odot}$ is the mass of the Sun.

Hot gas comprises a large percentage of the baryon content in clusters and has temperatures on the order of a few 10^7 to greater than 10^8 Kelvin [56], or between about two to over 10 keV [60]. In the X-ray community, temperatures are generally stated in keV, which we have adopted here. In clusters, the hot gas is a thermal plasma and mainly emits through bremsstrahlung continuum radiation, in which electrons are accelerated by the electric field of protons or atomic nuclei and emit X-ray photons as a result. Line emission is also present but less dominant due to the extremely ionized hot gas. Figure 1.1 illustrates the hot gas halo of a galaxy cluster as imaged by the X-ray telescope *XMM-Newton*.

On the other hand, galaxy groups contain less than 50 galaxies and, while they have the same types of matter as in clusters, they harbor relatively less hot gas. As expected, they also have lower total masses, around $10^{13} - 10^{14} M_{\odot}$ and gas

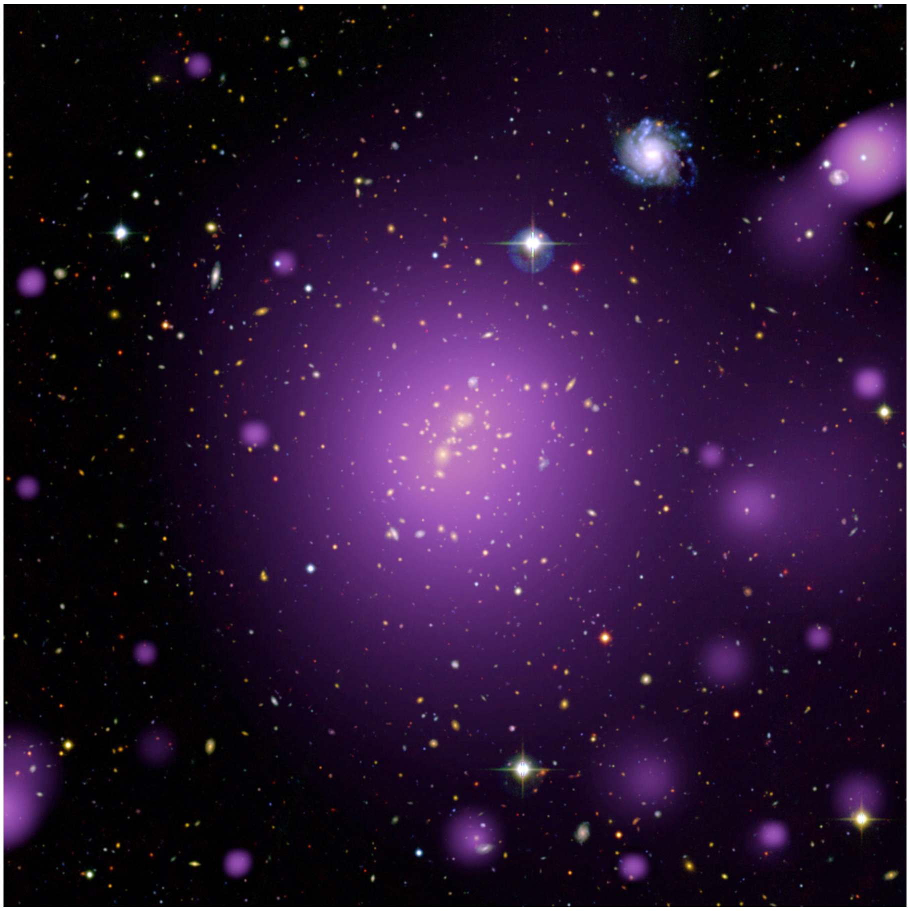

Fig. 1.1.— *XMM-Newton* X-ray false color image of the galaxy cluster XLSSC006 overlayed on optical CFHT-LS data. The central purple sphere is the hot gas halo. The small purple spots are background point sources. This composite image is credited to ESA/*XMM-Newton*, CFHT-LS and the XXL Survey.

temperatures of $k_B T \lesssim 2$ keV [74]. Since their temperatures are so low, the majority of X-rays come through line emission from excited atoms. This is in opposition to the bremsstrahlung that dominates in hotter clusters, though it is still present to a lesser extent in groups. Furthermore, galaxy groups can be classified as “poor”, which are groups that usually contain less than five bright galaxies. Specifically, “bright” refers to galaxies with absolute magnitudes in the B-band less than M_B^* [87], which is the magnitude corresponding to the luminosity break of the Schechter luminosity function. These low-temperature, poor groups are the focus of this work.

Both galaxy clusters and groups are virialized over-density regions in the Universe. This means the galaxies that merged to form the cluster or group have finished previous merging activity and are stable, abiding by the virial theorem. When discussing galaxy groups and clusters, properties and quantities are generally given by their over-density with respect to the critical density of the Universe, ρ_{crit}. This means these radii or derived properties contain an average mass density that is some constant times the critical density. For instance, one common radius out to which these systems are measured is r_{500}, or where $\rho_{ave} = 500\rho_{crit}$. Thus, as the over-density constant decreases, the radial extent of the measurement increases.

Based on numerical or semi-analytical simulations (e.g., Bryan & Norman [13]), the over-density of clusters and groups in the virial radius, r_{vir}, is approximately 100 times the critical density of the Universe for the prevailing concordance cosmology. However, observations are more easily able to probe the central regions within $\sim r_{2500}$, which limits us from understanding the overall properties of these objects, such as their virial masses, temperatures and gas and stellar contents. Therefore, measuring cluster and group properties at their outskirts close to the virial radius becomes a major endeavor. For galaxy clusters, successful measurements of the X-ray emission near r_{200} have been made with *Suzaku* for many individual clusters [e.g., 1, 7, 26, 30, 34, 39, 42, 63, 67, 70, 83] and by using stacking analysis [17, 18, 22, 64, 69]. Yet for galaxy groups, it is more difficult to study the X-ray emission at large radii because of the relatively weaker emission. The situation is especially severe for poor groups with temperatures below $k_BT \lesssim 1$ keV, where only measurements from stacking analysis and very few individual systems exists for these groups [4, 17, 73].

Galaxy groups are important to study the properties of virialized structures, especially to test the deviations from self-similar model predictions, such as the L_X–T relation. Scaling relations, or the empirical relations between system properties, are extremely useful for better understanding the physics of various types of objects and can be used to perform simulations, e.g., Truong et al. [77] and Kravtsov et al.

[43]. Since there are very few measurements out to large radii for poor groups, the nature of these relations at lower mass ranges is not well known. More accurate measurements in the group regime will extend the mass range for these tests.

Groups of galaxies are also important to better quantify the missing baryon problem in the low-redshift universe (Bregman [11] and references therein), in which the observed amount of baryons is less than that determined based on the cosmic microwave background (CMB) observed from the early universe. We know this by comparing the fraction of baryonic to total matter that has been obtained for both high redshift cosmic microwave background studies and nearby, low redshift surveys of galaxies, galaxy groups and clusters. According to the 3-year WMAP data, which we assume in this work, the baryon fraction, or the ratio of baryonic to total gravitational matter, is $f_b = \Omega_b/\Omega_m = 0.175$ for $\Omega_m = 0.26$ and $\Omega_\Lambda = 0.74$. Here Ω is the dimensionless parameter representing the ratio of mass or energy density to critical density for each component of the Universe. While observations of nearby galaxies yielded only about 10% of the expected baryon content, [e.g., 12, 27, 61], observations of rich galaxy clusters with $k_B T > 5$ keV retain the cosmological value after adjusting for stellar mass [79].

Illustrated by Figure 1.2, we can see that the observed baryon fraction of nearby systems as a function of gravitational potential well follows a broken power-law model [18, 19]. In this case, we represent gravitational potential well as the total mass within r_{200}, which is the conventional choice. The data for all but the most massive objects fall below the cosmological fraction measured at high redshift. The group regime is arguably the transition region, where baryon loss becomes significant. However, we lack sufficient data to well define the mass threshold of the baryon loss due to difficulties in accurately measuring their properties, especially to the outskirts. These missing baryons are theorized to be in a warm-hot intergalactic

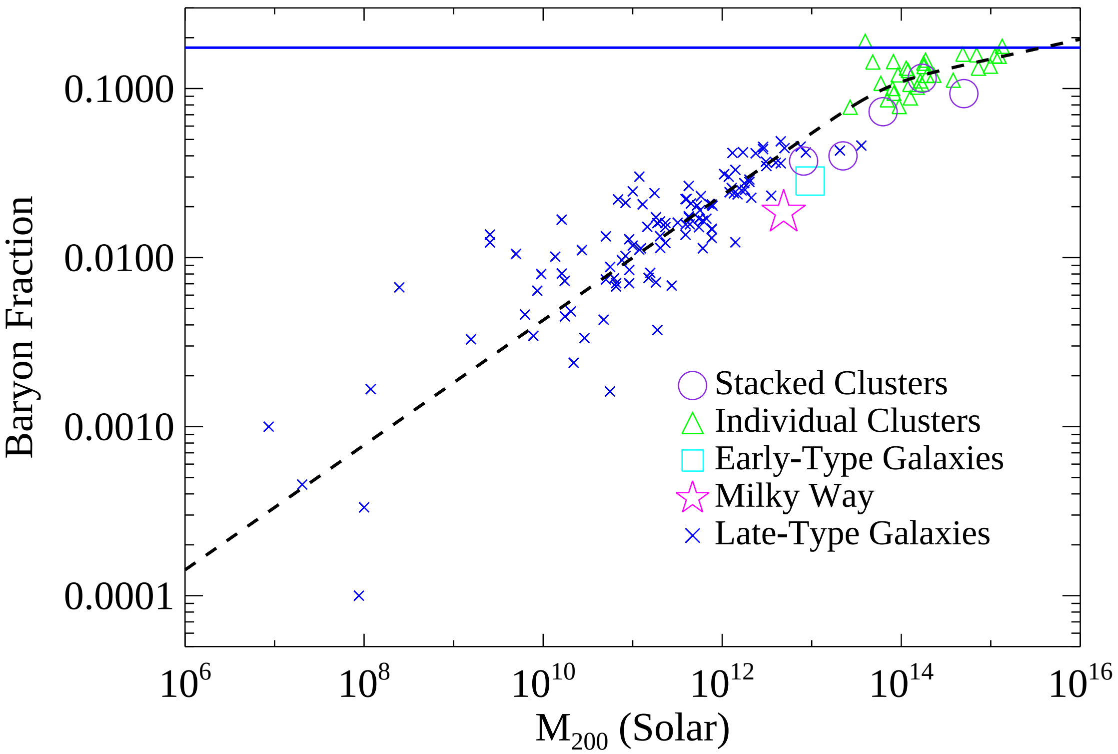

Fig. 1.2.— Baryon fraction as a function of M_{200}, or mass enclosed by r_{200}. Plotted are the measurements from Sakamoto et al. [65], McGaugh [49], Flynn et al. [24], Vikhlinin et al. [79], Gavazzi et al. [29], Walker et al. [82], Stark et al. [72], Sun et al. [73], Dai et al. [18], Anderson & Bregman [3], converted from circular velocity to M_{200}. The blue solid line is the cosmological baryon fraction measured from the CMB, and the black dashed line is the best-fit broken power-law model for baryon losses.

medium (WHIM), which permeates the large scale structure filaments of the Universe and hot gas halos of galaxy clusters and groups. Recent work has strongly supported this hypothesis, e.g., Nicastro et al. [57].

Although this general picture is likely correct, some key questions still remain ambiguous, such as how virialized regions of various galactic systems lose their baryons (such as through feedback processes), or if the missing baryons of galaxies and galaxy groups were suppressed from falling into their hot gaseous halos altogether. Answering these questions will guide the development of numerical simulations with non-gravitational processes such as feedback and pre-heating, e.g., Benson [10]. In the pre-heating model, the gas never fell into the systems due to a significant warming phase, such as baryons shock heating on the dark matter halo. On the other hand, the feedback model posits that the baryons were driven out as a wind, for instance, by AGN or supernovae [10]. Distinguishing between these models is an area of strong interest in the astrophysics community.

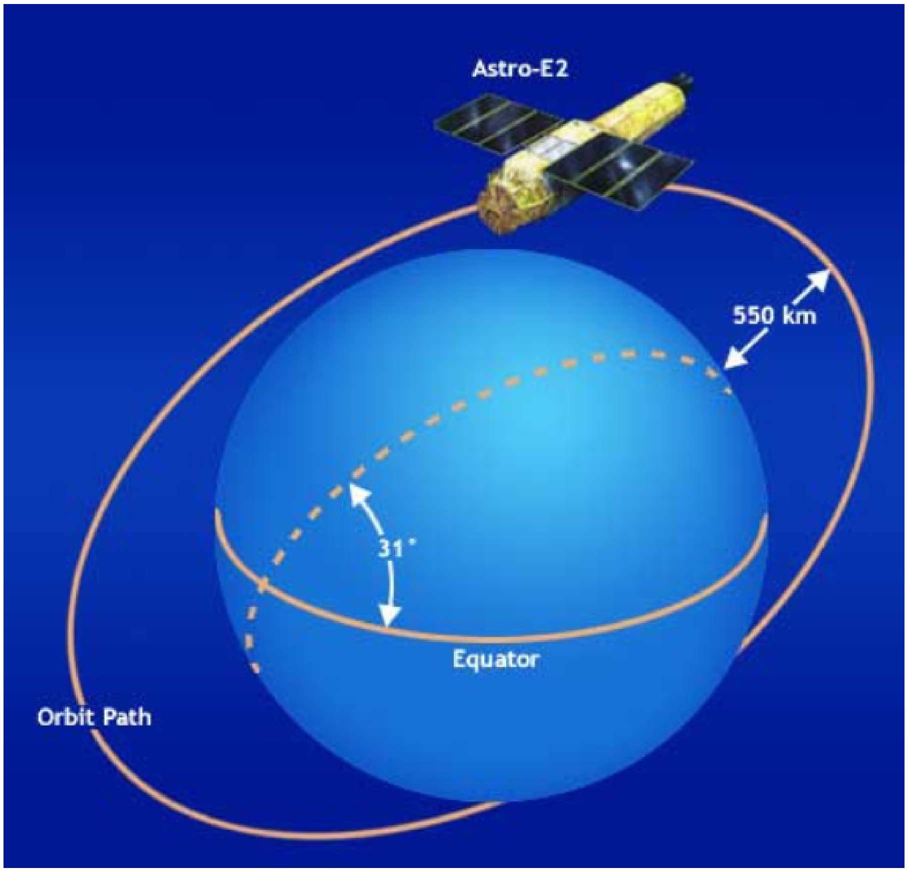

Fig. 1.3.— A depiction of *Suzaku*'s orbital path and its altitude. This figure is from the *Suzaku* Technical Description.

In this work, we observed the diffuse, extended emission from two poor galaxy groups in the soft X-ray band with *Suzaku* (previously Astro-E2), which is best for such observations due to its low, stable background resulting from its low-earth orbit (Figure 1.3). Now decommissioned, *Suzaku* was an X-ray observatory specifically designed with the capability to study diffuse, low surface brightness objects. This is because its low altitude orbit increased sensitivity by taking advantage of the shielding effect Earth's magnetic field has against background cosmic rays. We analyzed observations made using the X-ray Telescopes (XRTs), which focused the emission onto CCD detectors, the X-ray Imaging Spectrometers (XISs). Since the emission is so high energy, the XRTs were comprised of nested mirrors which focus the X-rays through double reflection at grazing-angle incidence, a schematic of which is given in Figure 1.4. At this point, the emission becomes focused onto the XISs. The field of view (FOV) for each detector is 17.8 by 17.8 square arcminutes on the sky. See the *Suzaku* Technical Description and Chapter 2 of this work for more details.

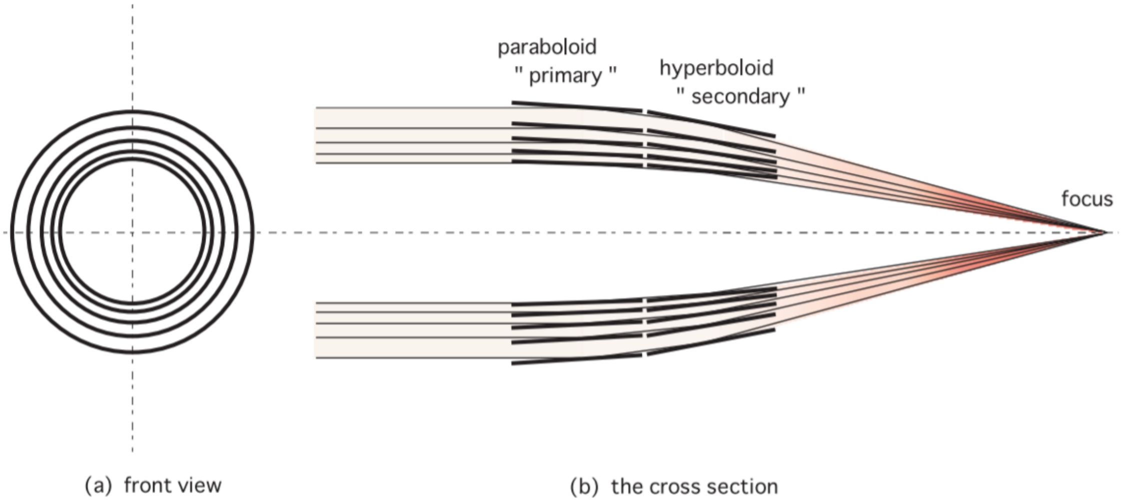

Fig. 1.4.— Schematic representation of the XRTs onboard *Suzaku*. The view looking down towards the detectors is shown in part (a), whereas (b) illustrates a side view and the path X-rays take in the instrument. This figure is from Mori et al. [54].

The two groups extensively studied in this paper and many of their properties are well documented in the literature. For instance, NGC 3402 Group, also called SS2b153, NGC 3411 Group and USGC S152, appears to be perfectly round, containing "no evidence of irregularity" [48] and is believed to have between four and five member galaxies [31, 48]. This nearby ($z = 0.0153$) group has a global temperature, $k_BT = 0.88 \pm 0.04$ keV [73]. All global temperatures mentioned in this work have been adjusted for the significant change in AtomDB, as discussed in Chapter 4.3. NGC 3402 is the central giant elliptical galaxy of this group, classified as a cD galaxy. Accordingly, the group has been labeled a fossil group, which is believed to be the remnant of a series of galaxy mergers resulting in a dominant, bright elliptical galaxy surrounded by few, much less luminous galaxies [41].

Illustrated in Figure 1.5, we can see that the *XMM-Newton* image for NGC 3402 Group indeed appears quite spherical and uniform. That makes this group especially interesting due to its peculiarly shaped temperature profile [59], given its seemingly relaxed nature. We will further address this temperature profile in Chapter 4.3.

Although NGC 5129 Group has nearly the same global temperature as NGC 3402 Group, $k_BT = 0.90 \pm 0.04$ keV [73], it is a less nearby ($z = 0.0230$) loose group with approximately 19 member galaxies [47]. The term "loose" means the galaxies are separated by greater than several galactic radii on the sky [32]; our Local Group is considered loose as well. Also shown in Figure 1.5 are X-ray observations of NGC 5129 Group, in this case using the *Chandra* ACISs. Though different in some ways, both groups lie in the temperature range that so far has a dearth of successful measurements. This is especially true for their outskirts, hence the need for our *Suzaku* observations.

Throughout this work, we adopt the 3-year WMAP cosmology and a flat universe: $H_0 = 73$ km s^{-1} Mpc^{-1}, $\Omega_m = 0.26$ and $\Omega_\Lambda = 0.74$. Beyond this Introduction, Chapter 2 provides details on the observations, as well as the extensive data reduction we performed on these groups. Next, the process by which we determined the surface brightnesses through spectral analysis is detailed in Chapter 3. Also, numerous radial profiles are plotted and the process of obtaining our contribution to them is explained in Chapter 4. Moreover, several mass quantities later used to determine various mass fractions are established in Chapter 5. Finally, in Chapter 6 we discuss our findings and summarize their larger implications.

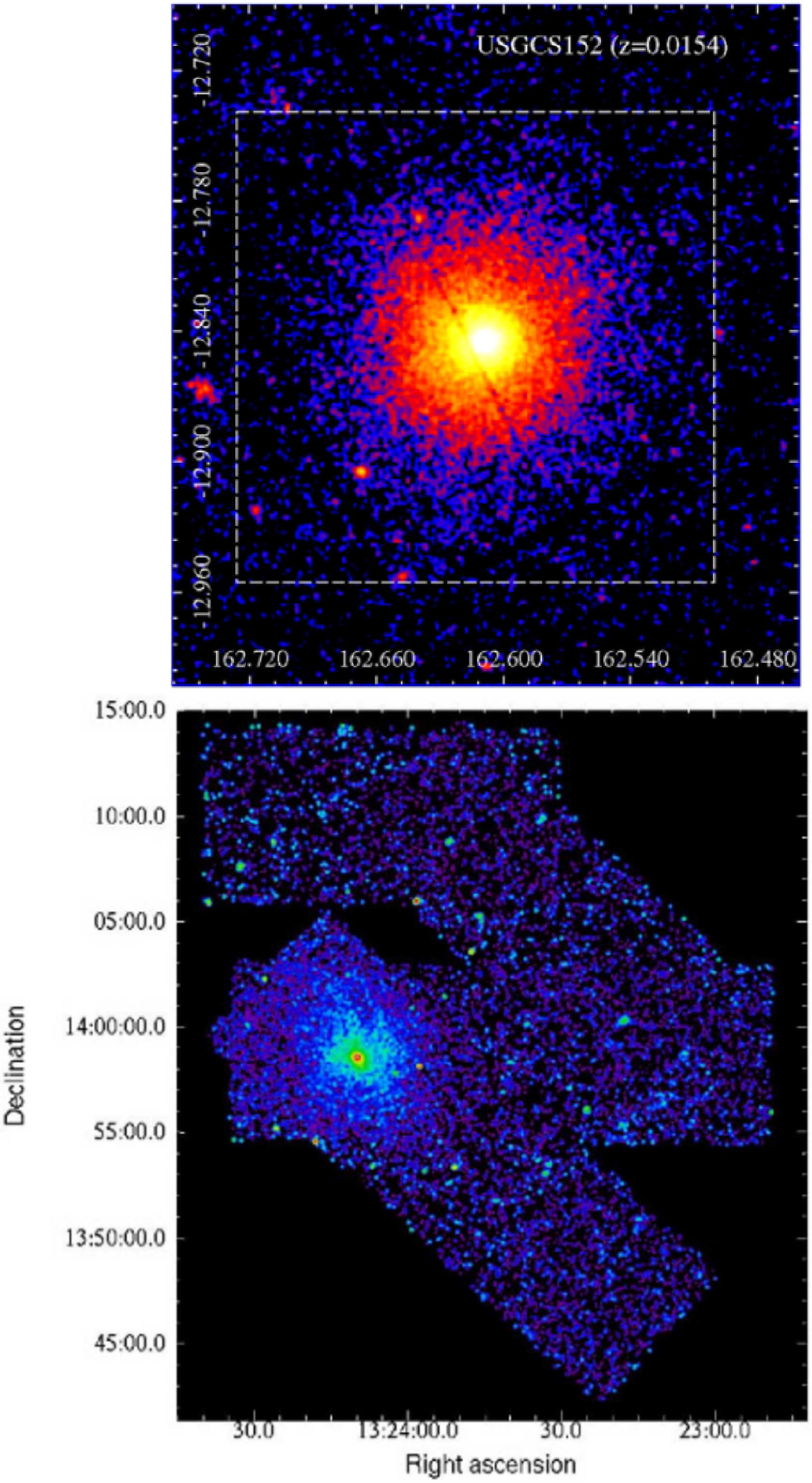

Fig. 1.5.— *Top: XMM-Newton* EPIC X-ray observation of USGC S152 (NGC 3402 Group). This figure is credited to Laganá et al. [46]. *Bottom: Chandra* ACIS X-ray observations of NGC 5129 group. This figure is courtesy of Eckmiller et al. [23].

Chapter 2

Observations and Data Reduction

Observations were obtained of the poor fossil group, NGC 3402 Group (hereafter NGC 3402), centered at 22.1 arcminutes (r_{475}) away from the group X-ray center with the position angle (PA) of 108° in the X-ray band using *Suzaku* on 2010 December 27 for 49 ks. Also with *Suzaku*, we observed the poor loose group, NGC 5129 Group (hereafter NGC 5129), using two off-center pointings with separations from the group X-ray center of 16.2 and 15.3 arcminutes (farther at r_{420}). This was performed on 2010 December 18 with PAs of 78° and 161° and exposure times of 55 ks and 38 ks, respectively. These off-center observations are also referred to as target or outskirts observations in this work. Additionally, to better model the background, we performed one background pointing for each galaxy group at $2.04r_{200}$ and $2.14r_{200}$ for NGC 3402 and NGC 5129, respectively. The two background observations were carried out within 10 days of the corresponding target observations to ensure no significant time variability had occurred in the X-ray background between them.

All five observations were taken using the three remaining X-ray Imaging Spectrometers (XISs) onboard *Suzaku*: two front-illuminated (FI) CCDs (XIS0 and XIS3) and one back-illuminated (BI) CCD (XIS1). Details of these observations are listed in Table 2.1. Also, ROSAT images of each group are depicted in Figure 2.1, where the radial extent of the *Chandra* analysis from Sun et al. [73], the extent of r_{500} based on the electron number density profiles discussed later in this work, and the *Suzaku* FOV for the group and background observations are shown. In part (b) of Figure 2.1, the northern observation is what we have designated NGC 5129 1^{st}, whereas the southern observation is NGC 5129 2^{nd}. From this, we can see that the center of each group pointing lies beyond r_{500} and a significant area of NGC 5129 is analyzed due to its two spatially separate pointings. Here both the cyan and blue squares are 17.8 arcminutes on each side, representing the FOV of *Suzaku*.

Table 2.1. Observation Parameters

Observation	Obs. ID	Date	RA(J2000) deg	Dec (J2000) deg	Raw/Final Exposure Time(ks)[a]		
					XIS0	XIS1	XIS3
NGC3402	805070010	2010/12/27	162.4923	−13.1954	49.4/24.1	49.2/24.1	49.4/24.1
NGC3402back	805071010	2010/12/19	161.6656	−13.5535	15.2/12.5	15.1/12.5	15.3/12.5
NGC5129 1st	805072010	2010/12/18	201.3141	14.0346	55.4/25.6	53.5/25.6	55.8/25.6
NGC5129 2nd	805073010	2010/12/18	201.1253	13.7341	37.9/25.4	37.7/25.3	37.9/25.4
NGC5129back	805074010	2010/12/17	201.7433	13.5725	16.4/12.3	15.8/12.3	16.5/12.3

[a] Final exposure times after all screening, including the COR2 $>$ 6 GV condition.

The data were reduced using the software package *HEAsoft* version 6.13. First, we reprocessed the data using the FTOOL `aepipeline`, which also performs default screening, along with the XIS calibration database (20120210). All data were reduced according to *The Suzaku Data Reduction Guide*[b]. Additionally, we excluded times when the revised cut-off rigidity value (COR2) was less than 6 GV to improve the signal-to-noise (S/N) ratio by reducing instances of background flaring. These are times in which the satellite passes through regions where the geomagnetic field is weak and they are calculated in part based on the position of *Suzaku* [76].

Then, we removed resolved foreground and background X-ray sources, as well as the ^{55}Fe calibration sources located at two corners of each detector (Figures 2.2 through 2.6). The locations of the calibration sources were known and the remaining sources were excised by visual inspection. Furthermore, most likely due to a micrometeorite impact, a strip of the XIS0 detector (located at DETX = 70–150) was deemed unusable by the XIS team[c]. Following their notes for reducing XIS0 data after this anomaly[d], we used a C-shell script to generate a region to remove all events in the affected area and formed a region to remove possible spurious sources near this strip. This was applied to the XIS0 CCDs for all observations. The top images of Figures 2.2–2.6 illustrate these sources and their regions for the XIS0 3x3 and 5x5 combined observations. Here the 3x3 and 5x5 distinctions are editing modes specifying the telemetry format.

Next, we examined these observations' light curves using `Xselect` for instances of background flaring in the 0.5–8 keV band after the above screening processes. The only light curves that seemed to indicate any flaring were from the BI CCD (XIS1). Since our analysis is focused solely on the soft X-ray band, we filtered those spectra further by the energy band used later on in the spectral analysis: 0.5–5 keV

---

[b] http://heasarc.gsfc.nasa.gov/docs/suzaku/analysis/abc/abc.html

[c] http://www.astro.isas.ac.jp/suzaku/doc/suzakumemo/suzakumemo-2010-01.pdf

[d] http://www.astro.isas.jaxa.jp/suzaku/analysis/xis/xis0_area_discriminaion

[39]. The resultant curves show no flaring in that energy range. Thus, the light curves in the energy bands of interest are not contaminated by background flaring. Therefore, no significant background flares were found in any observations.

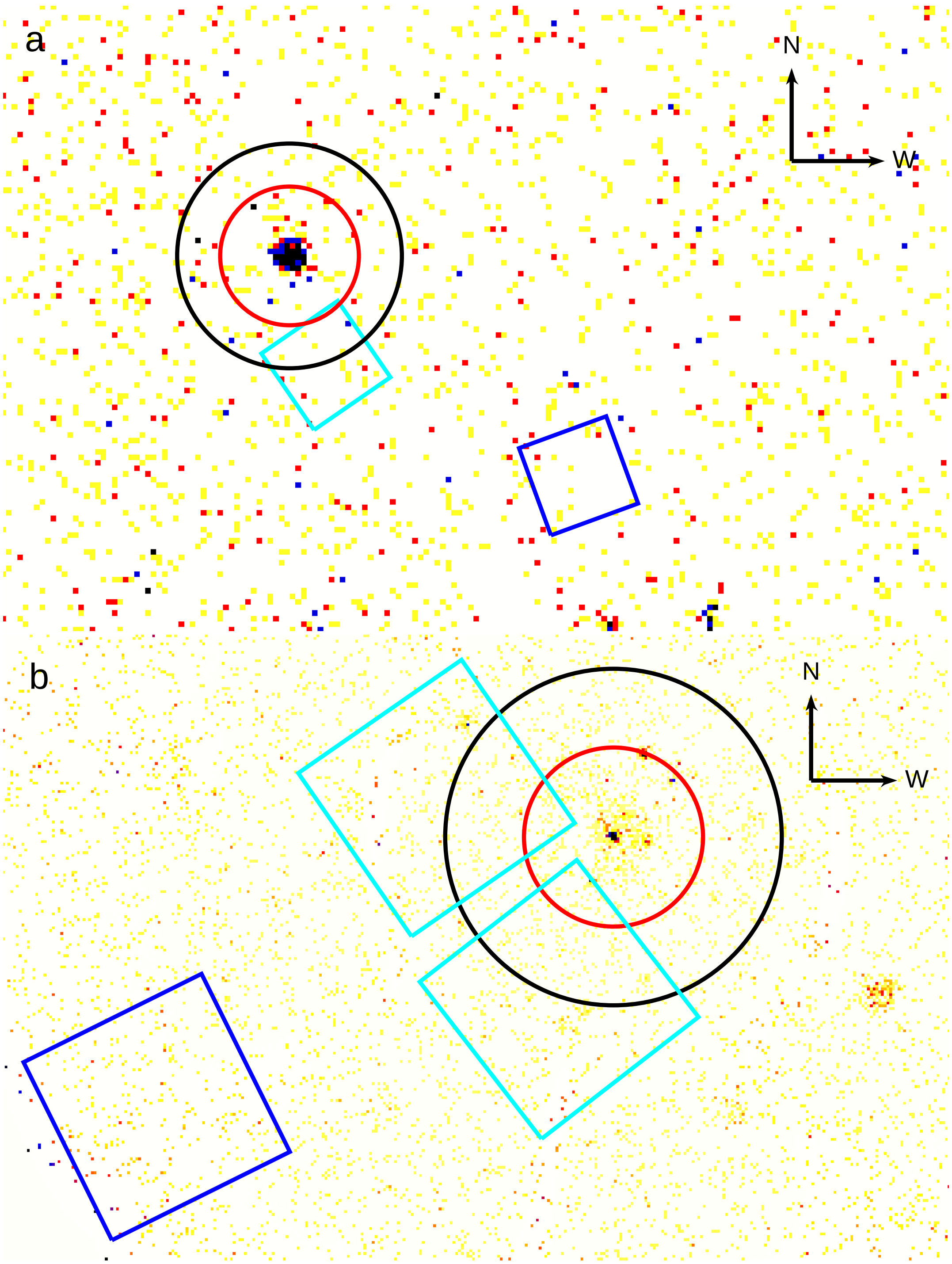

Fig. 2.1.— ROSAT images for (*a*) NGC 3402 and (*b*) NGC 5129 with overlaid extent of the *Chandra* spectral analysis from Sun et al. [73] (red circles), extent of r_{500} according to the electron number density profiles determined in this work (black circles), the *Suzaku* FOV for observations of the two groups (cyan squares) and their corresponding *Suzaku* background observations (blue squares). The cyan and blue squares are 17.8 arcminutes on each side.

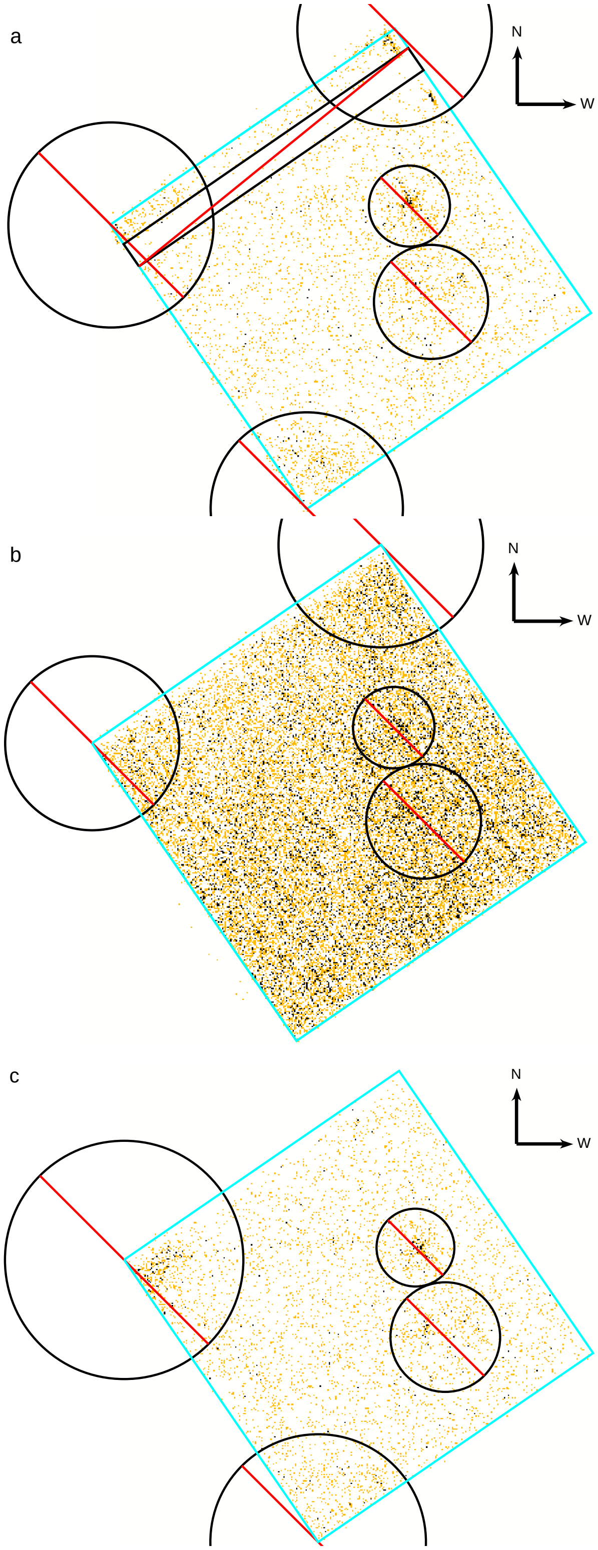

Fig. 2.2.— *Suzaku* (*a*) XIS0, (*b*) XIS1 and (*c*) XIS3 3x3 and 5x5 combined formatted images for NGC 3402 outskirts pointing with inclusion and exclusion regions and the COR2 > 6 GV condition applied.

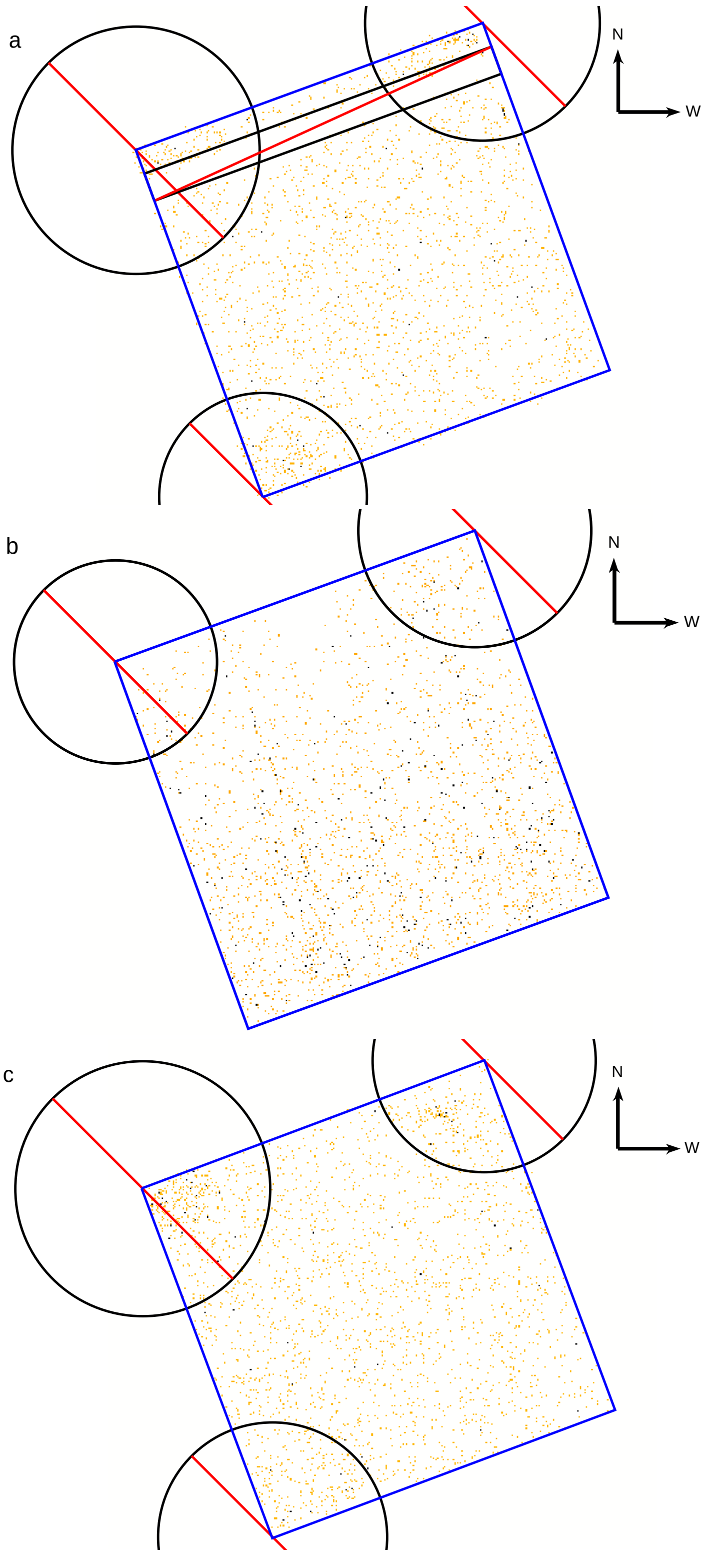

Fig. 2.3.— Same as in Figure 2.2, except for the NGC 3402 background pointing.

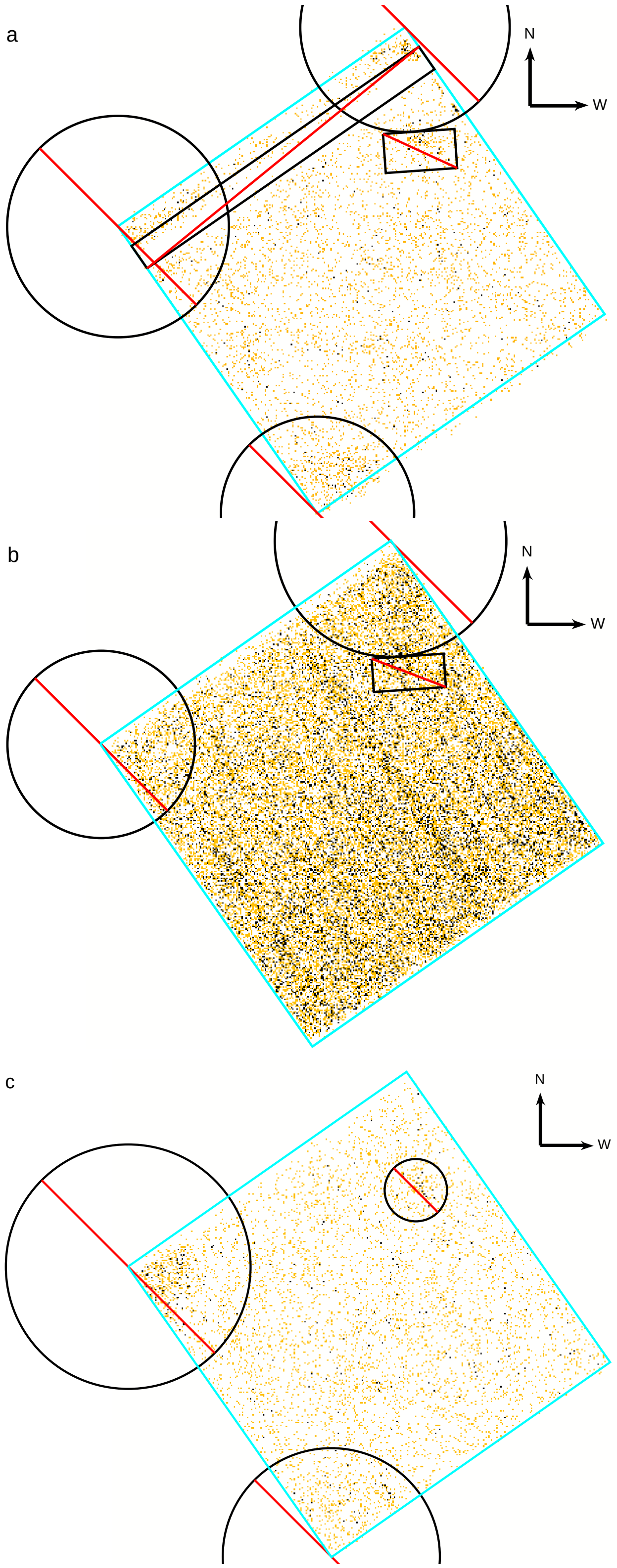

Fig. 2.4.— Same as in Figure 2.2, except for the NGC 5129 1st outskirts pointing.

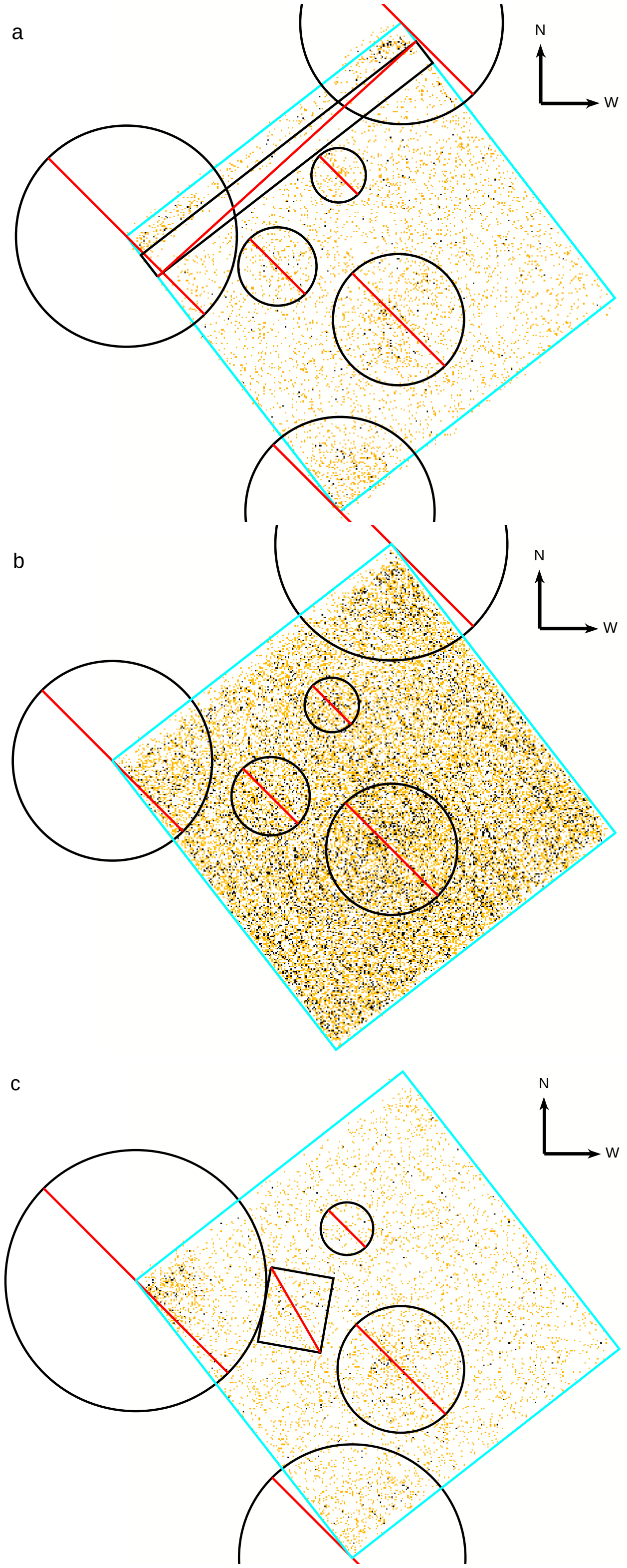

Fig. 2.5.— Same as in Figure 2.2, except for the NGC 5129 2nd outskirts pointing.

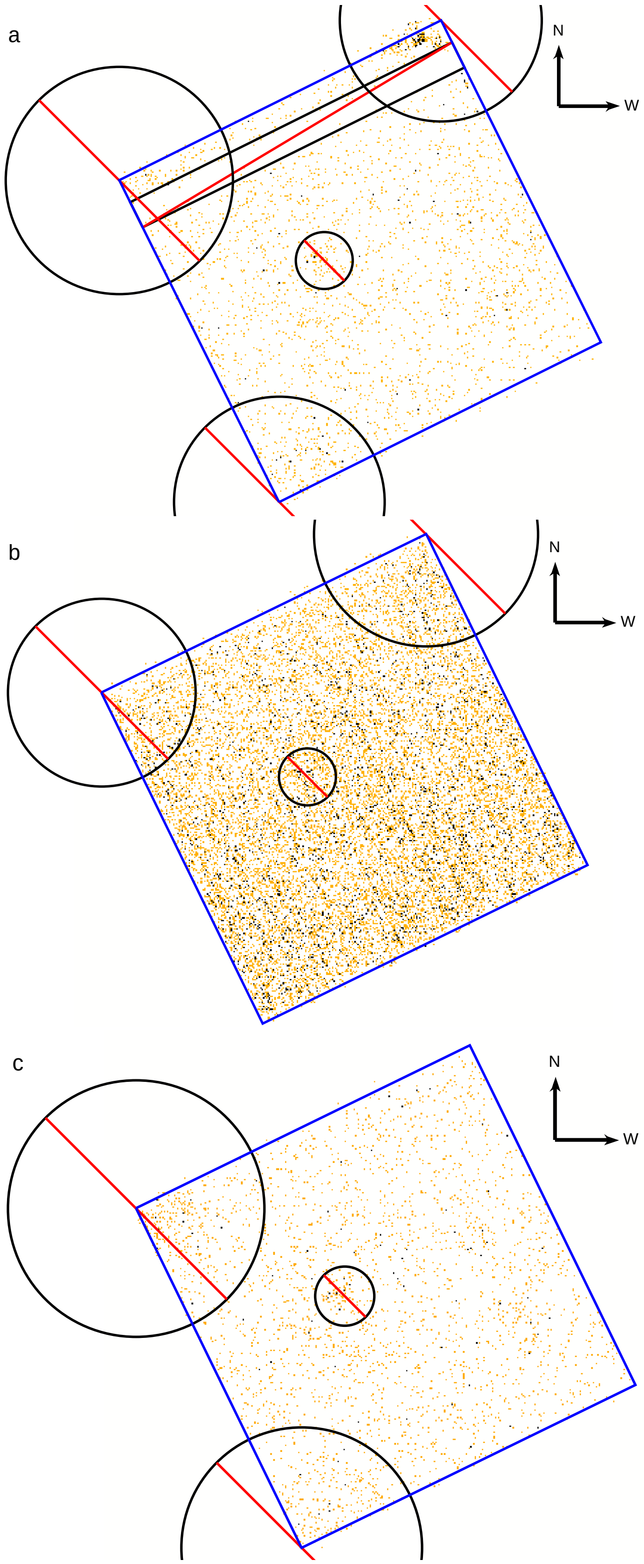

Fig. 2.6.— Same as in Figure 2.2, except for the NGC 5129 background pointing.

Chapter 3

Surface Brightness

Two methods were employed to measure the mean surface brightness (SB) for each target. First is the direct subtraction method, since there are background observations at greater than $2.04r_{200}$ performed within 10 days of each target observation enabling the non-X-ray background to be measured well. In this method, the SB is computed for both the target and their corresponding background observations and the net value is the difference between the two and is one way to perform imaging analysis. The second method involves modeling the spectra of both the target and background observations, and the surface brightness is determined from the best-fit model parameters for the group emission.

3.1 Direct Subtraction Method

Using version 2.4b of `Xselect`, we read in both the 3x3 and 5x5 event files with the COR2 $>$ 6 GV screening for each CCD and extracted the total events for each observation in the 0.6–1.3 keV energy range, excluding the resolved X-ray, calibration and anomalous sources mentioned in Chapter 2. The 0.6–1.3 keV range was chosen based on simulations of the expected group halo emission. Then, mean surface brightnesses for both the group and background pointings were calculated. Since the group emission is extended and much larger than the point spread functions (PSFs) of the XISs, the net SB is just the subtraction of the two. For uncertainties, we purely considered Poisson noise. There was no detection of any group emission from this crude analysis. This result is not unexpected for such low temperature and diffuse objects. In our case, the data is much closer to the detection threshold. Hence, a more meticulous analysis is required by utilizing the full spectrum. Spectral analysis enables us to better constrain the background components, which then facilitates extraction of the source emission. For example, the hard energy band allows us to better pin down the AGN (power-law) component. Therefore, we shifted our approach to precisely analyzing the spectra of each group and background pointing.

3.2 Spectral Analysis

3.2.1 Modeling Groundwork

Spectra of each observation were generated using `Xselect` and we binned all spectra with a minimum of 25 photons in each bin using the FTOOL `GRPPHA`. The instrumental response was simulated by generating redistribution matrix files (RMFs) using the XIS response generator `xisrmfgen` ver. 2012-04-21, which include information concerning the quantum efficiency of the detectors [40]. Next, we used the Monte Carlo ray-tracing algorithm `xissimarfgen` ver. 2010-11-05 to produce the ancilliary response files (ARFs), which account for the effective area of each detector. The input GTI files were from the cleaned event files with the COR2 condition applied.

Furthermore, we approximated emission caused by cosmic ray and γ-ray interactions with the telescope's interior by generating the non-X-ray background (NXB) spectra using the tool `xisnxbgen` ver. 2010-08-22, which uses the night-Earth data collected by *Suzaku* [52, 86]. Night-Earth data were accumulated for more than 750 ks for the BI CCD and 1.5 Ms for the FI CCDs, combined. Since XIS0 and XIS3 are both front-illuminated CCDs, we were able to combine their spectra, NXB and response files using `addascaspec`. To avoid systematic uncertainties in the background calibration, all spectra were fit in the energy ranges: 0.6–7 keV for FI CCDs and 0.5–5 keV for the BI CCD [39]. All spectra were modeled with `Xspec` ver. 12.8.0. Also, both the background and group observations' FI and BI spectra were fit simultaneously to improve the constraints on model parameters, since concurrently fitting all spectra maximizes signal-to-noise.

3.2.2 Extragalactic, Galactic and Non-X-ray Background Modeling

The background constituents in both the outskirts and background observations were modeled by several components: NXB, Galactic emission, unresolved extragalactic sources (cosmic X-ray background, CXB) and emission due to solar wind charge exchange (SWCX) [25]. The NXB component was subtracted from each spectrum using the pre-generated NXB spectra discussed in Chapter 3.2.1. To address any possible shortcomings in the NXB generated by `xisnxbgen`, we visually inspected the NXB subtracted binned and unbinned spectra for any significant NXB excess, and added Gaussian lines to model any residual NXB emission lines. All line normalizations were allowed to fit freely during the spectral fits.

Unresolved extragalactic sources, i.e., active galactic nuclei (AGN), were modeled using a power-law (*pow*) component with photon index (Γ) frozen at 1.41 [36]. We accounted for Galactic gas halo emission with one absorbed *apec* thermal plasma model, where the temperature was allowed to be free. Since NGC 5129 is close to the North Polar Spur, which is a section of the Galaxy that has enhanced X-ray emission, we added a second Galactic *apec* component at $k_B T = 0.4$ keV [28, 50, 73]. We used zero redshift and solar abundances for both background *apec* models, where the temperature of the 0.4 keV model was fixed during the spectral analysis. Also, the Galactic and extragalactic components were modified by a *wabs* multiplicative model component to include photo-electric absorption by the Galaxy

[21]. Neutral hydrogen column densities were computed using the default parameters on the web-based N_H tool[d], where we chose the Dickey and Lockman weighted average values. Thus, the NXB-subtracted background model is: *wabs*(pow + apec[free] + apec[0.4]*(for NGC 5129 only)*) + gau*(residual NXB lines), where the normalizations for all model components were treated as free parameters.

We performed simultaneous fits between the FI and BI spectra, since the Galactic, extragalactic and galaxy group emission should correspond between different CCDs. However, the residual NXB line normalizations were allowed to fit independently due to the variation of this type of emission between differing CCDs, as well as in time.

3.2.3 Solar Wind Charge Exchange Modeling

Solar wind charge exchange (SWCX) [25] provides additional cosmic X-ray background to the spectra. It occurs when rapidly moving, highly ionized solar wind interacts with more neutral gas (usually hydrogen) in the Solar System and strips an electron. Then this electron enters an excited state in the solar wind ion and cascades down, releasing an X-ray. This can occur for many ions, including carbon, oxygen and neon [15]. Similar to residual NXB emission lines, SWCX can be modeled with Gaussian lines. Thus, we also visually inspected the spectra for any residual lines that could be a result of SWCX. Unlike the NXB, which should not be Doppler shifted or broadened, SWCX can be due to the velocity of the solar wind. Hence, any lines that were centered within several eV of a common SWCX line were added to the model. For each observation, any emission lines with fit normalizations below 10^{-5} photons/cm^2/s or that had uncertainties greater than 100% were removed from the model and the model was re-fit.

---

[d] http://heasarc.gsfc.nasa.gov/cgi-bin/Tools/w3nh/w3nh.pl

Table 3.1 depicts the emission lines that were kept in the fits and their NXB and SWCX candidates. The NXB line, Au-Mα, should be centered on 2.123 keV. However, we find a strong 2.195 keV and 2.155 keV line for NGC 3402 Background BI and NGC 5129 Background FI observations, respectively. Sekiya [68] also identifies lines at similar energies as this instrumental NXB line. *The Suzaku Data Reduction Guide* discusses this feature as a result of an improper calibration of that NXB line. We have effectively removed this calibration issue by including the residual lines in our models.

Table 3.1. Model Emission Lines and Their Candidates

Observation	FI CCDs			BI CCD		
	Line Energy keV	Candidate	Emission Type	Line Energy keV	Candidate	Emission Type
NGC 3402	1.08	Ne X Lyα	SWCX	1.48	Al Kα	NXB
NGC 3402 Back	0.685	O VII	SWCX	0.58	O VII Kα	SWCX
	0.815	O VIII Lyγ	SWCX	1.285	Ne X	SWCX
	1.825	Si XIII	SWCX	2.195	Au Mα	NXB
NGC 5129	0.65	O VIII Lyα	SWCX	0.55	O VII Kα	SWCX
	0.915	Ne IX Kα	SWCX	0.85	O VIII Lyϵ	SWCX
NGC 5129 Back	0.63	N VII	SWCX	0.665	O VII Kβ	SWCX
	0.915	Ne IX Kα	SWCX	0.805	O VIII Lyγ	SWCX
	1.37	Mg XI Kα	SWCX	0.895	Ne IX Kα	SWCX
	2.155	Au Mα	NXB			

Note. — All line energies are the centers of residual lines as observed by the *Suzaku* XISs.

Table 3.2. Xspec Background Parameters and Normalizations for Spectral Analysis

Emission Source or Absorption	Model Type	Parameter	Fixed/Free	NGC 3402	NGC 5129
Galactic Absorption	wabs	$N_H (10^{22}\ \mathrm{cm}^{-2})$	Fixed	0.0477	0.0178
AGN	power-law	Γ	Fixed	1.41	1.41
		Normalization[b]	Free	$(7.63 \pm 0.23) \times 10^{-4}$	$(1.05 \pm 0.03) \times 10^{-3}$
Galaxy	apec	$k_B T$ (keV)	Free	0.177 ± 0.007	0.173 ± 0.009
		Abundance ($Z_\odot$)	Fixed	1	1
		Redshift	Fixed	0	0
		Normalization[c]	Free	$(1.65 \pm 0.19) \times 10^{-3}$	$(3.49 \pm 0.29) \times 10^{-3}$
Galaxy (NPS)[a]	apec	$k_B T$	Fixed	⋯	0.4
		Abundance	Fixed	⋯	1
		Redshift	Fixed	⋯	0
		Normalization[c]	Free	⋯	$(6.28 \pm 1.20) \times 10^{-4}$

Note. — All normalizations assume an emission area of 400π in Xspec.

[a] Excess emission due to the North Polar Spur (NPS).

[b] Power-law normalization in photons $\mathrm{cm}^{-2}\ \mathrm{s}^{-1}\ \mathrm{keV}^{-1}$ at 1 keV.

[c] *Apec* normalization given in cm^{-5}.

3.2.4 Group Halo Emission Modeling

We modeled the group halo emission using an *apec* thermal plasma model modified by Galactic absorption, allowing the temperatures and normalizations to vary freely and with the remaining parameters frozen at $Z = 0.2Z_\odot$ (based on the measurements by Eckmiller et al. [23]) and the respective redshift of each group's central galaxy ($z = 0.0153$ for NGC 3402 and $z = 0.0230$ for NGC 5129). Here we have used the default abundance table for this version of `Xspec`, *angr* [2]. This group emission was added to all the background components to model the target group spectra. Then both background and group FI and BI spectra were simultaneously fit, totaling four spectra for NGC 3402 and six for NGC 5129 being fit at the same time. There were six for NGC 5129 due to both target group pointings and one background pointing.

Furthermore, we considered the possibility of systematic uncertainties in the background spectral modeling. To do this, we fit all combinations of models where: $\Gamma = 1.41$ or 1.56, the Galactic foreground *apec* temperature would be one single component and allowed to vary, or frozen at two components ($k_BT = 0.07$ keV and 0.2 keV), and residual NXB and SWCX lines would be included or not considered entirely. The $\Gamma = 1.56$ variation assumes the power-law component is due to unresolved low-mass X-ray binaries (LMXBs) within our Galaxy, whereas the two Galactic *apec* components of $k_BT = 0.07$ keV and $k_BT = 0.2$ keV reference the model parameters in Humphrey et al. [37, 38]. For NGC 5129, we kept the additional fixed $k_BT = 0.4$ keV *apec* component for all models.

All eight of the different background model parameters were applied to the source group and background spectra in this way, producing eight separate simultaneous spectral models. The task *steppar* was performed on each fit for the group *apec* temperature to ensure that it had not fallen into a local minimum. The subsequent fits were all relatively good for NGC 3402, with reasonable fit parameter values and indicating clear detections of the group halo emission. Unfortunately for NGC 5129, the group *apec* temperatures for each pointing were vastly different, where $k_B T$ was unphysically large for the 1^{st} observation and the fits were fairly poor.

To gauge what was occurring, more spectral analysis was performed for NGC 5129. First, we tried separately fitting each observation simultaneously with the background. The eight fit results for the 1^{st} observation were well-behaved, in which the reduced χ^2 and parameter values with errors were all acceptable. On the other hand, the fits for the 2^{nd} observation were comparatively poor in reduced χ^2 and some produced unrealistically low group *apec* temperatures. Also, there were very large uncertainties in the group *apec* normalization and $k_B T$, as well as in several other parameters. Moreover, the background components did not agree between the separate fittings of each observation.

Next, we attempted fitting the background observations separately, then constrained the target observations' best-fit background parameters to be within 3σ of the results from those separate fits. The outcome was similar to the other test: the 1^{st} observation had good fits with most parameters being well constrained whereas the 2^{nd} observation consistently had extremely poor fits with large uncertainties in several parameters, especially the group *apec* normalization and $k_B T$. The 2^{nd} observation also generated unrealistic group temperatures in this test. From this, it is apparent that the 2^{nd} observation of NGC 5129 is a non-detection. Though unfortunate, this is not completely unexpected due to the excessive number of extraction regions needed to filter out several point sources for that observation, as seen in Fig 2.5. The fully extracted observed area was considerably smaller than that of the 1^{st} pointing, which can be detrimental to such low surface brightness observations.

Thus, we chose to present the results of the simultaneous fit between the background and off-center target pointing for NGC 5129 1^{st}. Any subsequent results referred to as "NGC 5129" are solely from that observation. The resulting eight models each for NGC 3402 and NGC 5129 were all comparatively good fits, varying little in reduced χ^2 (see Table 3.3).

3.2.5 Spectral Analysis Results

We chose the models shown in Tables 3.2 and 3.3 due to their overall excellent fit to the data (including consideration of residuals), being the models nearest to mean and median across the spectra for both groups, when distributed by temperature, and for allowing the Galactic *apec* temperature to vary freely. This type of model is more likely to be physically accurate, since the Galactic emission varies throughout the sky not only in normalization but also in temperature [51]. The average best-fit temperatures for the Galactic foreground were $k_B T_{ave} = 0.177$ keV and 0.173 keV for NGC 3402 and NGC 5129, respectively. These temperatures are consistent to that of other research using the same approach, e.g., Bautz et al. [7] and Simionescu et al. [71]. In addition, choosing the AGN index of 1.41 is far more representative of the power-law component than that of LMXBs, since our observations are relatively high in the Galactic plane with Galactic latitudes of $\sim 40^\circ$ and 75° for NGC 3402 and NGC 5129, respectively. For each chosen fit, the reduced χ^2 (defined as χ^2_{min}/dof) is approximately unity, suggesting that the background has been successfully modeled and extracted from the hot halo group emission.

Figures 3.1-3.4 show the best-fit unfolded models (data and models not convolved with the detector's response) with individual model components and spectral data overlayed for both the off-center group and background observations, divided into each type of CCD. These models' best-fit parameters and normalizations are given in Tables 3.2 and 3.3, in which NXB and SWCX emission line parameters and normalizations are left out for compactness. Moreover, Figures 3.5-3.8 depict the same information as Figures 3.1-3.4, except the models and data have been convolved with the detector's response. Both folded and unfolded spectra comparing between FI and BI CCDs separately for the background and target observations are also included in Figures 3.9-3.16.

One issue of critical importance is that when generating ARF files of extended sources, the usual assumption is the emission originates from a 20 arcminute radius circle, so the emitting area is $20^2\pi$ arcmin^2. Any normalizations generated from the fit analysis are using this area. Typically one desires the normalization to represent the extracted observation area instead. To do this, the output normalization should be multiplied by the SOURCE_RATIO_REG factor found in the header of the ARF file, which is simply the ratio of observation area (with extraction regions removed) to 400π. This must be considered for all analyses utilizing these normalizations or fluxes derived from them (Eric Miller, private communication); see [40] for details. We discuss adjustments made based on this crucial information in subsequent chapters.

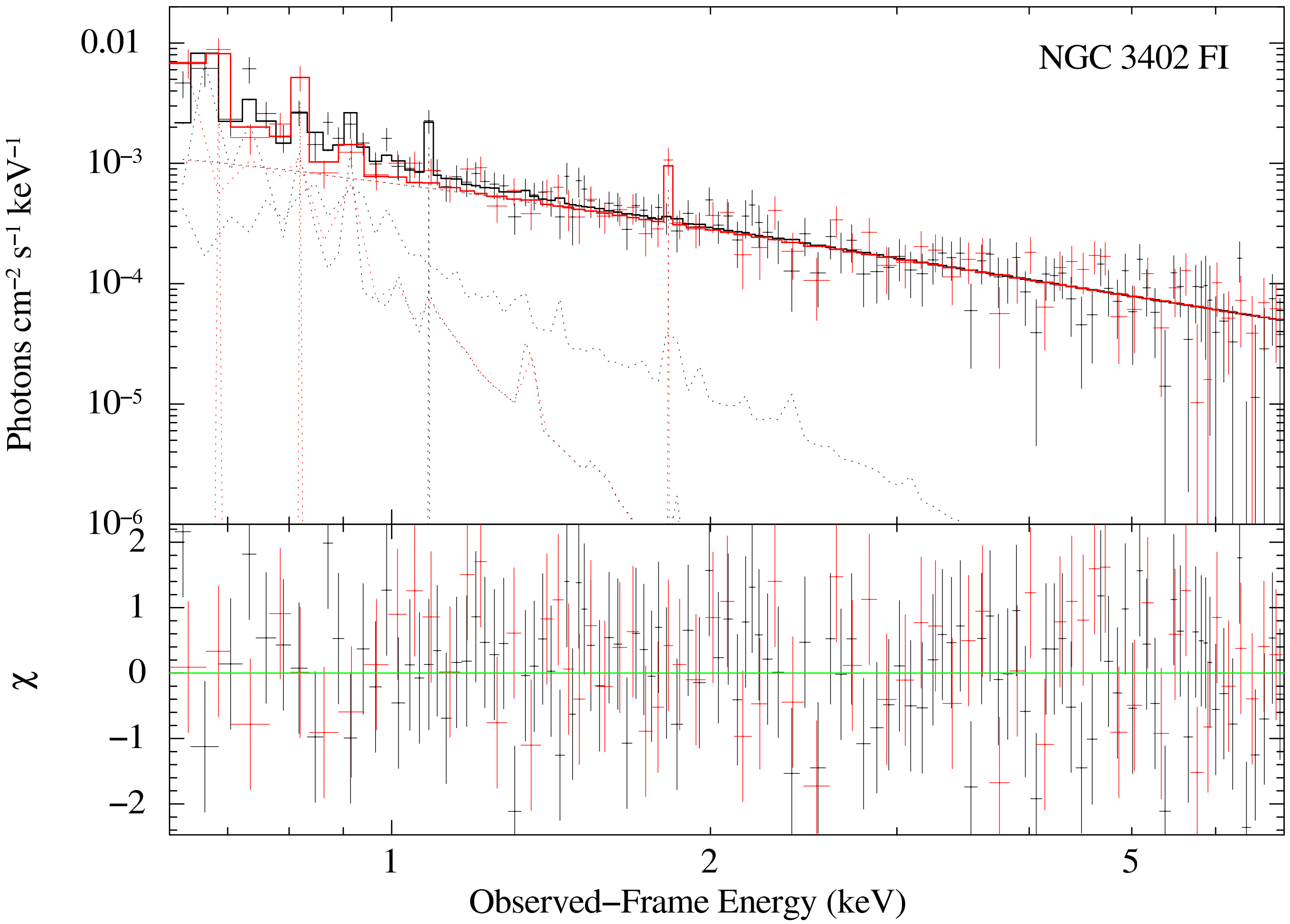

Fig. 3.1.— Unfolded spectra for NGC 3402 FI off-center target (black) and background (red) observations. The solid lines are the best-fit theoretical model, not folded with the instrument response, while crosses are the corresponding binned spectral data. Bottom panel contains the residuals in units of standard deviation with error bars of 1σ.

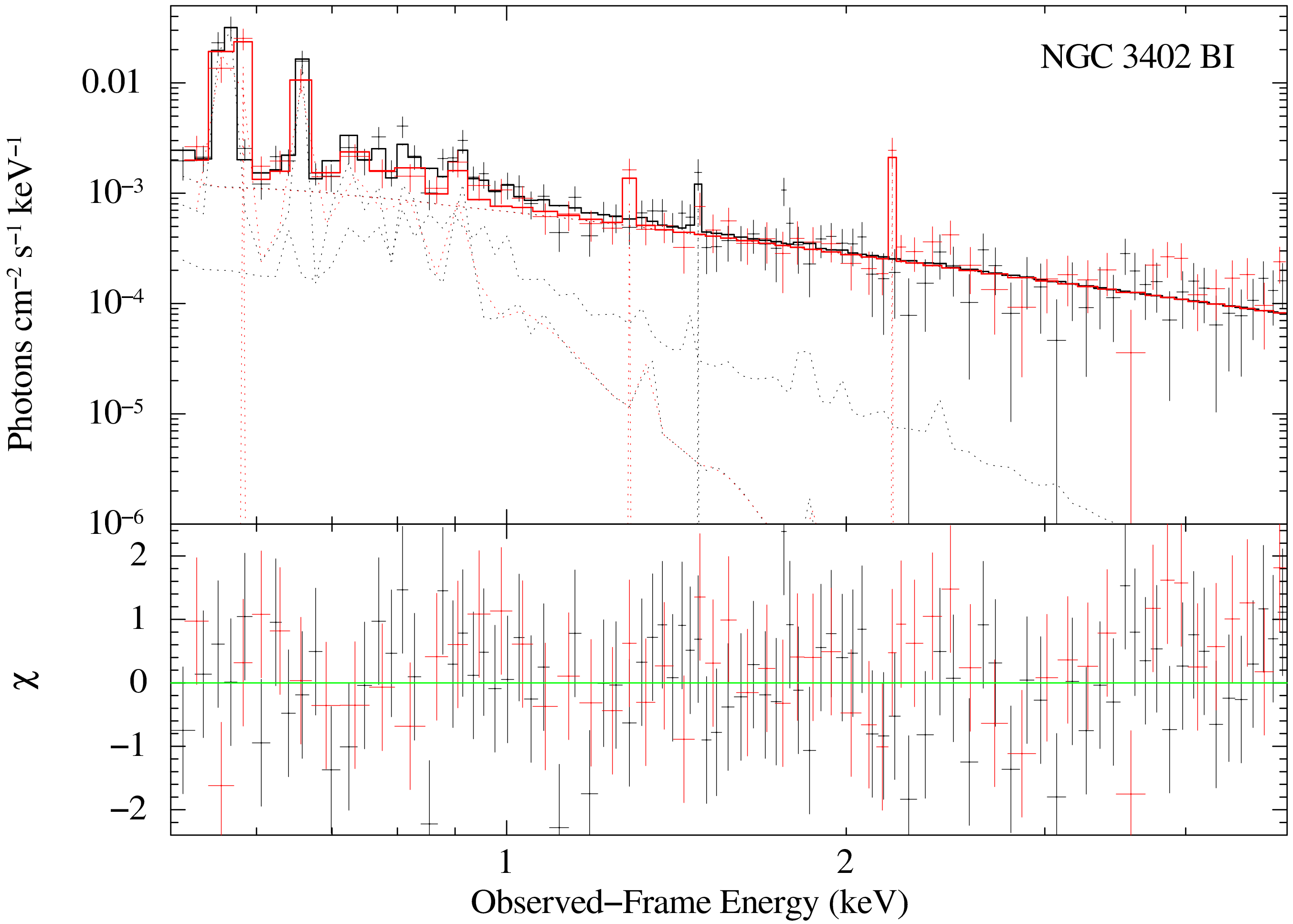

Fig. 3.2.— Same as in Figure 3.1, except for the BI CCD.

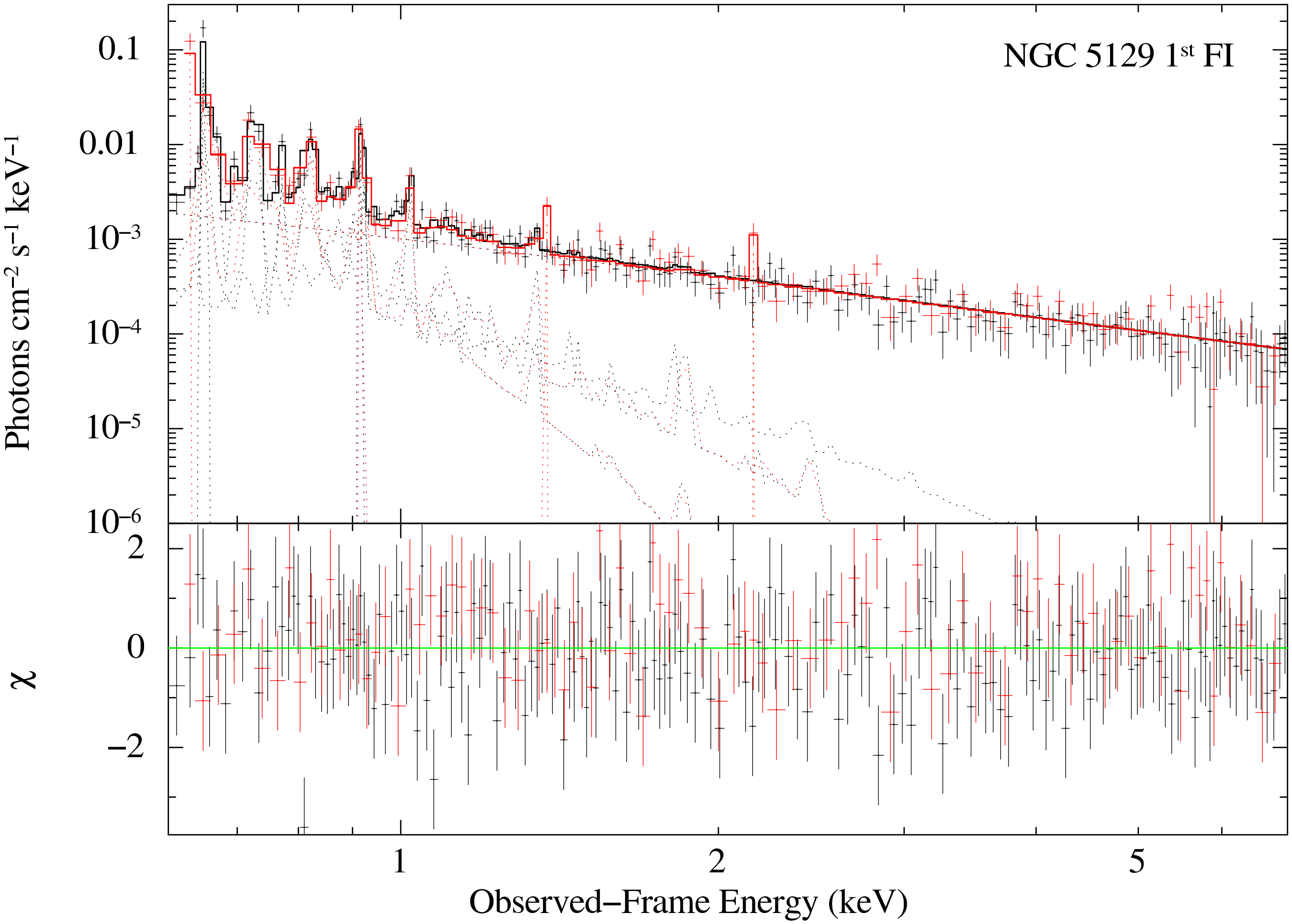

Fig. 3.3.— Unfolded spectra for NGC 5129 1^{st} FI off-center target (black) and background (red) observations. The solid lines are the best-fit theoretical model, not folded with the instrument response, while crosses are the corresponding binned spectral data. Bottom panel contains the residuals in units of standard deviation with error bars of 1σ.

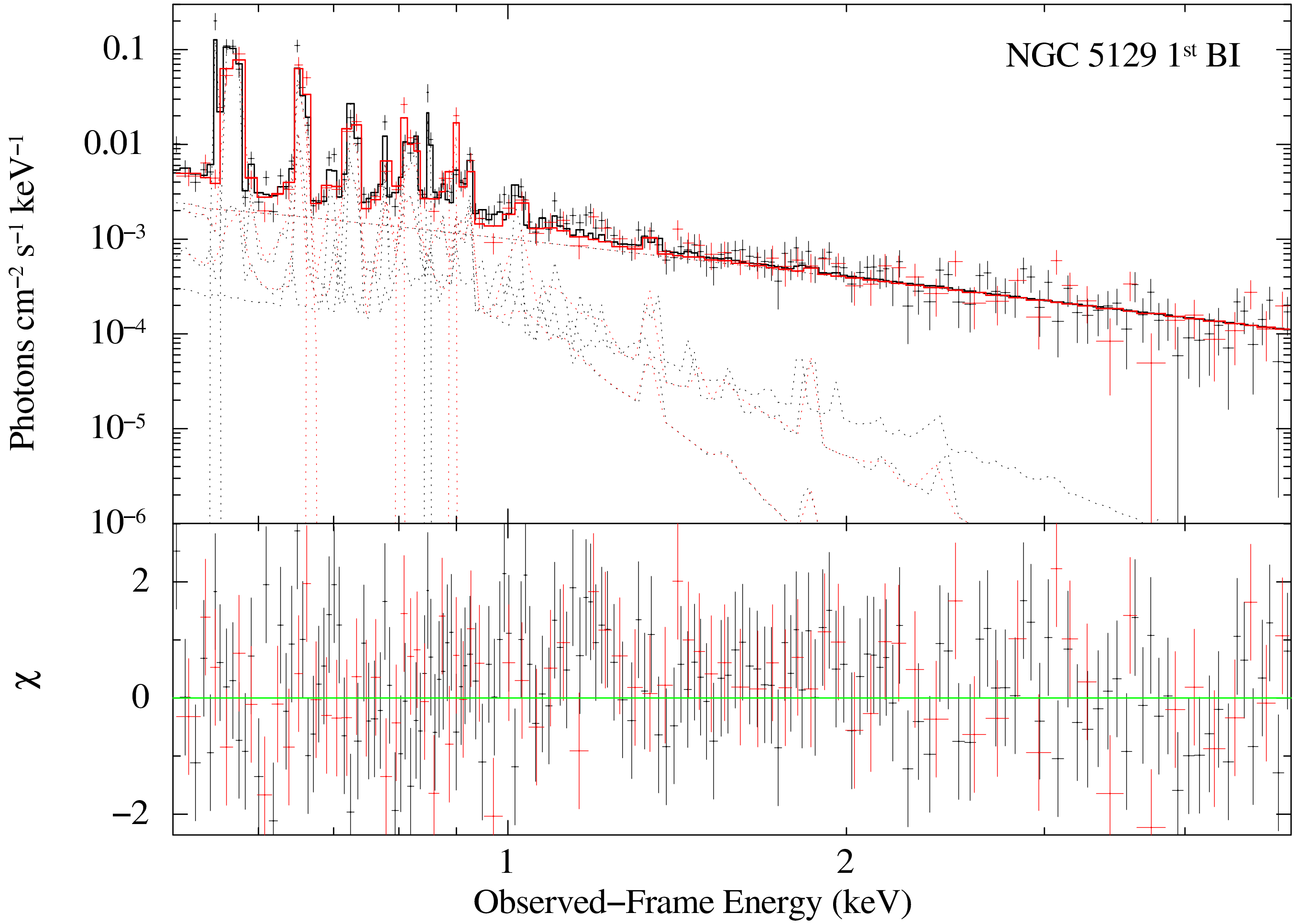

Fig. 3.4.— Same as in Figure 3.3, except for the BI CCD.

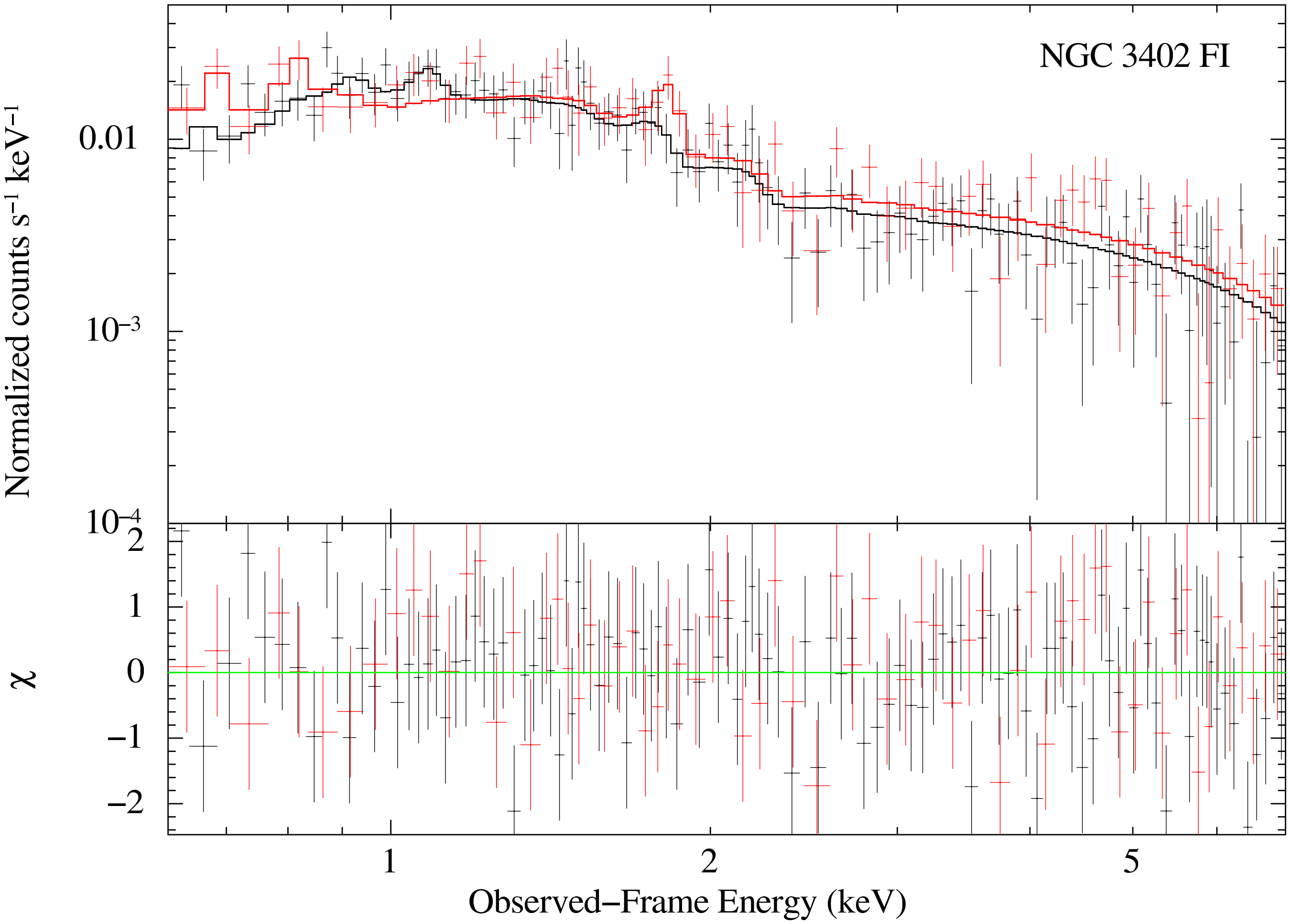

Fig. 3.5.— Normalized folded spectra for NGC 3402 FI off-center target (black) and background (red) observations. The solid lines are the best-fit theoretical model, folded with the instrument response, while crosses are the corresponding binned spectral data. Bottom panel contains the residuals in units of standard deviation with error bars of 1σ.

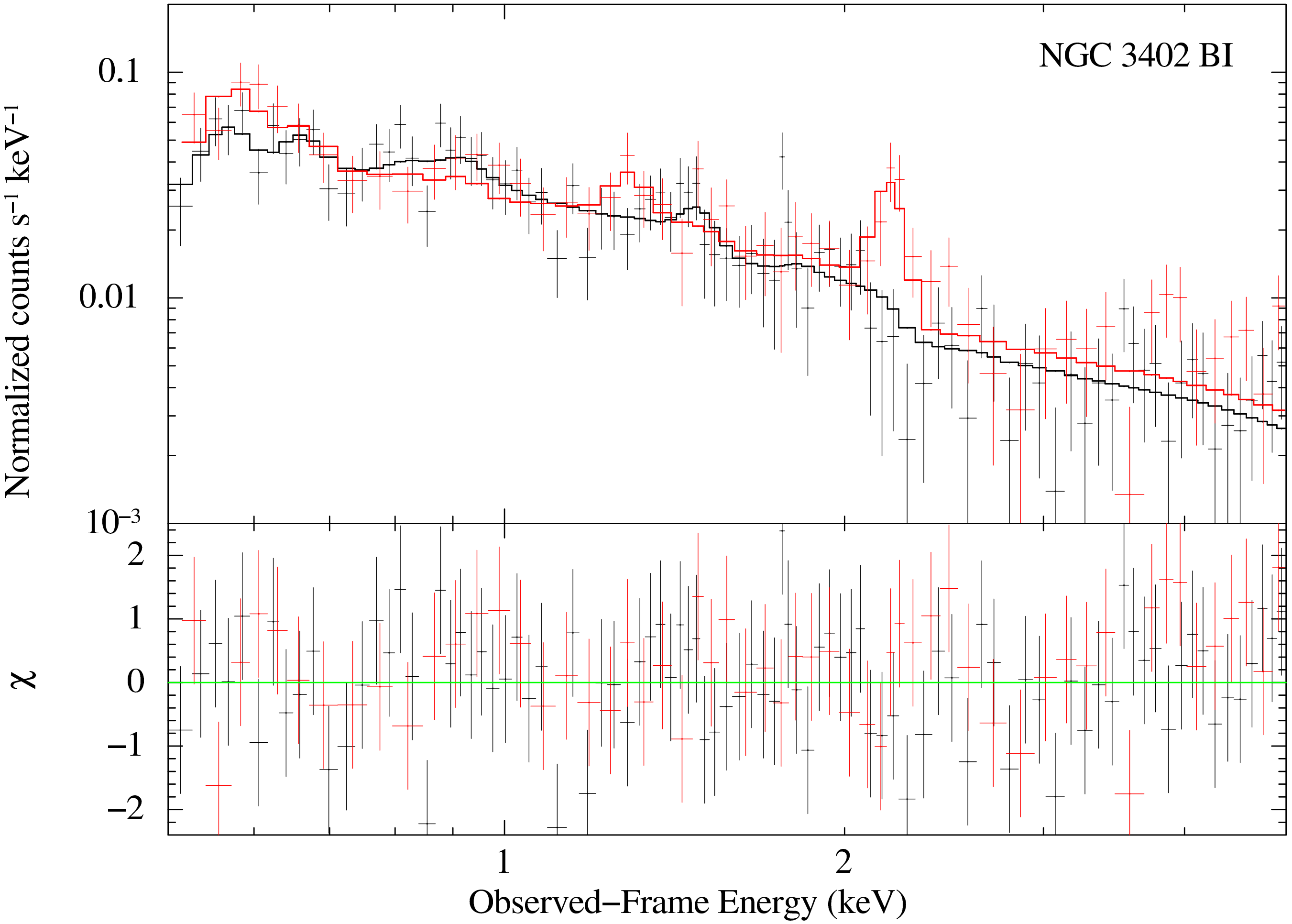

Fig. 3.6.— Same as in Figure 3.5, except for the BI CCD.

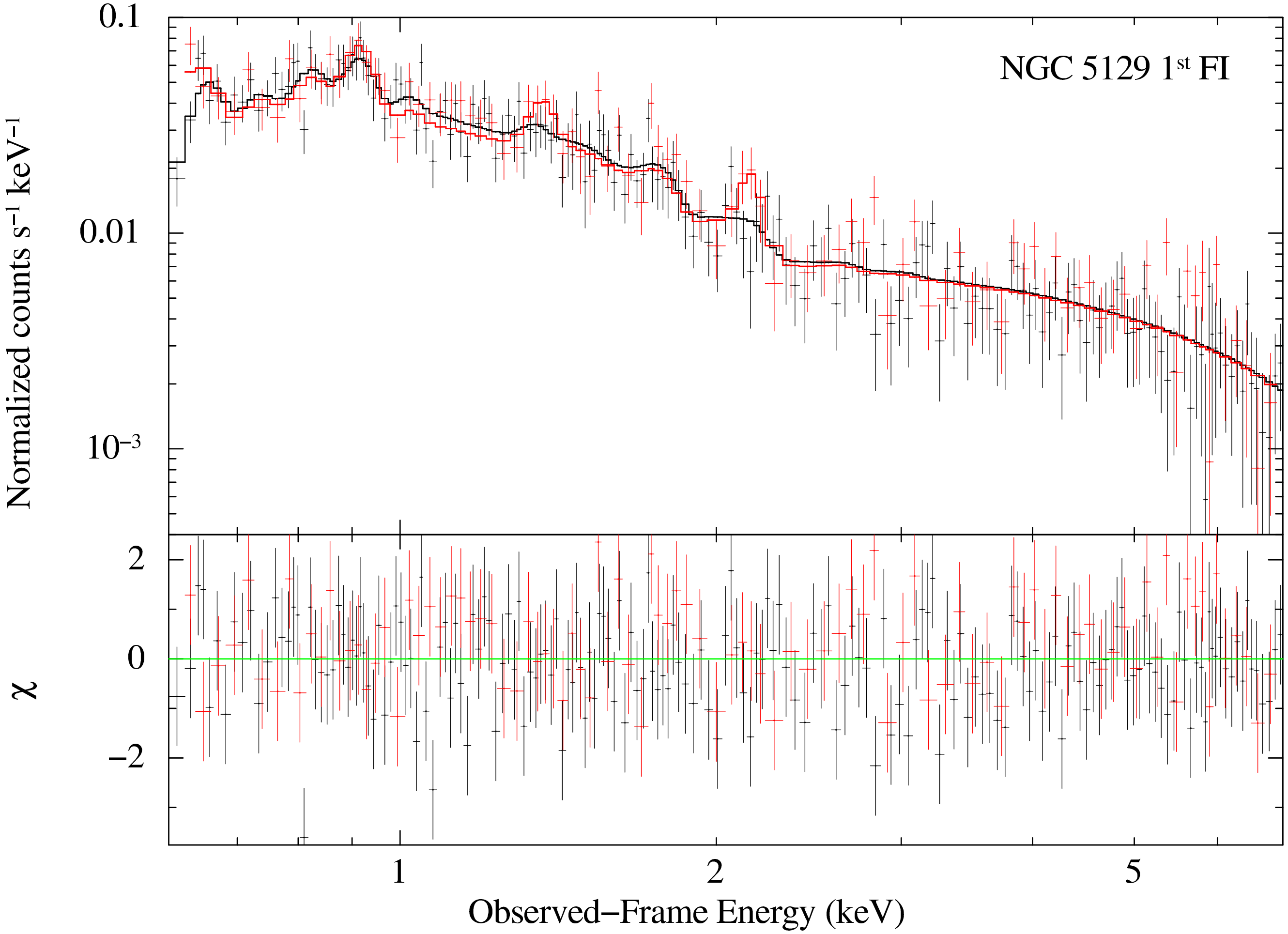

Fig. 3.7.— Normalized folded spectra for NGC 5129 1^{st} FI off-center target (black) and background (red) observations. The solid lines are the best-fit theoretical model, folded with the instrument response, while crosses are the corresponding binned spectral data. Bottom panel contains the residuals in units of standard deviation with error bars of 1σ.

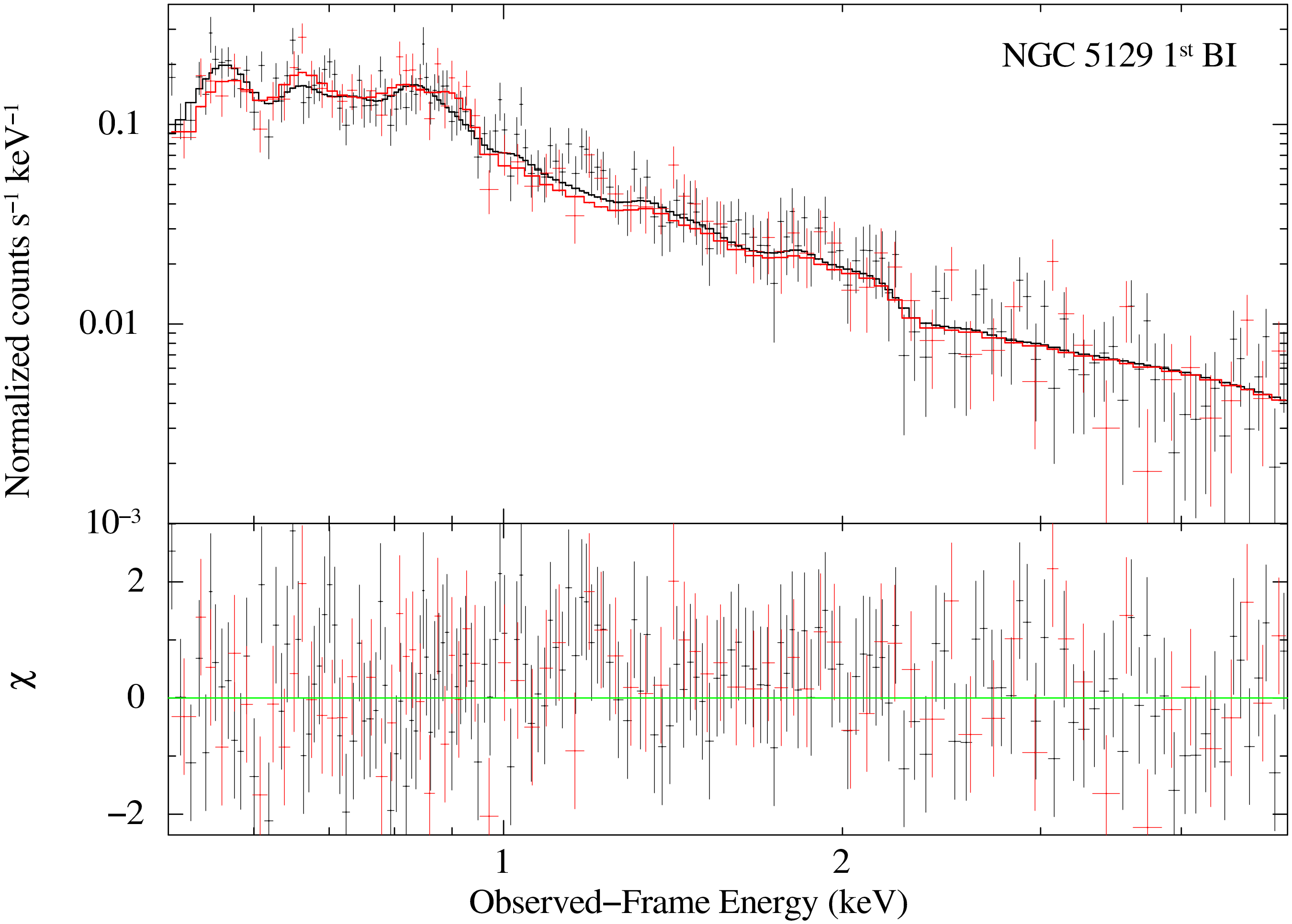

Fig. 3.8.— Same as in Figure 3.7, except for the BI CCD.

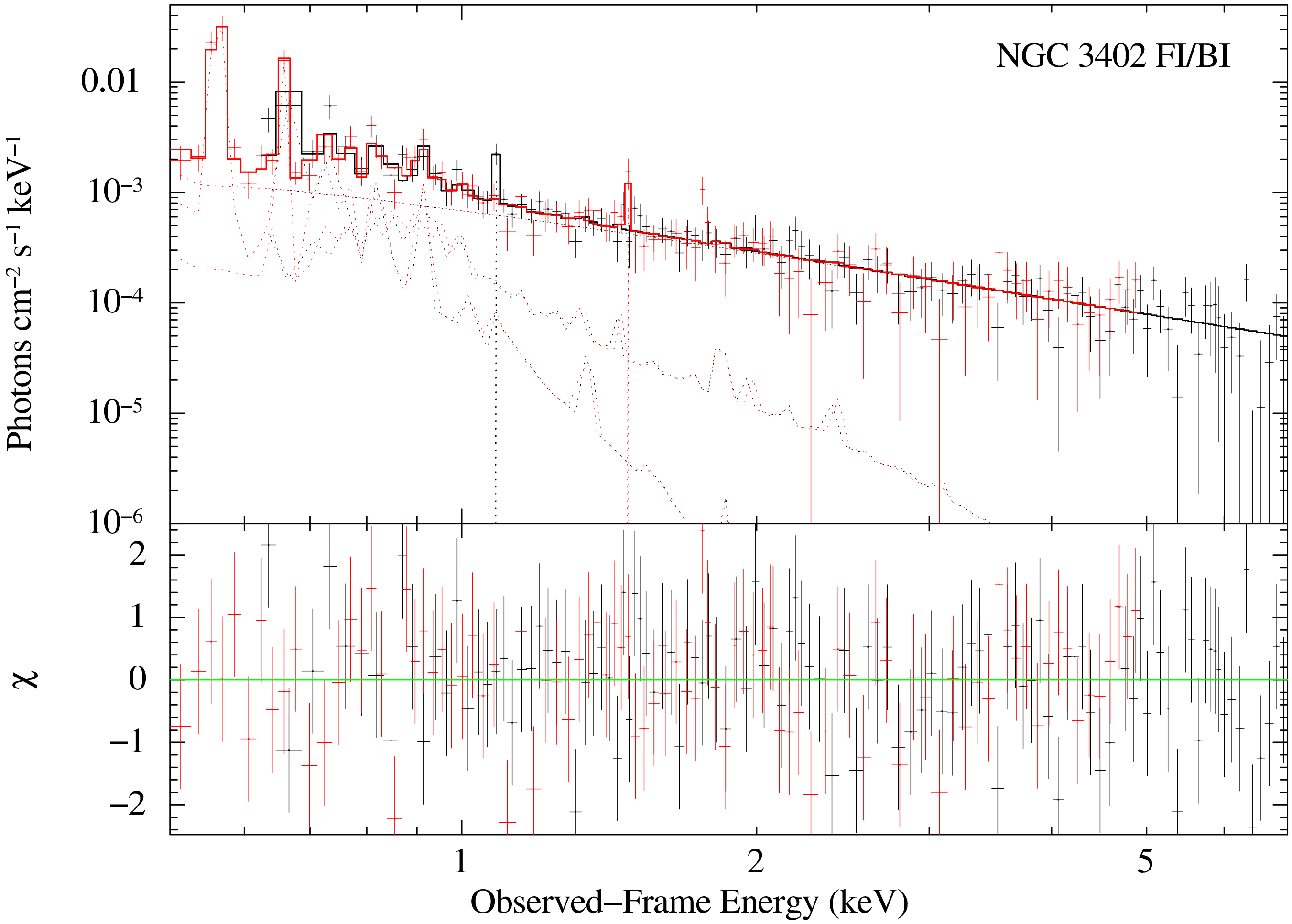

Fig. 3.9.— Unfolded spectra for NGC 3402 off-center target observations, for both FI (black) and BI (red) CCDs. The solid lines are the best-fit theoretical model, not folded with the instrument response, while crosses are the corresponding binned spectral data. Bottom panel contains the residuals in units of standard deviation with error bars of 1σ.

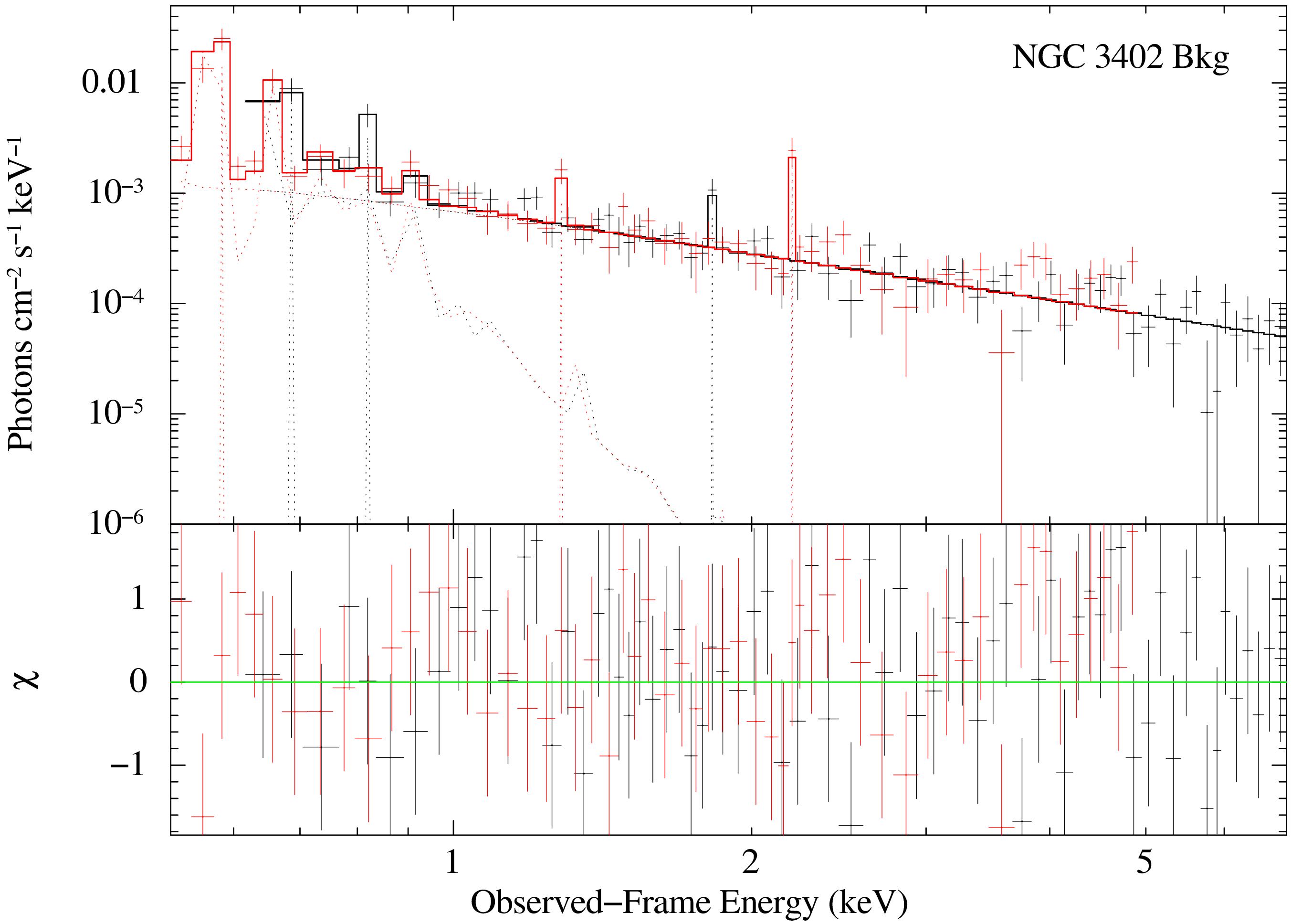

Fig. 3.10.— Same as in Figure 3.9, except for the background observations.

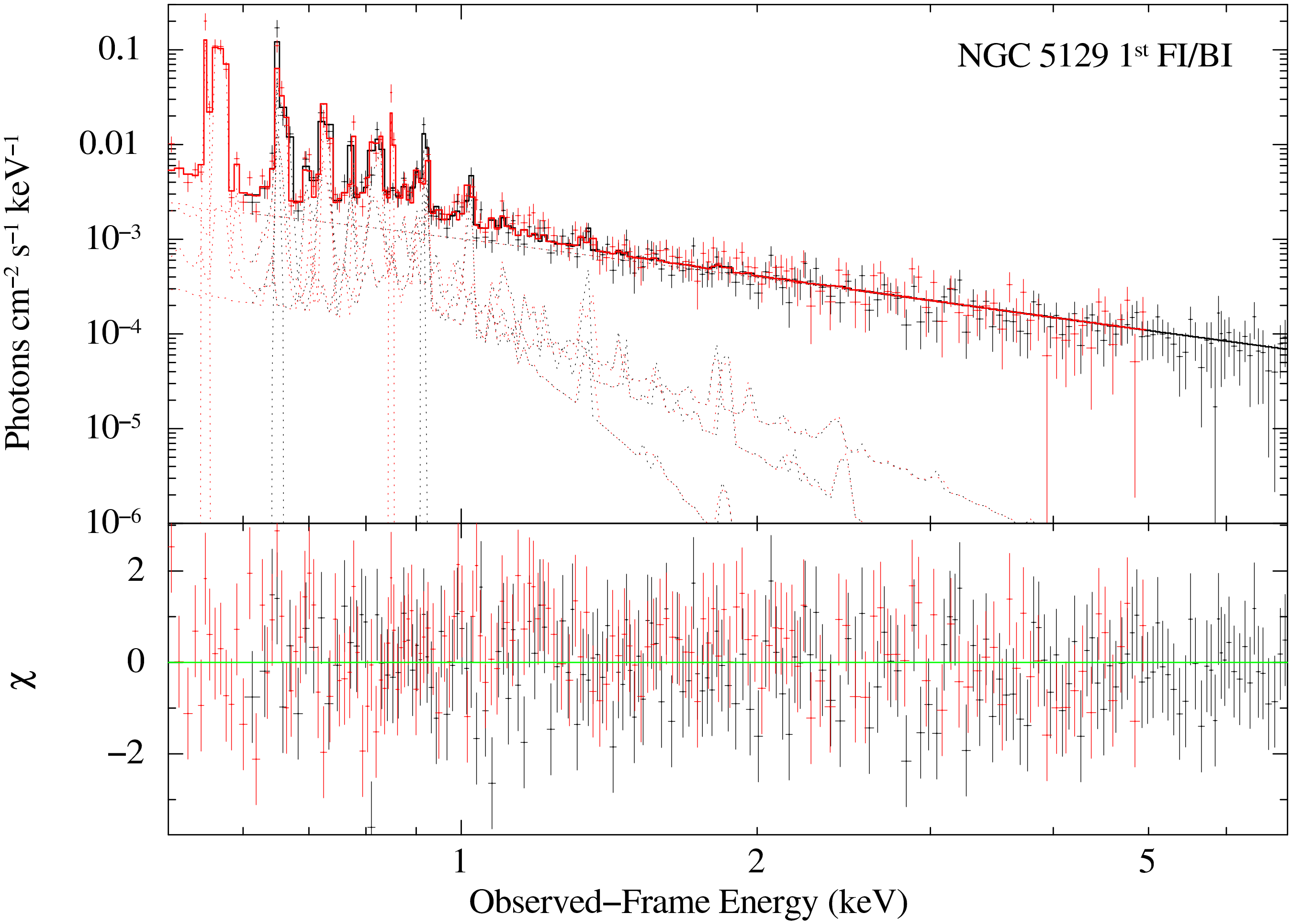

Fig. 3.11.— Unfolded spectra for NGC 5129 1^{st} off-center target observations, for both FI (black) and BI (red) CCDs. The solid lines are the best-fit theoretical model, not folded with the instrument response, while crosses are the corresponding binned spectral data. Bottom panel contains the residuals in units of standard deviation with error bars of 1σ.

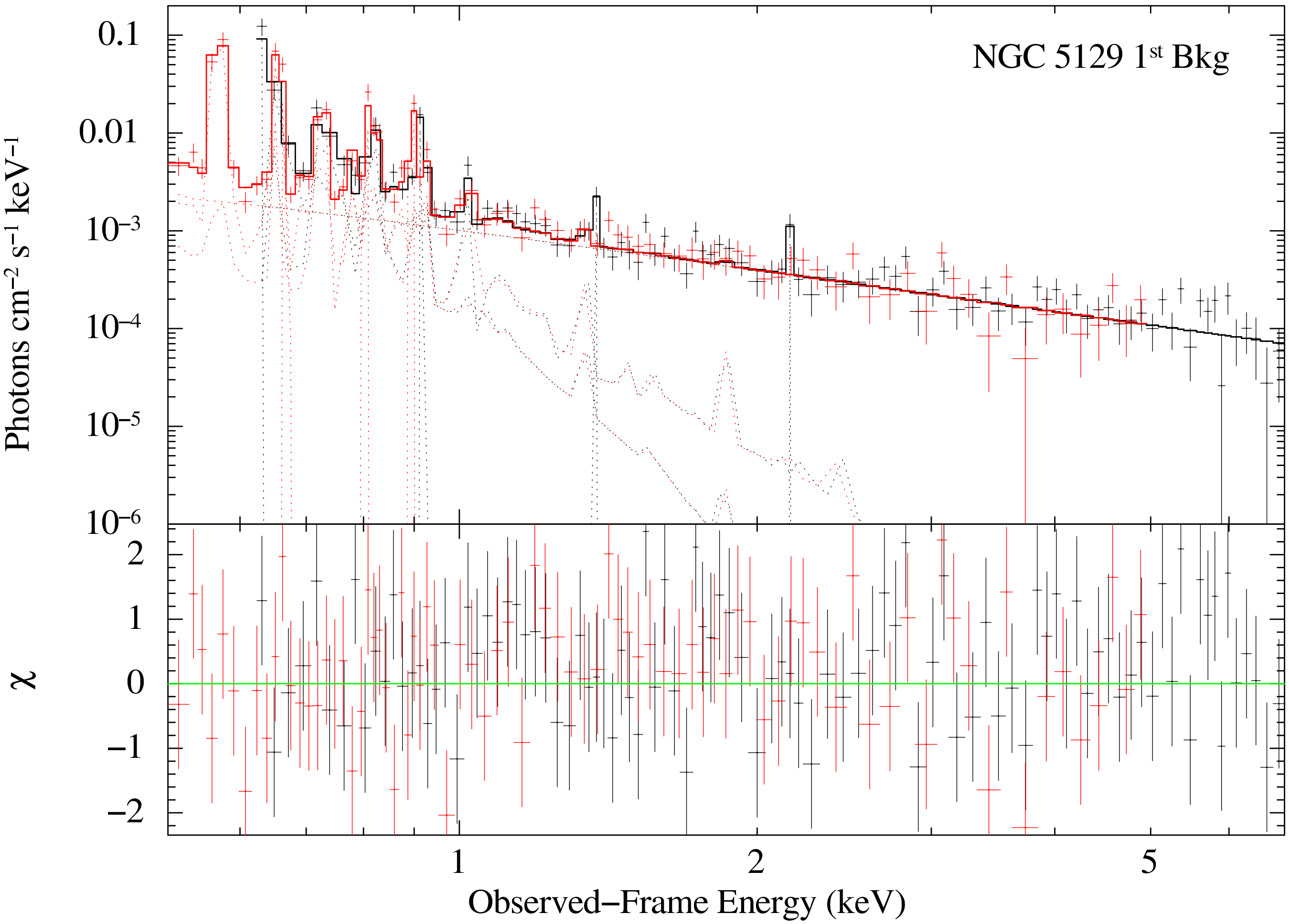

Fig. 3.12.— Same as in Figure 3.11, except for the background observations.

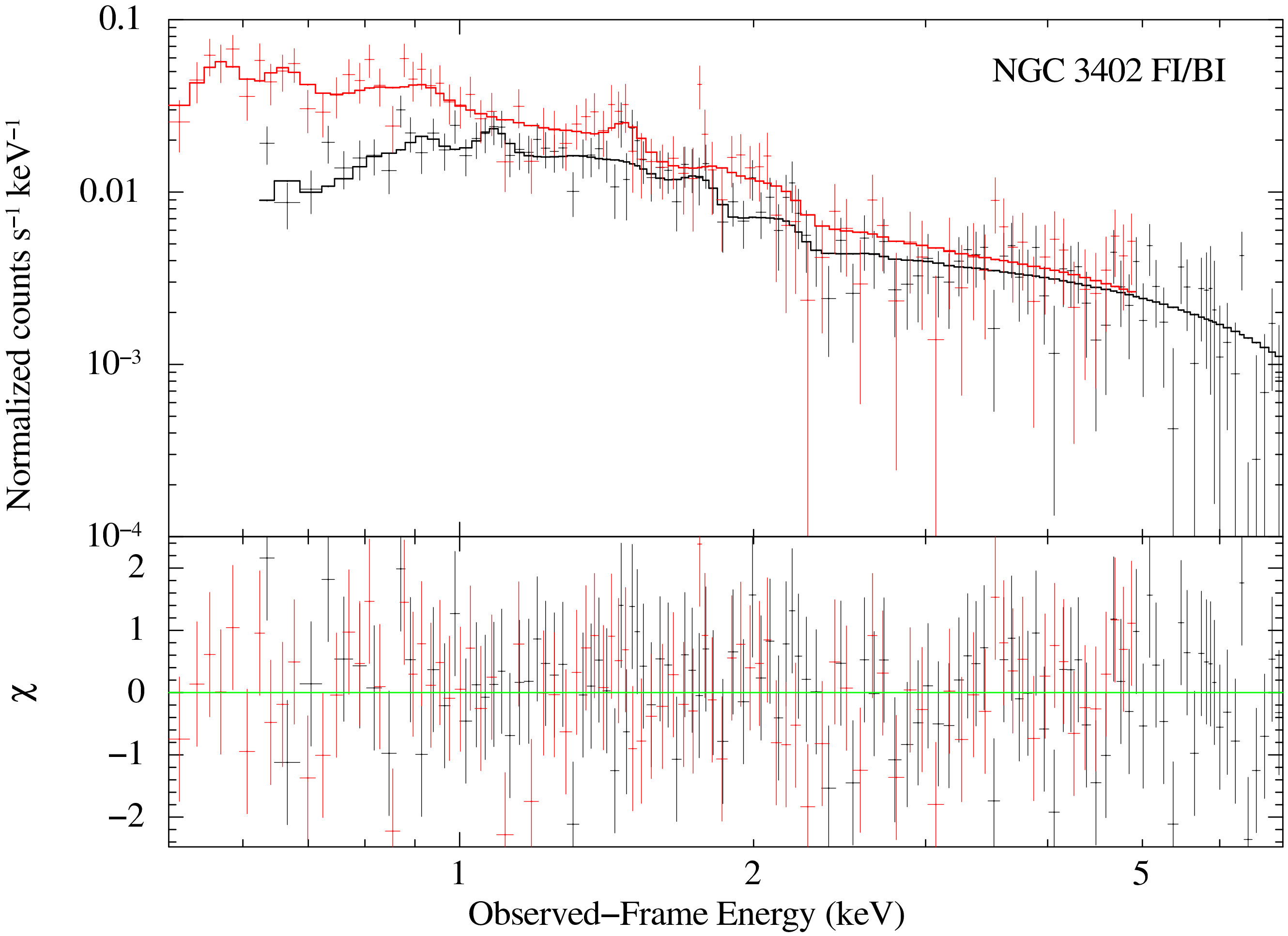

Fig. 3.13.— Normalized folded spectra for NGC 3402 off-center target observations, for both FI (black) and BI (red) CCDs. The solid lines are the best-fit theoretical model, folded with the instrument response, while crosses are the corresponding binned spectral data. Bottom panel contains the residuals in units of standard deviation with error bars of 1σ.

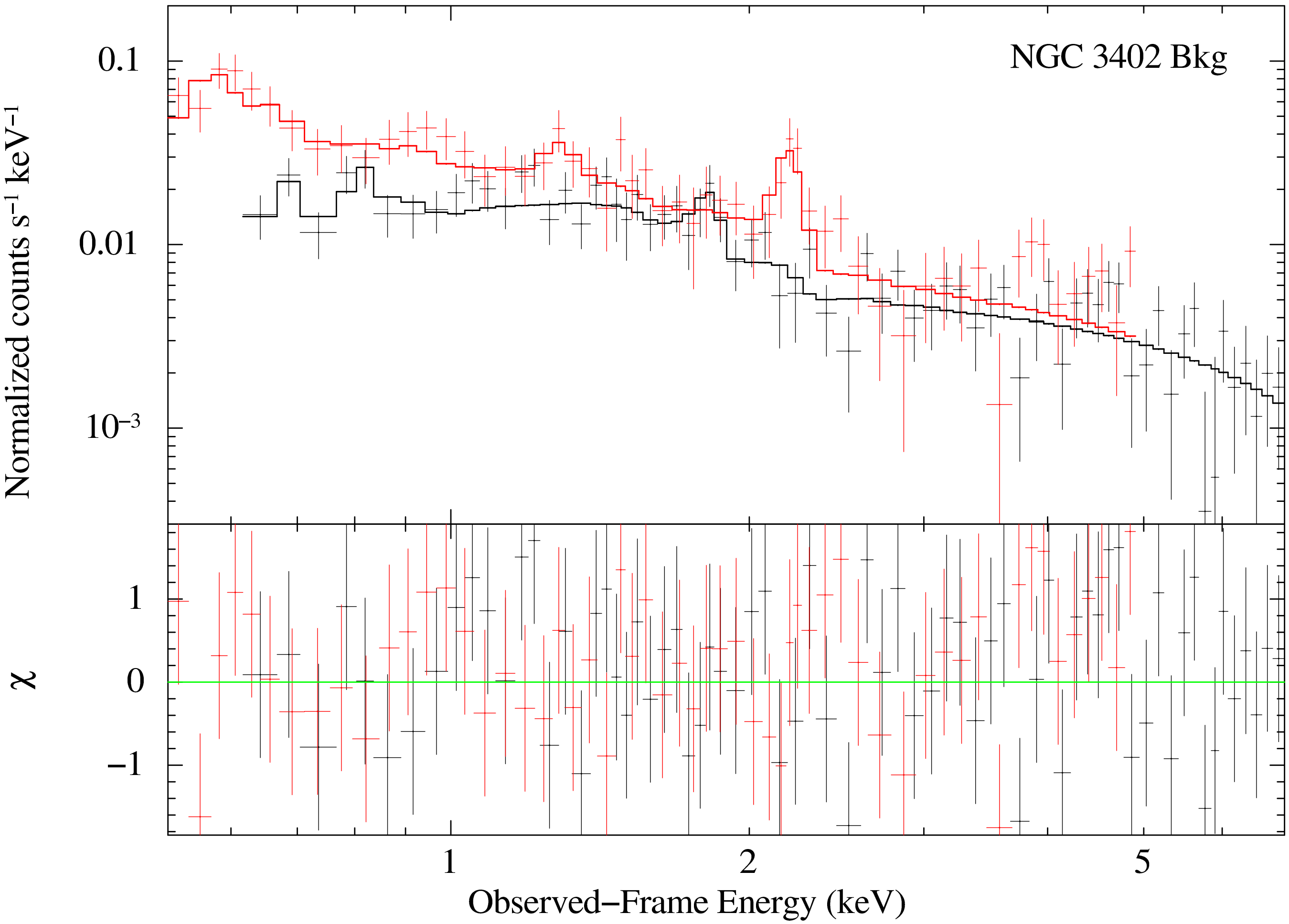

Fig. 3.14.— Same as in Figure 3.13, except for the background observations.

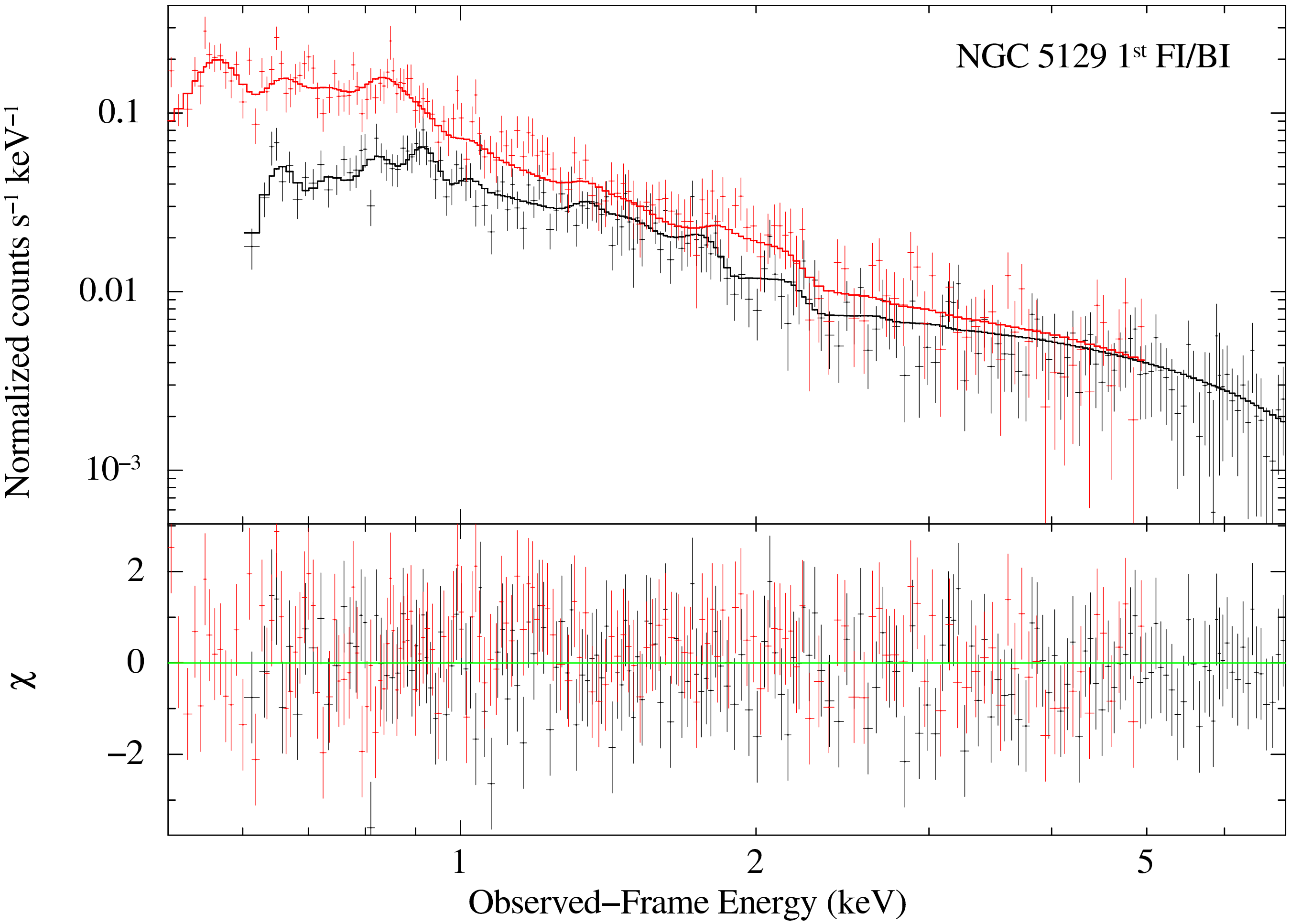

Fig. 3.15.— Normalized folded spectra for NGC 5129 1^{st} off-center target observations, for both FI (black) and BI (red) CCDs. The solid lines are the best-fit theoretical model, folded with the instrument response, while crosses are the corresponding binned spectral data. Bottom panel contains the residuals in units of standard deviation with error bars of 1σ.

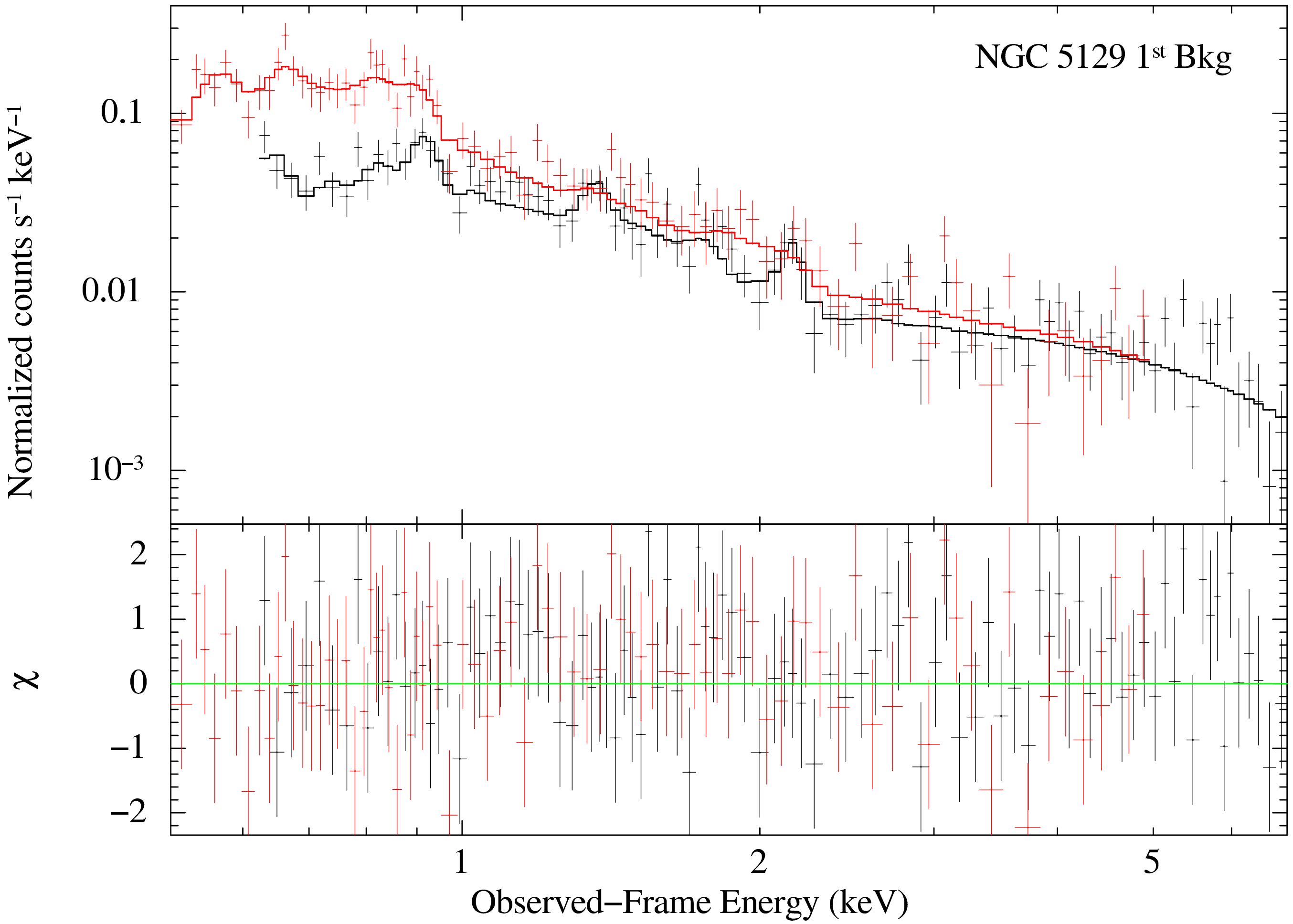

Fig. 3.16.— Same as in Figure 3.15, except for the background observations.

Also included in Table 3.3 are systematic uncertainties (σ_{syst}) in the group *apec* temperature and normalization introduced from the eight variations in background parameters. While the σ_{syst} in the group temperature is approximately half (or less) than that of statistical, the σ_{syst} in normalization is more significant. Furthermore, we changed the fixed abundance from $Z = 0.2Z_{\odot}$ to $Z = 0.33Z_{\odot}$ solely in the chosen models and re-fit. The change in group temperature between models with these abundances is small, $\Delta k_B T = 0.003$ keV for NGC 3402 and $\Delta k_B T = 0.019$ keV for NGC 5129. However, the relative change in group normalization between them is larger, $\Delta norm/norm = 0.32$ and 0.31 for NGC 3402 and NGC 5129, respectively.

Ultimately, we chose to perform all subsequent analysis and computations purely considering statistical uncertainties. In addition, the uncertainties in group temperature and normalization shown in Table 3.3 were averaged when performing ensuing calculations. Since different components in the target spectra have been effectively isolated through spectral modeling, this allowed for more success in detecting the group emission compared to the direct subtraction method. Specifically, the group emission was detected at 4.3σ and 2.7σ for NGC 3402 and NGC 5129, respectively. We use these constraints on the group emission from the spectral modeling in our subsequent analysis.

Table 3.3. Xspec Group Parameters and Normalizations for Spectral Analysis

Emission Source or Absorption	Model Type	Parameter	Fixed/Free	NGC 3402	NGC 5129
Galactic Absorption	wabs	$N_H (10^{22}\ \mathrm{cm}^{-2})$	Fixed	0.046	0.0176
Group Hot Halo	apec	$k_B T$ (keV)	Free	$0.862^{+0.093}_{-0.112}$[a] $\pm$ 0.054[b]	0.962 $^{+0.215}_{-0.147}$[a] $\pm$ 0.066[b]
		Abundance ($Z_\odot$)	Fixed	0.2	0.2
		Redshift	Fixed	0.0153	0.0230
		Normalization[c]	Free	$(5.24^{+1.29}_{-1.15}$[a] $\pm$ 0.76[b] $)\times10^{-4}$	(5.09 $\pm$1.91[a] $\pm$ 1.11[b] $)\times10^{-4}$
		χ^2_{min}/dof		249/317	471/506
		χ^2_ν range[d]		0.784–0.894	0.917–1.06

Note. — All normalizations assume an emission area of 400π in Xspec.

[a] Statistical uncertainties

[b] Systematic uncertainties based on the eight different background models discussed in Chapter 3.2.4.

[c] *Apec* normalization given in cm^{-5}.

[d] Range in reduced χ^2 for the eight different background and group simultaneous models.

3.2.6 PSF Smearing

Due to the faintness of our detected signal, it is pertinent to consider contributions from the galaxy group core smeared by the PSF into the CCD field of view. Systematics of this type are only important if the group core is within the FOV of the corresponding telescope's mirrors, which is slightly larger than the detector FOV. Since the exact size of that is not known, we performed a conservative estimation on the possible impact of PSF smearing.

This emission was estimated by considering both the PSF and off-axis effective area of *Suzaku*. Using the plots from the *Suzaku Technical Description* (TD), we first approximated the level of emission from the core due to the PSF that one should expect for our observations. Extrapolating the *Suzaku* PSF (Figure 6.12 of the TD) to our observation radii, we found that the smeared emission from the core at these radii is between five and six orders of magnitude less than that of the group center, for both galaxy groups. We also included the effects of vignetting, which reduces this signal further. Following the plot for 1.49 keV in Figure 6.17 of the TD, the effective area is $\sim$1000 times less at the group cores since they are off-axis in the observations. Combining these, both contributions are approximately four and five orders of magnitude below the detected signal, for NGC 3402 and NGC 5129, respectively. Since this emission from the group core is several orders of magnitude below the detected signal for both groups, it is negligible to our analysis.

3.2.7 Stray Light

Systematic uncertainties due to stray light entering the detector from the group core is crucial to consider for our off-center observations. Stray light is known as emission that scatters off the primary and secondary mirrors onto the focal plane any way other than originally intended (see the *Suzaku* TD and Takei et al. [75]).

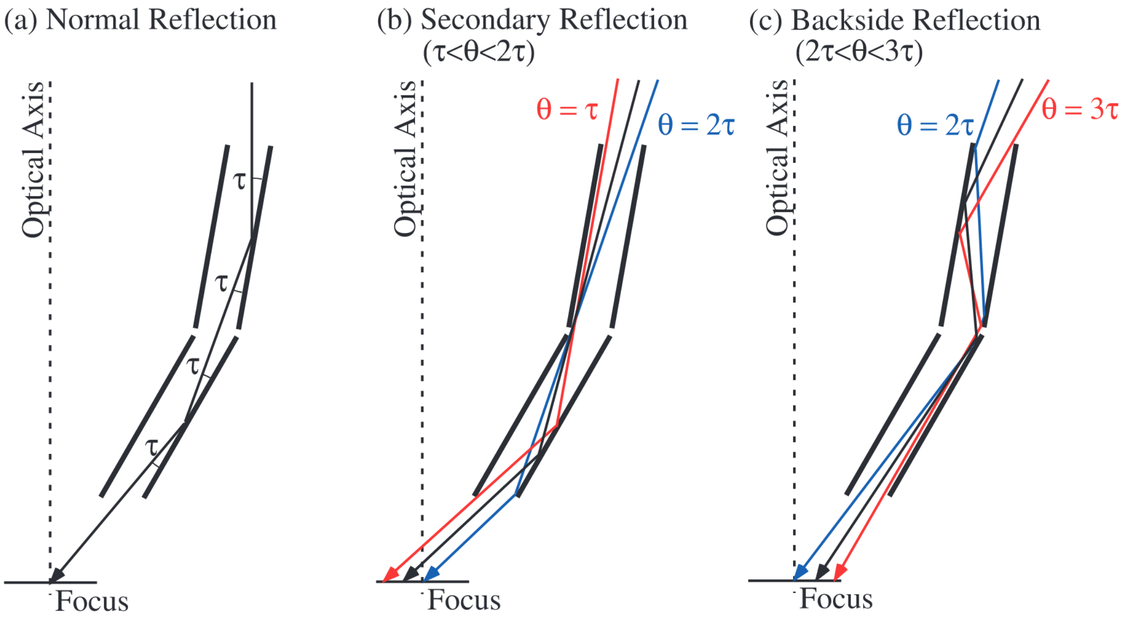

Fig. 3.17.— Representations of stray light and normal reflection. The angle τ defines the "oblique angle of the primary reflector measured from the optical axis of the XRT"[54]. This figure is from Mori et al. [54].

For example, light outside the detector FOV can enter the mirrors and glance off the secondary mirror only. Another common scenario is radiation reflecting off the backside of the primary, then reflecting normally onto the CCD [54]. These ways in which stray light can occur are illustrated in Figure 3.17. To determine whether stray light is an important contribution for our observations, we performed simulations using the FTOOL `xissim` ver. 2010-11-05. We obtained a "zeroth-order" estimate (Eric Miller, private communication) by modeling both groups as point sources and used the exposure time for the cleaned events with the COR2 condition applied. The simulations were done using the total Chandra count rates (0.7–2 keV) within $1'$, integrated from the SB profiles (Figure 4.4). Then, we converted these to absorbed flux between 0.6–7 keV to use as inputs for `xissim`. This was carried out using the online tool `WebPIMMS`, which requires input model parameters such as gas temperature and redshift. We assumed an *apec* model with the same redshift as in Table 3.3. However, the temperatures were chosen to be

$log(T) = 7.05$ for NGC 3402 and 7.1 for NGC 5129 to better reflect their values in the central $1'$. For this same reason, the neutral hydrogen column density for NGC 3402 was changed to $N_H = 0.044{\times}10^{22}$ cm^{-2} and the metallicities used were: $Z = 0.6Z_\odot$ and $Z = 0.4Z_\odot$ for NGC 3402 and NGC 5129, respectively [23, 78]. The simulations performed raytracing for all photons at a single energy, 1 keV, and were computed for the XIS0 CCD.

The resultant events proved to be negligible, with 5 counts for NGC 3402 and 1 count for NGC 5129. To estimate its significance, we compared the stray light flux (effective area approximated as 200 cm^2 at 1 keV) to the 0.6–7 keV flux derived from the best-fit spectral models. At this stage in the analysis, we began using HEAsoft 6.25, with `Xspec` ver. 12.10.1 and `Xselect` ver. 2.4e. The change in versions appears to be negligible, as discussed later in Chapter 4.4, and thus should not affect these comparisons. We find that stray light emission constitutes less than 0.3% when compared to the total flux from each observation, including background emission. More importantly, it comprises less than 2.8% and 0.5% of the absorbed group emission for NGC 3402 and NGC 5129, respectively. From this, we are confident that stray light does not play a significant role in our observations.

3.2.8 Galactic and Extragalactic Background Variance

Another source of systematic uncertainty in the background modeling involves variance in the Galactic and extragalactic backgrounds. That is, these components vary spatially between the background and group observations. Variations in the X-ray emission from our Galaxy are of more concern than that of extragalactic sources. This is because extragalactic sources become more important in the hard energy band, hence why the more energetic part of the spectrum is crucial to pinning down the power-law component. Therefore, we performed additional analysis regarding the Galactic component. Moreover, although extragalactic sources are less of a concern for our observations, we carried out analysis similar to the methods in Section 3.4 of Bautz et al. [7] to account for this systematic uncertainty.

First, we addressed the Galactic background variance using HEAsoft 6.25 with `Xspec` ver. 12.10.1. Of course, this version was used on all models being fit for this test to ensure an apples-to-apples comparison. Recall that during the course of the background spectral modeling, we characterized the Galactic halo component using a single *apec* model with free temperature and normalization (with an additional *apec* model for the North Polar Spur in NGC 5129). These values were simultaneously fit between all group and background pointings. We will call these models "constrained". To test if significant spatial variations in the Galactic component between background and group observations is present, we allowed the Galactic apec temperature (k_BT_{Gal}) and normalization (k_{Gal}) to be unconstrained between the group and background observations. This means the model was no longer simultaneously fitting the Galactic component between group and background observations. However, we simultaneously fit the NPS *apec* model for NGC 5129 as in the original model. We will call these models "unconstrained".

Comparing the resulting Galactic *apec* temperatures and normalizations within the unconstrained models, we found that the k_BT_{Gal} and k_{Gal} agree well within their 1σ uncertainties for both galaxy groups. Furthermore, those values are consistent within 1σ of the best-fit parameters from the constrained models. Together, this strongly implies that there is no significant spatial variation in the Galactic background between our group and background observations. Perhaps more importantly, we compared the best-fit group *apec* emission temperatures and normalizations between the constrained and unconstrained models. The group k_BT and k were also consistent and within 1σ of each other for both galaxy groups. Taking the difference between the group parameters of the constrained and unconstrained models, we computed the relative uncertainties with respect to the best-fit values. Applying this to the best-fit parameters from the old `Xspec` version, we obtained those systematic uncertainties. These values are: $\Delta\, k_BT_{3402} = 0.018$ keV, $\Delta\, k_BT_{5129} = 0.072$ keV, $\Delta\, k_{3402} = 0.29 \ \times \ 10^{-4}$ cm^{-5} and $\Delta\, k_{5129} = 1.06 \ \times \ 10^{-4}$ cm^{-5}. These differences are less than or on par with the systematic uncertainties from the eight background models discussed in Chapter 3.2.4.

As for the extragalactic variance, we calculated the expected background surface brightnesses (using parameters from Moretti et al. [53], M03) for unresolved point sources (B) in the same way as Bautz et al. [7]. Our results are $B_{M03} = 6.12 \times 10^{-12}$ (0.5–2 keV) erg cm^{-2} s^{-1} deg^{-2} and 1.55×10^{-11} erg cm^{-2} s^{-1} deg^{-2} (2–8 keV). We assume the same limiting flux $S_{excl} = 10S_{14}$ as Bautz et al. [7] for our *Suzaku* observations, since our exposure times and those in Bautz et al. [7] are similar and we do not have XMM-Newton observations to lower that limit. We cross-checked our calculations with Moretti et al. [53] and obtained the same answers given in their Sec. 7.1 and 7.2.

In addition, we used the more recent relations and parameters in Dai et al. [20] (D15, Equation 3 and Swift-all from their Table 11) and obtained $B_{D15} = 3.57 \times 10^{-12}$ erg cm^{-2} s^{-1} deg^{-2} (0.5–2 keV) and 7.04×10^{-12} erg cm^{-2} s^{-1} deg^{-2} (2–8 keV). We compare these values to those derived from the flux of the power-law component in our spectral model fits, divided by the area assumed during the spectral fitting, 400π arcmin^2. Our results lie between (4.44–6.57) $\times\ 10^{-12}$ erg cm^{-2} s^{-1} deg^{-2} (0.5–2 keV) and (1.13–1.56) $\times\ 10^{-11}$ erg cm^{-2} s^{-1} deg^{-2} (2–8 keV) for both galaxy groups. These values correspond extremely well with those we obtained using the parameters and equations in Moretti et al. [53]. They are also consistent within at most a little over a factor of two of the values computed from Dai et al. [20]. Therefore, we can see that the power-law component was properly modeled in our work and we did not under-subtract the extragalactic background.

Chapter 4

Radial Profiles

4.1 AtomDB

The release of the atomic database AtomDB ver. 2.0.2 in 2011 caused significant changes in the derived spectral properties of plasma with $k_B T < 2$ keV, due to updates in the Fe L-shell data; see the Sun [74] review. The major quantity affected for our analysis is the gas temperature, which increased by 10–20% from ver. 1.3 to 2.0 and later versions. This is important to consider, since we are adding our contributions to data derived from older AtomDB versions. To estimate the temperature change in the inner profile, we compared the projected *Chandra* temperature profile of NGC 3402 from Sun et al. [73] (which used AtomDB ver. 1.3.1) to the *Chandra* data reprocessed with CIAO 4.6.1 and CALDB 4.6.2 (post AtomDB ver. 2.0.2, Ewan O'Sullivan, private communication). By determining the vertical shift between temperature profiles and averaging them, we found the temperature measurements increased by 18.6% between pre-AtomDB 2.0.2 and post-2.0.2 analyses (see Figure 4.1). This shift was applied to the subsequent temperature and entropy profiles of the inner data, as well as the global temperatures for these objects, as mentioned in the Introduction. These adjusted temperatures are used repeatedly in our analysis and are indicated as such in the corresponding figures and text.

4.2 Emission Weighted Radius

Since results from the spectral analysis are weighed by emission, we also computed the corresponding radii for each target observation. These emission weighted radii (R_{emw}) were calculated by summing over all distances between each pixel in

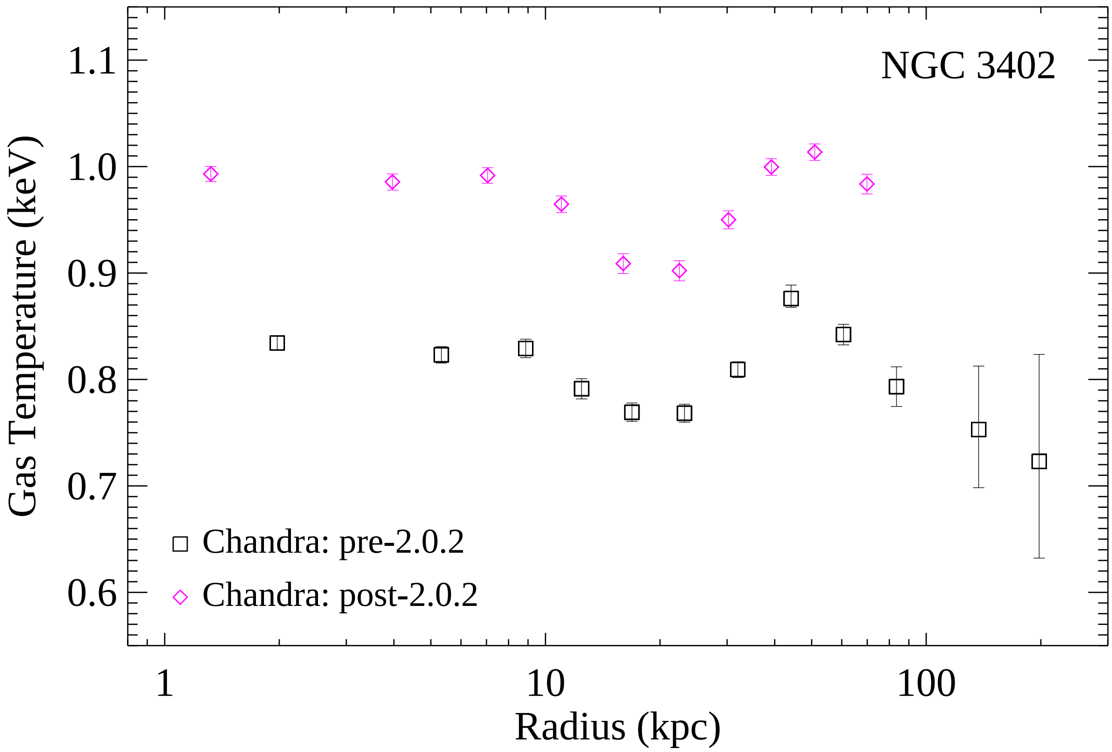

Fig. 4.1.— *Chandra* projected temperature data from the AtomDB version prior to 2.0.2 (black squares) and post 2.0.2 (magenta diamonds) with their 1σ uncertainties.

the extraction region and the group's X-ray center, multiplied by the surface brightnesses at those pixel locations. As discussed below, these surface brightnesses were estimated using a model of the SB profile at the outskirts. Then, we divided by the sum of the SBs at those radii, producing a radius that correlates to the emission weighted center of each observation.

To obtain the surface brightness function for the outskirts of each group, we used data from *Chandra* observations (Sun et al. [73]), as well as the SBs determined from our spectral analysis, adjusted for the *Chandra* detector and energy band (see Chapter 4.4). First, we selected outskirts data such that the cut-off corresponded to the innermost extent of our *Suzaku* observations without extraction regions applied: 200 kpc and 90 kpc for NGC 3402 and NGC 5129, respectively. Next, we fit a power-law using χ^2 minimization to this outer data, allowing the normalization and power-law index to be free. These data include the SBs obtained in this work at the initial central location of each observation, i.e., the center of the largest squares in Figures 2.2 and 2.4. The fits are depicted in Figure 4.2, where they are sufficient considering the data fluctuations and uncertainties.

Furthermore, we approximated a grid of pixels over the extraction region by generating a cleaned event file with the COR2 condition and extraction regions applied. Then, we selected the locations of all events with $k_B T > 2$ keV, effectively excluding the group halo emission. Since the observations are dominated by background emission, this results in a uniform grid of pixel locations. The event files were chosen from the XIS0 observations. Although the extraction regions change between CCDs, we felt this approximation was justified given the quality of the data. From this, we weighed all radii according to the summations mentioned previously. Following this procedure, we iterated the fitting process until the radii converged to be the same by rounding to three significant figures. The subsequent emission weighted radii were $R_{emw} = 375$ kpc for NGC 3402 and 249 kpc for NGC 5129. This corresponds to an average mass over-density of $\Delta = 530$ and 1430 times the critical density of the Universe, for NGC 3402 and NGC 5129, respectively.

Lastly, using the iterated outskirts SB function, we computed a radial binsize based on the locations within which 68% of the total halo emission for each observation is contained, centered on R_{emw}. Specifically, we found the radius at which 16% of all emission within the extraction region was contained and set this as the lower bound. The upper bound was found using the corresponding location within which 84% of emission was enclosed. These binsizes have been overlayed for all radial profiles: Figures 4.3, 4.4, 4.6, 4.8, and 4.10.

4.3 Gas Temperature

Figure 4.3 illustrates the projected temperature profiles for NGC 3402 and NGC 5129 out to R_{530} and R_{1430}, respectively, by combining our outer *Suzaku* data with the inner, adjusted *Chandra* data [73]. Here we have plotted the asymmetric uncertainties originally found through `Xspec` instead of the symmetrized ones used in all other related calculations. Furthermore, we included the projected temperature profile derived from *XMM-Newton* observations of NGC 3402 using AtomDB ver. 3.0 and SAS 13.5 (Ewan O'Sullivan, private communication), based on the work by O'Sullivan et al. [59].

Comparing the *Chandra* and *XMM-Newton* profiles of NGC 3402, we can see an overall agreement between them, where both temperature profiles exhibit "wiggles" that match in radii. O'Sullivan et al. [59] discussed the temperature dip at $\sim$ 10–40 kpc as the possible presence of a "cool core that has been partially re-heated by AGN activity", resulting in a region of warmer gas enclosed within a shell of cool gas. They also discuss the possibility of the shell being due to a recent merger. Laganá et al. [46] supports the latter hypothesis given the nature of their 2D spectral maps of NGC 3402. Their metallicity map shows a clear increase along the southwest to northeast direction in the region of that shell, which they deem can only be the result of merging activity.

Moreover, both the *Chandra* and *XMM-Newton* data show decreases in temperature at $R > 50$ kpc. The *Suzaku* emission weighted temperature at 375 kpc, $k_BT = 0.86 \pm 0.10$ keV, is consistent with the outermost *Chandra* and *XMM-Newton* data points. Our contribution appears to indicate a leveling off of the outer profile as opposed to decreasing, which may also be the result of a merger or perhaps shock heating of infalling material. Yet this should not be overemphasized due to the large uncertainties involved.

In the case of NGC 5129, our *Suzaku* temperature measurement from the 1^{st} observation is also comparable with the outermost *Chandra* data points, albeit slightly larger. However, considering the relatively large uncertainties, it is in agreement with the declining trend of the inner data, typical of a universal temperature profile, e.g., Vikhlinin et al. [78]. In this way, NGC 5129 is far closer to exhibiting the general shape of relaxed galaxy clusters and groups' temperature profiles than NGC 3402.

4.4 Surface Brightness

To obtain the mean surface brightnesses for our spectra, we simulated the group emission using the `Xspec` command *fakeit*. We chose an arbitrary *apec* normalization, then simulated and extracted the count rate (CR) of the fake spectrum in the 0.6–1.3 keV energy range. Under the straightforward assumption that the ratios of CR to *apec* normalization are equal for both the fake and real spectra, we converted to CR for the observed spectrum. Subsequently, the mean surface brightness was computed for each *Suzaku* observation (see Table 4.1).

The projected surface brightness profiles in Figure 4.4 were produced by combining our *Suzaku* measurements at R_{emw} with inner data from the *Chandra* observations in Sun et al. [73]. We have converted the *Suzaku* count rates into *Chandra* ACIS-S 0.7–2.0 keV CRs (same as in Sun et al. [73]) using `WebPIMMS`, which requires input and output energy ranges, as well as parameters such as gas temperature. The temperatures were chosen to be those closest to the best-fit values shown in Table 3.3, while the other fixed parameters were entered exactly as modeled. These converted SBs can be compared to the *Suzaku* SBs in Table 4.1. Our *Suzaku* data expand upon measurements of the surface brightness profiles, especially in the case of NGC 3402, in which the profile is extended by ∼117 kpc. As expected, our

SB measurements are lower than the inner SBs and fall on the declining trends established by the inner data.

Total count rates of the two groups were measured to greater than $0.62\,R_{500}$, by interpolating and integrating the SB profiles. First, we used the IDL *Interpol* function to linearly interpolate between SB data such that there were over 1000 total points. Then, we computed the total CR by summing over the expression $2\pi R\,S(R)$, in which R and S(R) are the interpolated projected radius and surface brightness values. Next, `WebPIMMS` was utilized again to convert the total CRs into unabsorbed fluxes in the 0.5–2 keV band. This conversion required global parameters for the groups including: a $Z = 0.2\,Z_{\odot}$ abundance for both groups [23] and the neutral hydrogen column densities for the center of each group, $N_H = 0.044 \times 10^{22}$ cm^{-2} (NGC 3402) and 0.0176×10^{22} cm^{-2} (NGC 5129).

Combining these parameters with the adjusted global temperatures for each group, $k_B\overline{T}_{3402} = 0.88$ keV and $k_B\overline{T}_{5129} = 0.90$ keV [73], the estimated 0.5–2 keV unabsorbed X-ray fluxes are: $F_{X,3402} = (9.09 \pm 0.20) \times 10^{-12}$ erg cm^{-2} s^{-1} and $F_{X,5129} = (1.790 \pm 0.042) \times 10^{-12}$ erg cm^{-2} s^{-1}. Subsequently, we used `Xspec` to obtain the model normalization that matches these fluxes generated by `WebPIMMS` to calculate the 0.1–100 keV bolometric X-ray luminosities. At this point in the analysis, the version of `Xspec` was ver. 12.10.1 by virtue of updating to HEAsoft 6.25. We tested the impact of this change and found that the difference between former and updated software was negligible. Thus, we used the updated version to determine all subsequent luminosities.

First, the bolometric luminosities are: $L_{Xbol,3402} = (7.00 \pm 0.15) \times 10^{42}$ erg s^{-1} and $L_{Xbol,5129} = (3.157 \pm 0.074) \times 10^{42}$ erg s^{-1}. Also, we extrapolated the bolometric luminosities out to R_{500} and R_{200} by assuming $L_{Xbol,emw}$ is equivalent to the total count rate ($CR_{tot,emw}$) multiplied by some constant. By assuming the same constant for $L_{Xbol,500}$ and $L_{Xbol,200}$, we were able to generate them from their total count rates.

To do this, the SB data including our contribution at R_{emw} were extrapolated by fitting a β-model (discussed further in Chapter 4.5) beyond the radii that began the knee of the SB profile, or $R \geq 100$ kpc for both galaxy groups. Then this model was used to find the SB at R_{500} and R_{200}. The data was interpolated as previously done, including the SB at R_{emw}, out to the extrapolated SBs at either R_{500} or R_{200}. Finally, the CRs were computed as before and the extrapolated luminosities determined.

Furthermore, we found the X-ray luminosities in the ROSAT 0.1–2.4 keV band to be: $L_{ROSAT,3402} = (6.77 \pm 0.15) \times 10^{42}$ erg s^{-1} and $L_{ROSAT,5129} = (3.042 \pm 0.071) \times 10^{42}$ erg s^{-1}. The aforementioned values can also be seen in Table 5.1, where uncertainties in these fluxes and luminosities are from the relative uncertainties in the total count rates. This was done using Monte Carlo simulations, in which 1000 random values were chosen according to a normal distribution within the 1σ uncertainty range for each SB data point, including our *Suzaku* data. Then the 1σ standard deviation was calculated from a Gaussian fit to the resulting total CR distribution for each galaxy group.

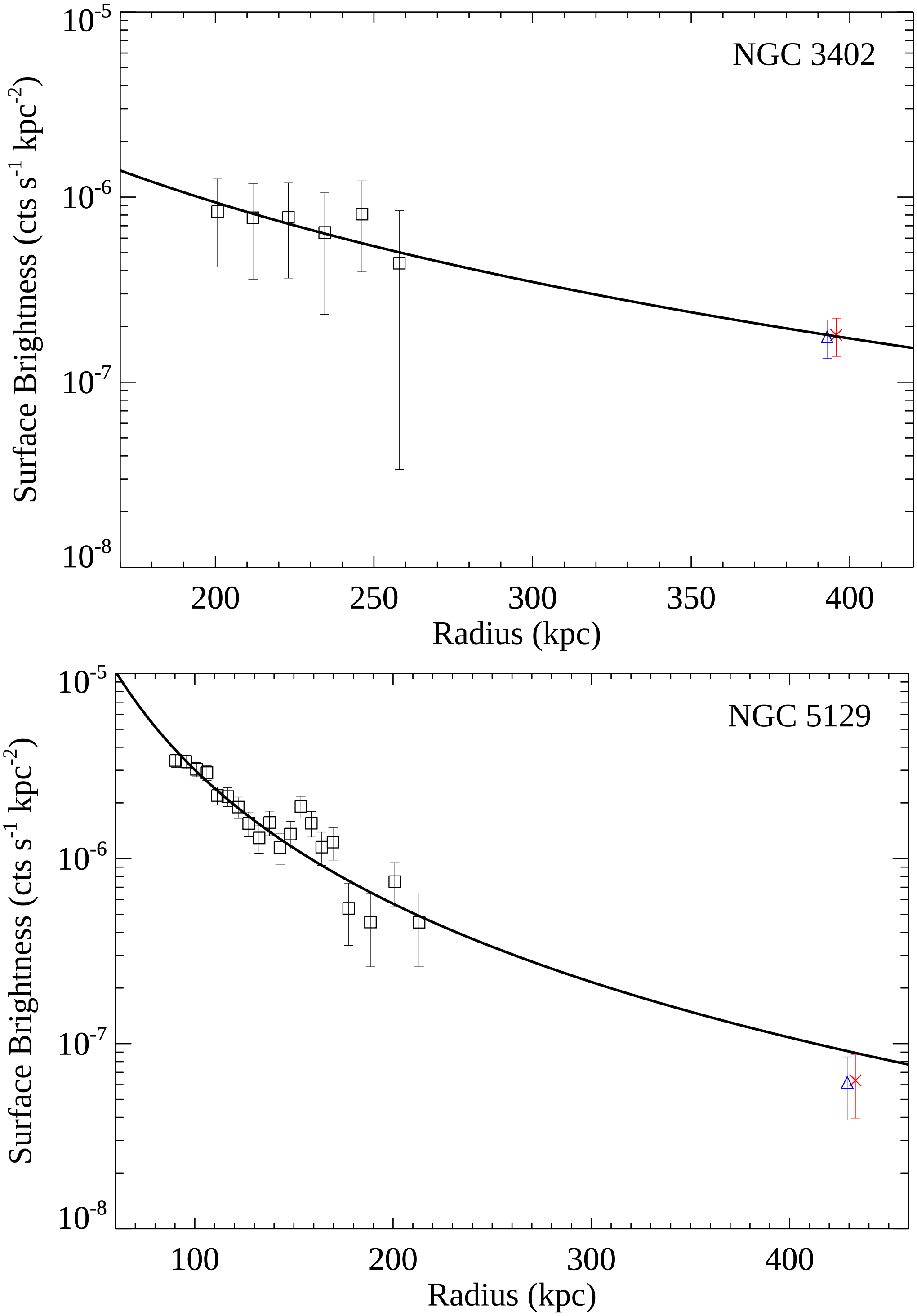

Fig. 4.2.— Projected SB data lying beyond the radii that our *Suzaku* outskirts observations begin (black squares), the SBs obtained from our spectral analysis (red crosses and blue triangles for FI and BI CCDs, respectively) and their 1σ uncertainties, located at the pre-weighted observation center. Black lines are power-law fits to these data.

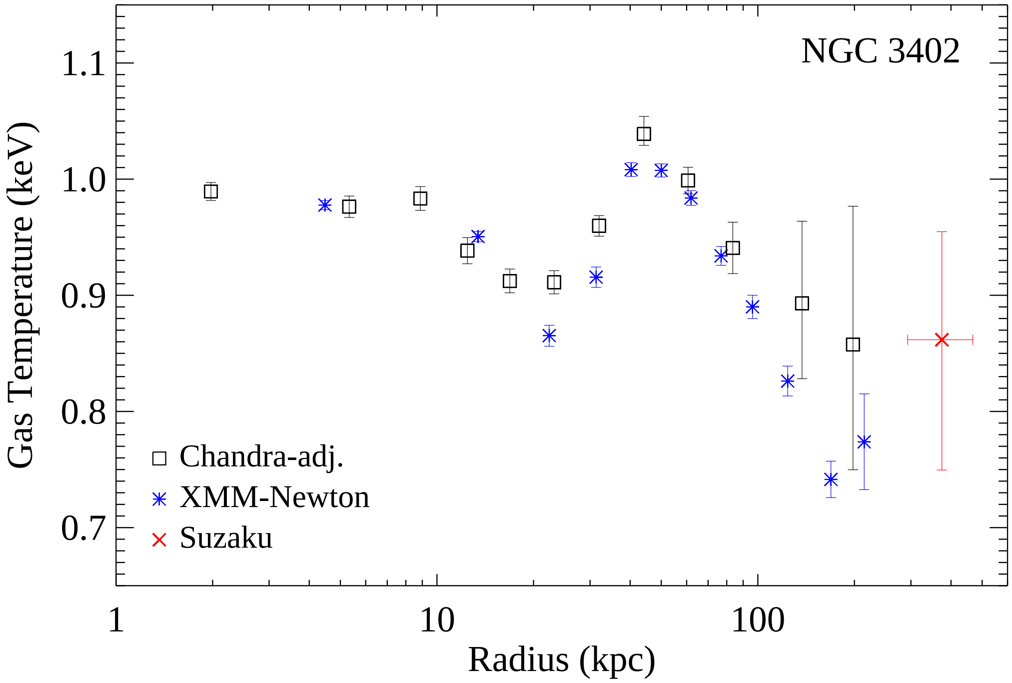

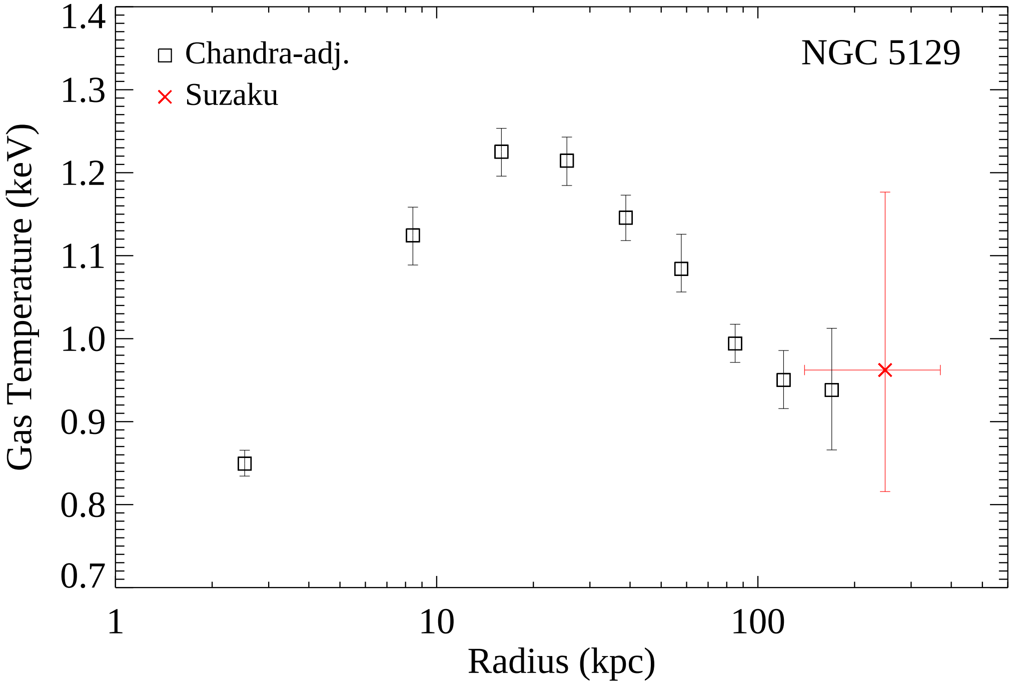

Fig. 4.3.— Projected temperature profiles with 1σ uncertainties in k_BT and emission weighted radial binsizes overlayed. Black squares are *Chandra* data retrieved from Sun et al. [73] and adjusted to AtomDB ver. 2.0.2, blue asterisks are projected XMM-Newton data (Ewan O'Sullivan, private communication) and red crosses are our *Suzaku* values.

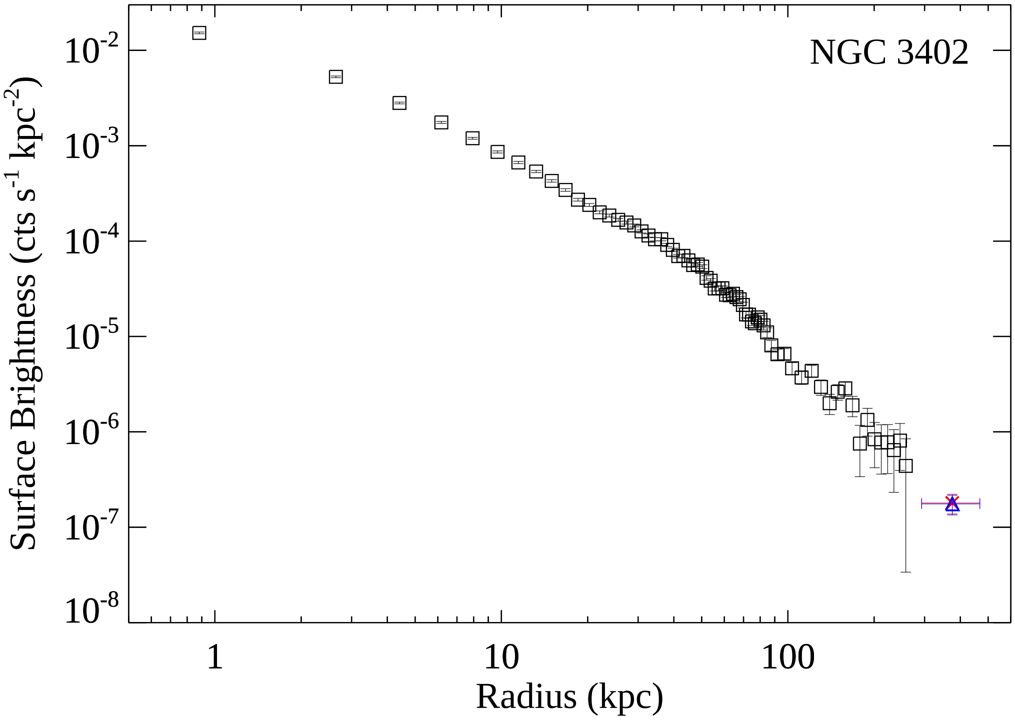

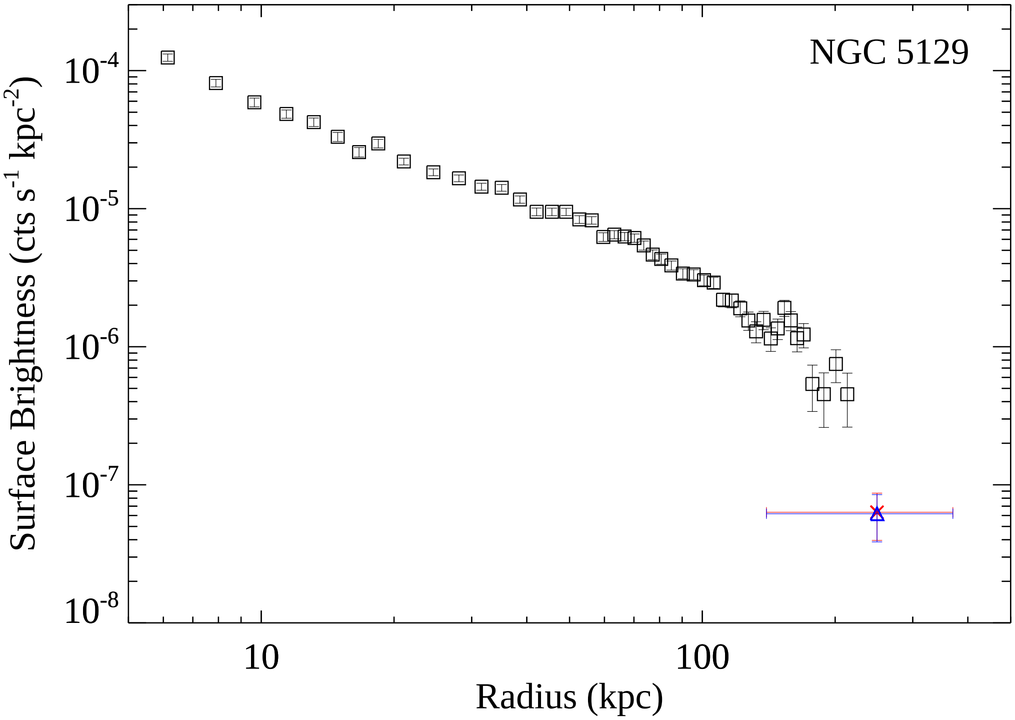

Fig. 4.4.— Projected surface brightness profiles with 1σ uncertainties in SB and emission weighted radial binsizes overlayed. Black squares are *Chandra* data, while red crosses and blue triangles are our *Suzaku* FI and BI data, respectively. Note the surface brightness has not been divided by the effective area of the telescope, which is energy dependent.

Table 4.1. Mean Surface Brightnesses and Electron Number Densities at R_{emw}

Spectral Analysis	FI/BI	Observations	
		NGC 3402	NGC 5129
$S_{0.6-1.3}$ (10^{-8} cts/s/kpc^2)[a b]	FI/BI	3.04 ± 0.71 / 5.4 ± 1.3	1.36 ± 0.51 / 2.41 ± 0.90
$S_{0.7-2.0}$ (10^{-8} cts/s/kpc^2)[a c]	FI/BI	18.0 ± 4.2 / 17.6 ± 4.1	6.3 ± 2.4 / 6.2 ± 2.3
$\Sigma_{0.1-2.0}$ (10^{-10} phot/s/cm^2/arcsec^2)[d]	···	2.16 ± 0.53	1.91 ± 0.77
n_e (10^{-5} cm^{-3})	···	6.55 ± 0.79	14.6 ± 2.8

[a] Note the effective areas of the XISs have not been divided, since they are energy dependent.

[b] This SB is in the 0.6 − 1.3 keV band for the *Suzaku* observations.

[c] The CR used to create this SB has been converted to *Chandra* in the 0.7 − 2.0 keV band.

[d] To match Eckmiller et al. [23], this SB is in the 0.1 − 2.0 keV band.

4.5 Electron Number Density

Following Hudson et al. [35] and Eckmiller et al. [23], the X-ray surface brightness in units of photons/s/cm^2/arcsec^2 at some projected distance on the sky (R) can be expressed in terms of the emission measure along the line of sight, $EM = \int n_e n_H \mathrm{d}l$, by

$$\Sigma = \int_{-\infty}^{\infty} n_e n_H \,\mathrm{d}l \, \frac{\int_{E_1}^{E_2} \Lambda(T, Z, E) \mathrm{d}E}{4\pi(1+z)^4}, \qquad (\mathbf{4.1})$$

where $\Lambda(T, Z, E)$ is the "emissivity function for a plasma of temperature T and metallicity Z at energy E" [35], z is the galaxy group redshift, n_e is the electron number density, and n_H is the number density of hydrogen. Converting to deprojected, three-dimensional radius r and assuming $n_e \approx 1.2 n_H$, since the ratio of the number of H to He is approximately 10% and most electrons come from H and He in these systems [6], Equation **4.1** becomes

$$\Sigma(R) = 2\int_{R}^{\infty} \frac{n_e^2(r)}{1.2} \, \frac{r\mathrm{d}r}{\sqrt{r^2 - R^2}} \frac{\int_{E_1}^{E_2} \Lambda(T, Z, E) \mathrm{d}E}{4\pi(1+z)^4}. \qquad (\mathbf{4.2})$$

Here the *apec* normalization is defined as

$$k \equiv \frac{10^{-14}}{4\pi[D_A(1+z)]^2} \int n_e n_H \mathrm{d}V, \qquad (\mathbf{4.3})$$

where D_A is the angular diameter distance, which can be found using the group redshift. To calculate $n_e(r)$ from Equation **4.2**, we needed to measure the projected surface brightness $\Sigma(R)$ and determine its shape in order to find the final shape of the $n_e(r)$ profile. As discussed below, $\Sigma(R)$ was estimated using data from another work and the Σ at R_{emw} from our *Suzaku* observations through additional spectral analysis. To do this, we first utilized the inner n_e data produced from *Chandra* observations (Sun et al. [73]) to pin down the type of modeling needed to fit the SB profile including our *Suzaku* data.

Most galaxy clusters and groups' X-ray number densities and surface brightnesses can be well described by the class of models called β–models (Bregman [11] and references therein), which assume the gas is isothermal and in hydrostatic equilibrium. In a single β–model assuming spherical symmetry, the electron number density of the gas is parameterized by

$$n_e(r) = n_{e0} \left(1 + \left(\frac{r}{r_c}\right)^2\right)^{-\frac{3\beta}{2}}, \qquad \textbf{(4.4)}$$

where n_{e0} is the central electron number density (the value of n_e at $r = 0$), r_c is the core radius, β is the slope of the density profile typically observed to be ~ 0.5 for groups [55]. Thus, Equations **4.2** and **4.4** reduce to

$$\Sigma(R) = \Sigma_0 \left(1 + \left(\frac{R}{r_c}\right)^2\right)^{-3\beta+\frac{1}{2}}, \qquad \textbf{(4.5)}$$

where Σ_0 is the surface brightness at $R = 0$. This single β–model form is sufficient for many rich clusters, but is overall a poor fit to the emission from groups [55]. To test this, we began with the single β–model and fit the *Chandra* number density data for each group obtained by Sun et al. [73]. Though initially asymmetric, we symmetrized the uncertainties in the *Chandra* data by subtracting the higher bound by the lower bound and dividing by two. Unless otherwise stated, all uncertainties used in the calculation of subsequent quantities and their errors have been symmetrized. Figure 4.5 shows that the single β–model is indeed not a good fit to the group data, especially at large radii where our *Suzaku* observations take place. Therefore, since it is clear that a more complicated model is needed, we chose to use a two component β–model, or a 2β–model. The 2β–model is characterized by the addition of two β–models, each with separate core radii, betas, and central SBs:

$$\Sigma(R) = \Sigma_{01}\left(1+\left(\frac{R}{r_{c1}}\right)^2\right)^{-3\beta_1+\frac{1}{2}} + \Sigma_{02}\left(1+\left(\frac{R}{r_{c2}}\right)^2\right)^{-3\beta_2+\frac{1}{2}} . \qquad (\mathbf{4.6})$$

Now that the need of at least a 2β–model is apparent, we decided to fit the SB profile from Eckmiller et al. [23] (which are their Figures C.19 and C.27), along with our *Suzaku* data. These SB profiles are in units of photons/cm^2/s/arcsec^2, whereas the SBs of Chapter 4.4 are in units of counts/s/kpc^2. Though perhaps counter-intuitive, in the X-ray community both are considered surface brightnesses due to being the number of photons (or counts) per second received from an object per unit area on the sky. The former units take into account the effective area of the detector in cm^2 and convert from counts to theoretical photons received. To include the *Suzaku* data from this work, we used the spectral analysis results for the group emission (Table 3.3), modeled the emission in `Xspec` and found the unabsorbed flux in the 0.1–2 keV band, which is also the band used to derive the SB profile in Eckmiller et al. [23]. This was converted to SB by dividing the area assumed by `Xspec` as the emitting region: $20^2\pi$ arcmin^2 = 400π arcmin^2.

A way to approximate uncertainties in the aforementioned 0.1–2 keV flux and SB is to use a convolution model component in `Xspec` called *cpflux*. From the best-fit spectral models in Tables 3.2 and 3.3, we multiplied this component to the model component for which the photon flux and its uncertainty are desired. In this case, that is the *apec* model for the group emission (excluding galactic absorption) which produces the unabsorbed photon flux. Then that flux was treated as a fit parameter and the *error* command was used to determine its 1σ uncertainty. We also needed to extend the energy range and created dummy response files to obtain the photon flux 1σ range between 0.1–2 keV.

At this point, the software package had been updated to HEAsoft 6.25 with

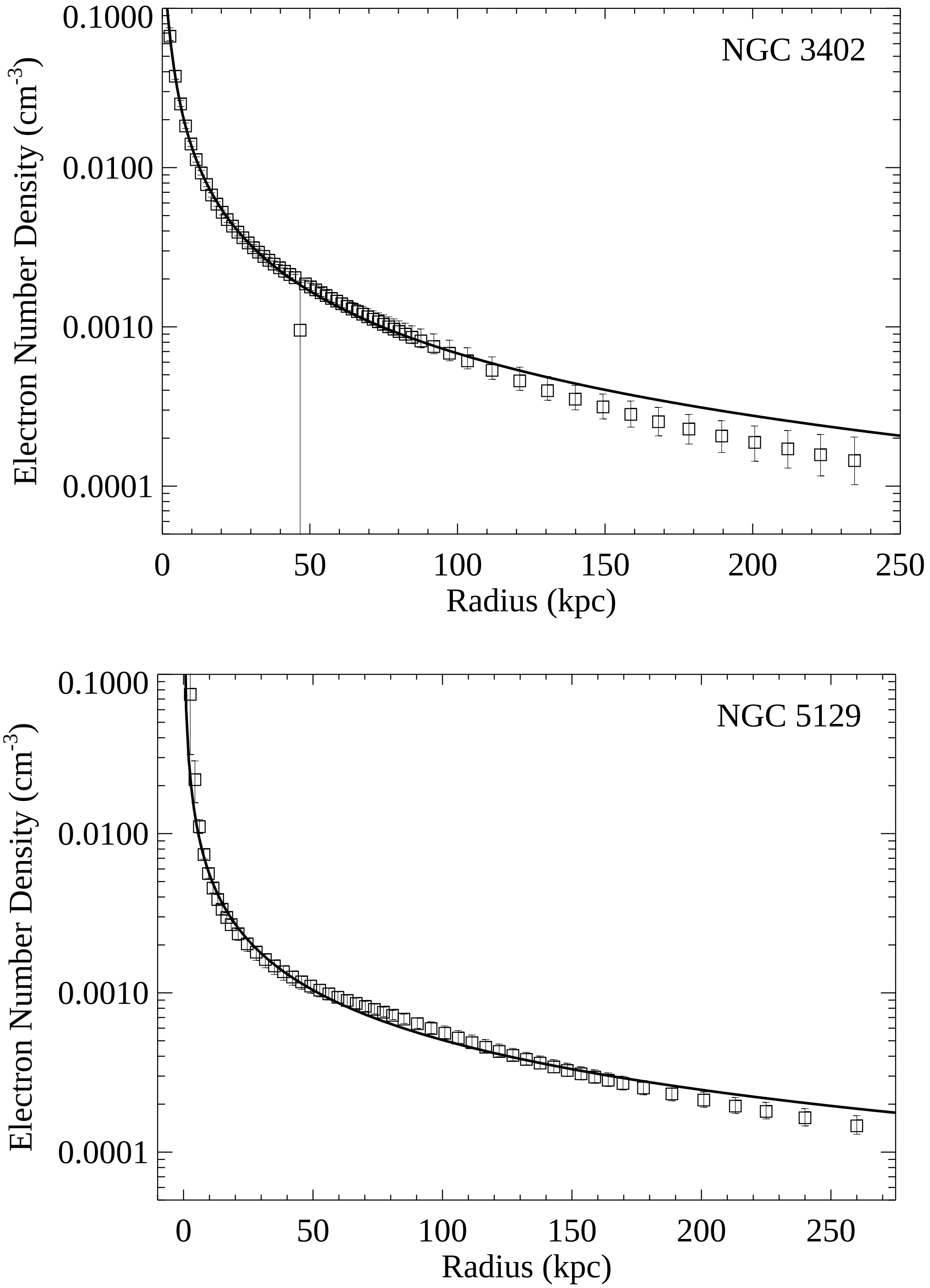

Fig. 4.5.— Single β–model fits (black lines) to the deprojected *Chandra* data from Sun et al. [73].

`Xspec` ver. 12.10.1. This altered the best-fit spectral models somewhat, though not significantly. Yet, we took this change into account by finding the relative uncertainty in the photon flux using the updated version of HEAsoft and applied that to the flux derived from the previous version (HEAsoft 6.13) to obtain its uncertainty. These values were used to determine the following surface brightnesses: $\Sigma_{3402} = (2.16 \pm 0.53) \times 10^{-10}$ photons/cm^2/s/arcsec^2 and $\Sigma_{5129} = (1.91 \pm 0.77) \times 10^{-10}$ photons/cm^2/s/arcsec^2; see also Table 4.1.

After joining these data with that of the inner *Chandra* SBs from Eckmiller et al. [23], we fit 2β–models to the profiles. To perform uncertainty estimation on the best-fit parameters, we fixed each parameter for which the uncertainty was being computed while letting the others vary and calculated the χ^2 over a range of fixed parameter values. This procedure assumes there is no covariance between parameters. The 1σ uncertainty occurs when $\chi^2 = \chi^2_{min} + 1$, i.e., $\Delta\chi^2 = 1$.

However, this revealed degeneracies in parameters, especially in r_{c2} and β_2 for NGC 3402 but also in r_{c1} and β_1 for NGC 5129. They were severely correlated for NGC 3402, resulting in unphysically high values of one parameter while the value of the other increased and still produced $\Delta\chi^2 < 1$. One way to alleviate this is to fix the degenerate core radius to its best-fit value. With that parameter now completely fixed, the other five were allowed to be free, the data re-fit and $\Delta\chi^2 = 1$ uncertainties approximated as initial guesses. This was done for both galaxy groups and, along with switching to brute force uncertainty estimation, brought about reasonable fit parameters and uncertainties.

Our SB profiles visually fit all data very well for NGC 5129, whereas the *Suzaku* data from this work is over 1σ above the best-fit model for NGC 3402. This may indicate that a different model (perhaps a 3β–model) would better fit the data. Results of these fits are shown in Figure 4.6 and Table 4.2, where the minimum χ^2 is larger than ideal considering the degrees of freedom. Nevertheless, a fit solely to the inner data (generated by Eckmiller et al. [23]) produced an analogous χ^2/dof, so we felt justified in proceeding with the analysis. Note that we assume $dof = N - P$, where N is the number of data points and P are the free parameters, five for these fits. However, the degrees of freedom could be as high as $dof = N - 1$ for non-linear models [5], which would improve the reduced χ^2.

Brute force uncertainty estimation involves calculating χ^2 over a grid of parameter ranges for a model chosen to characterize a data set. In this case, that is a 5-dimensional grid of the 2β-model parameter values, where r_{c2} and r_{c1} have been fixed for NGC 3402 and NGC 5129, respectively. The ranges were based on the aforementioned initial $\Delta\chi^2 = 1$ uncertainty estimates, in which the r_c values had been fixed. Using 15 values in each of the five dimensions, we obtained model parameters and their 1σ uncertainties by finding the minimum χ^2 for each value across the entire grid of all other parameters. From that, the $\Delta\chi^2$ for each parameter's range of values was found by subtracting out the global minimum χ^2, then a quadratic was fit to each to determine $\Delta\chi^2 = 1$, i.e., the 1σ confidence interval. Table 4.2 provides best-fit 2β-model parameters with 1σ uncertainties found using this brute force method. See also Figure 4.7, which illustrates quadratic fits to the $\Delta\chi^2$ for each parameter.

Now that the surface brightness model is determined and the parameters have uncertainties, other quantities can be derived such as the n_e profile. For a 2β-model where the SB is in the form of Equation **4.6**, the $n_e(r)$ can be written as

$$n_e(r) = \left[n_{e01}^2 \left(1 + \left(\frac{r}{r_{c1}} \right)^2 \right)^{-3\beta_1} + n_{e02}^2 \left(1 + \left(\frac{r}{r_{c2}} \right)^2 \right)^{-3\beta_2} \right]^{\frac{1}{2}}. \qquad \mathbf{(4.7)}$$

Substituting Equation **4.7** into Equation **4.2** and integrating yields Equation **4.6**, where Σ_{01} and Σ_{02} are related to n_{e01} and n_{e02} by

$$\Sigma_{0i} \equiv n_{e0i}^2 \frac{\int_{E_1}^{E_2} \Lambda(T, Z, E)\mathrm{d}E}{4\pi(1+z)^4 1.2} LI_i. \qquad (\mathbf{4.8})$$

Here LI_i is the line integral defined as

$$LI_i \equiv \int_{-\infty}^{\infty} \left(1 + \left(\frac{l}{r_{ci}}\right)^2\right)^{-3\beta_i} \mathrm{d}l. \qquad (\mathbf{4.9})$$

Combining this with $\Sigma_{12} = \Sigma_{01}/\Sigma_{02}$, Equation **4.7** becomes

$$n_e(r) = \eta \left[\Sigma_{12} LI_2 \left(1 + \left(\frac{r}{r_{c1}}\right)^2\right)^{-3\beta_1} + LI_1 \left(1 + \left(\frac{r}{r_{c2}}\right)^2\right)^{-3\beta_2}\right]^{\frac{1}{2}}, \qquad (\mathbf{4.10})$$

in which $\eta = n_{e0}/\sqrt{\Sigma_{12} LI_2 + LI_1}$ and $n_{e0}^2 = n_{e01}^2 + n_{e02}^2$ is the electron number density at $r = 0$. Finally, n_{e0} can be determined by inserting Equation **4.10** into Equation **4.3**, resulting in

$$n_{e0}^2 = \frac{4\pi 10^{14}(\Sigma_{12} LI_2 + LI_1) D_A D_L 1.2k}{\Sigma_{12} LI_2 EI_1 + LI_1 EI_2}, \qquad (\mathbf{4.11})$$

where D_L is the luminosity distance we found using the group redshift and EI_i is defined as the "emission integral divided by the central [electron] density" [35] and is expressed as

$$EI_i = 2\pi \int_{-\infty}^{\infty} \int_{0}^{R} R \left(1 + \frac{R^2 + l^2}{r_{ci}^2}\right)^{-3\beta_i} \mathrm{d}R\mathrm{d}l. \qquad (\mathbf{4.12})$$

Therefore, $n_e(r)$ can be derived from the fit results of the SB profile (Table 4.2) and the *apec* normalization, k. Since the normalization is being applied to the entire group here, we used the ratio of $\pi R_{emw}^2/400\pi$ instead of the SOURCE_RATIO_REG term. This ensures that the proper emission area is being taken into account. However, this resulted in n_e profiles that were considerably offset from the n_e data in Figure 4.5. This is most likely due to the *apec* normalization derived in this work from the *Suzaku* outskirts observations being applied to the entire group. Nevertheless, Figure 4.8 illustrates that the discrepancy is mostly vertical, when considering uncertainties in the n_e data. Clearly, a calibration must be made to correct for the offset. Also plotted in Figure 4.8 is the full un-calibrated n_e profile obtained using both the SB data from Eckmiller et al. [23] (i.e., the inner SB data) and our *Suzaku* SBs.

Calibrating the profiles involved fitting the inner SB data from Eckmiller et al. [23] and applying the resultant r_{ci} and β_i values in a fit to the inner n_e data from Sun et al. [73]. The parameters allowed to fit freely were the n_{0i} values, since n_{e0} of the n_e profile is what required the calibration. Then, we took the ratio of n_{e0} from that fit to the n_{e0} found by fitting the inner SB data of Eckmiller et al. [23]. Multiplying this ratio to our un-calibrated n_e profile resulted in the corrected curve for NGC 3402 shown in Figure 4.8. This shifted that $n_e(r)$ into complete agreement with the profile used to fit Sun et al. [73]'s data, which we utilized to make the calibration. There is a notch in the data between $r \approx 60 - 140$ kpc that is not taken into account by the adjusted profile, yet it matches well considering uncertainties.

As for NGC 5129, the profile calibrated for n_e at $r = 0$ kpc matched well with data in the innermost radii, then dropped off beyond $r \approx 10$ kpc. Since the vast majority of that profile lies beneath the data, we chose to calibrate the n_e at $r = 100$ kpc instead. This entire profile, save for a small notch that sits above the data between $r \approx$ 5–18 kpc, overlays the data extremely well, especially in the outskirts which is our area of interest for this work. These notches or slight discrepancies are most likely due to the different method used by Sun et al. [73] to derive their $n_e(r)$; see their Section 3.4.

Now that the calibrated electron number density curves have been found, 1σ uncertainties for n_e at the emission weighted radius can be determined. Here we assumed that the deprojected n_e that characterizes our observation is located at the projected R_{emw}, hereafter r_{emw}, which is a conservative placement considering the relationship between deprojected and projected radius. Since we want to probe as much probability space as possible, we produced grids spanning parameter values to at least $\Delta\chi^2 > 6.63$, which encompasses the confidence interval out to 99% for one parameter of interest. This was done for 25 steps in each parameter, which approached the limit of what was computationally feasible using this method. The partial quantity for which we calculated these grids, $n_{e,partial}(r_{emw})$, was the n_e at r_{emw} divided by the square root of the group *apec* normalization. Since the uncertainty in the *apec k* is independent from that of the model parameters, we were able to separate their error estimation. The uncertainty for this partial quantity was later combined with that of our *apec k* using standard propagation of errors, assuming no covariance.

Then, we performed a maximum likelihood estimation method to find the uncertainty in $n_{e,partial}(r_{emw})$. Using the 5-dimensional grid of parameter and χ^2 values, we computed corresponding likelihoods and obtained probabilities, which were binned by $n_{e,partial}(r_{emw})$, giving the probability distribution with respect to $n_{e,partial}(r_{emw})$. The mean values were chosen to be the $n_{e,partial}$ associated with the global minimum χ^2 for the full grid. The 1σ uncertainties in $n_{e,partial}(r_{emw})$ were found by taking the 68% area under the normalized probability distributions, centered on the mean $n_{e,partial}(r_{emw})$. For both groups, these mean quantities were located at the peaks of the largely symmetric distributions. There is slight asymmetry in the distribution for NGC 5129, however, this is to be expected considering the parameter curves in Figure 4.7. The resultant n_e at r_{emw} can be seen in Table 4.1 and the distributions of $n_{e,partial}$ are plotted in Figure 4.9.

To obtain the total number density of the hot gas, we assumed $n\mu = n_e\mu_e$, where μ is the mean molecular weight and μ_e is the mean molecular weight per free electron. Assuming total ionization, $n_e \approx 1.2n_H$ and $\mu \approx 0.62$, $\mu_e \approx \left(X + \frac{1}{2}(Y + Z)\right)^{-1} \approx 1.18$ in which $X = 0.7$, $Y = 0.29$ and the metallicity is $Z = 0.2Z_\odot = 0.004$.

4.6 Entropy

In the astrophysical community, the entropy of the intragroup medium (IGM) is given by $K = k_BT/n_e^{2/3}$, where k_BT is in keV. Technically, this is the term inside the usual thermodynamic entropy per particle equation (multiplied by a constant, C) for an adiabatic, monatomic gas: $\kappa = k_B \cdot \ln CK + \kappa_0$. Here κ_0 is described as a "constant that depends only on fundamental constants and the mixture of particle masses" [81]. Regardless, the former quantity is widely used and called "entropy" because this representation can separate the effects due to gravitational and non-gravitational processes. See Cavagnolo et al. [14] and Voit [81] for more details. Taking into account the overall temperature increase of 18.6% caused by the change in AtomDB, we applied this to the inner entropy profiles of both groups from Sun et al. [73], as seen in Figure 4.10. Also plotted are the data determined from the spectral analysis of the outskirts by this work, where we have used the symmetric uncertainties in the outer n_e and group *apec* k_BT to compute the uncertainty in entropy. These entropies are $K = 530 \pm 76$ keVcm^2 for NGC 3402 and $K = 348 \pm 79$ keVcm^2 for NGC 5129; also see Table 5.1.

There appears to be no tendency for the entropy in either group to drop off or flatten in the outskirts, the latter of which has been observed in clusters [e.g., 30, 34, 42]. In fact, our *Suzaku* data indicate the opposite may be occurring, although this finding is inconclusive considering the uncertainties and radial binsizes in the outskirts. This tendency is more pronounced in NGC 5129, where the outer entropy appears to be significantly higher than the trend of the inner data. Furthermore, we have included in Figure 4.10 the self-similar models, which are the entropy profiles solely due to gravitational processes [$K \propto r^{1.1}$, 84]. We also plotted power-law fits to the data, including the contributions from this work. The best-fit power-law index, Γ, for NGC 3402 was $\Gamma = 0.94$, whereas for NGC 5129 the index was much flatter at $\Gamma = 0.59$.

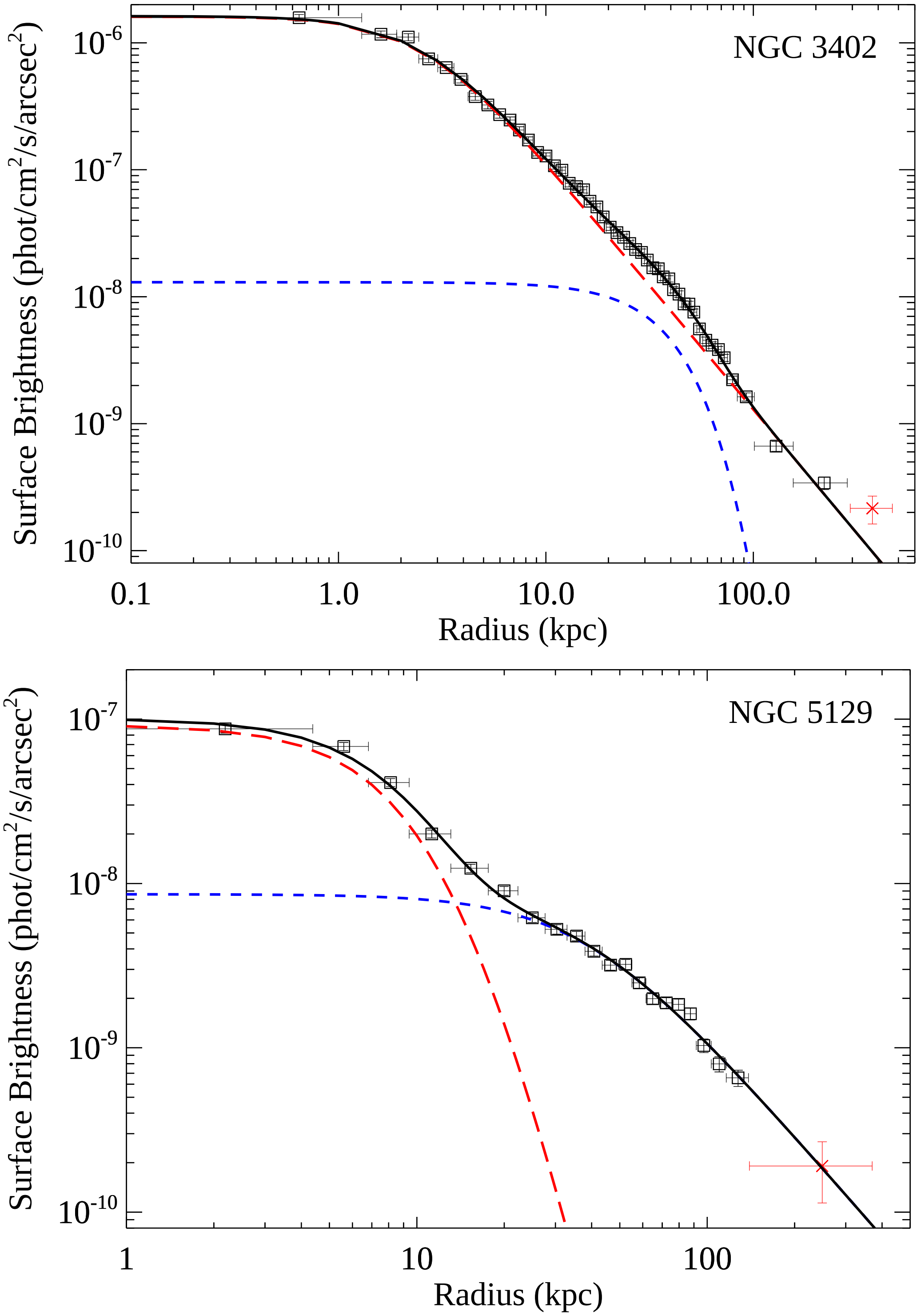

Fig. 4.6.— 2β–model fits to the projected *Chandra* data (black squares) from Eckmiller et al. [23] plus our *Suzaku* data (red crosses). Red and blue dashed lines are the first and second β model components, respectively, while black is the sum of the two.

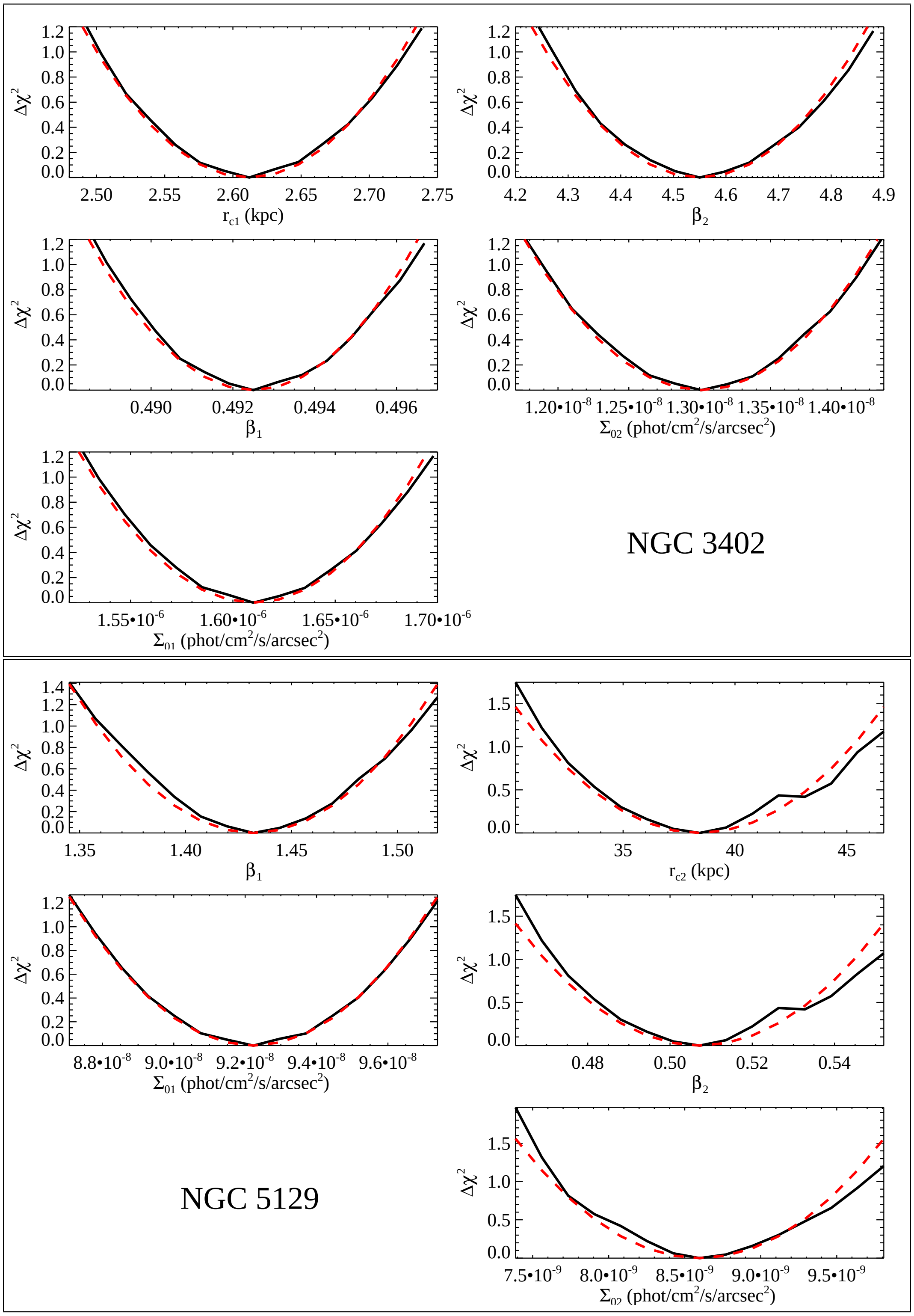

Fig. 4.7.— Quadratic fits (red dashed lines) to the 2β–model parameters (black solid lines) represented via their $\Delta\chi^2$ value over the 5-dimensional grid, from which their 1σ uncertainties were derived.

Table 4.2. 2β–Model Fit Parameters

Model Parameters	Value (inner plus our data) NGC 3402	 NGC 5129
r_{c1}(kpc)	2.61 ± 0.11	14.08
β_1	0.4925 ± 0.0037	1.432 ± 0.074
Σ_{01}(ph/cm^2/s/arcsec^2)	$(1.610 \pm 0.078) \times 10^{-6}$	$(9.22 \pm 0.46) \times 10^{-8}$
r_{c2}(kpc)	138.4	38.4 ± 6.8
β_2	4.55 ± 0.29	0.507 ± 0.038
Σ_{02}(ph/cm^2/s/arcsec^2)	$(1.30 \pm 0.12) \times 10^{-8}$	$(8.60 \pm 0.97) \times 10^{-9}$
χ^2_{min}/dof	56.1/43	26.6/16

Note. — Best-fit parameters for the 2β–model considering inner *Chandra* data and our *Suzaku* contributions. Note the dof could be as high as 47 and 20, respectively.

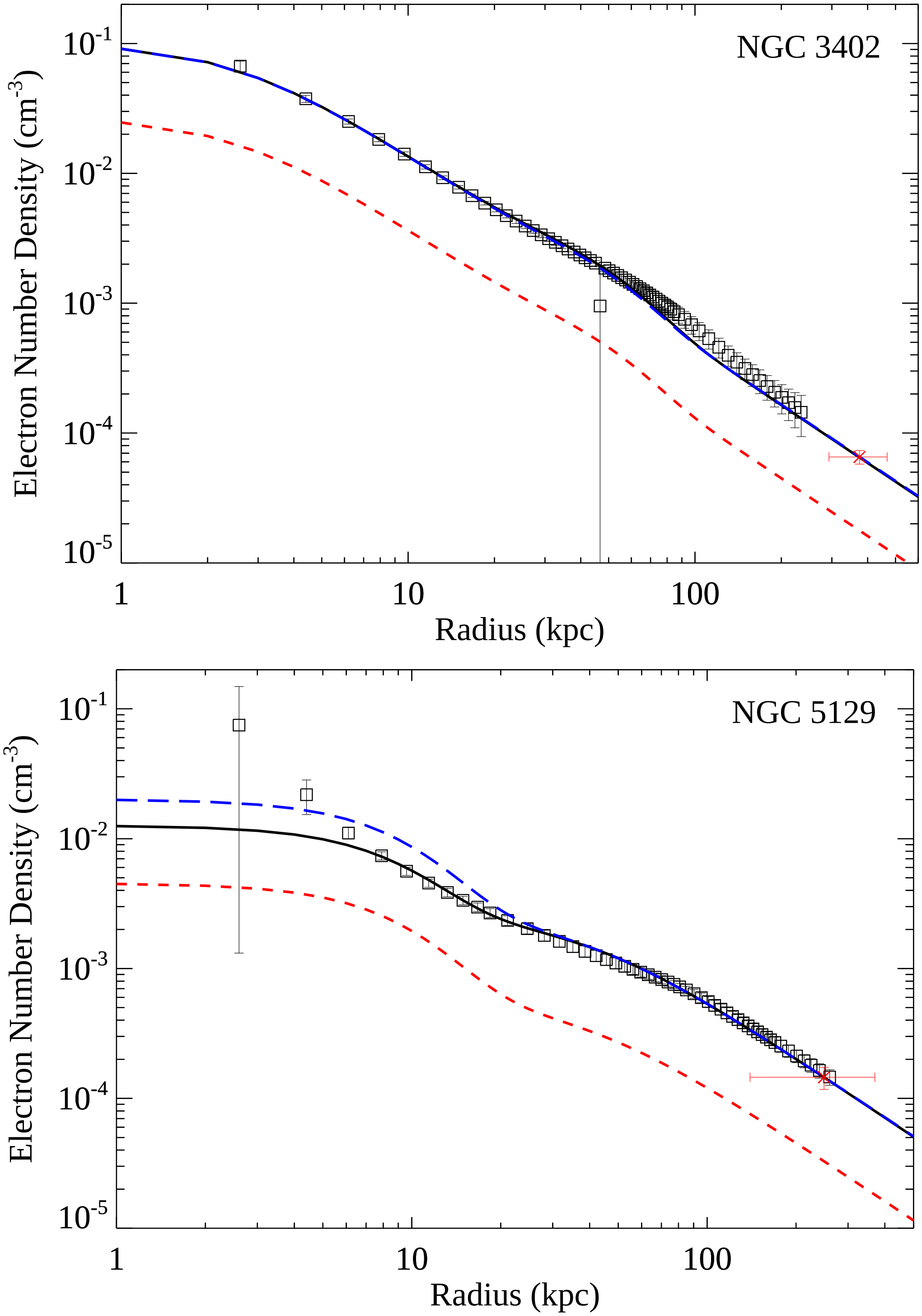

Fig. 4.8.— Sun et al. [73] n_e data (black squares) and our *Suzaku* data (red crosses) with radial bin-sizes plotted. The black line is the constrained fit to the data used to make the calibration, whereas the red and blue dashed lines are the un-calibrated and calibrated profiles for the full SB data set (Eckmiller et al. [23] and *Suzaku*), respectively.

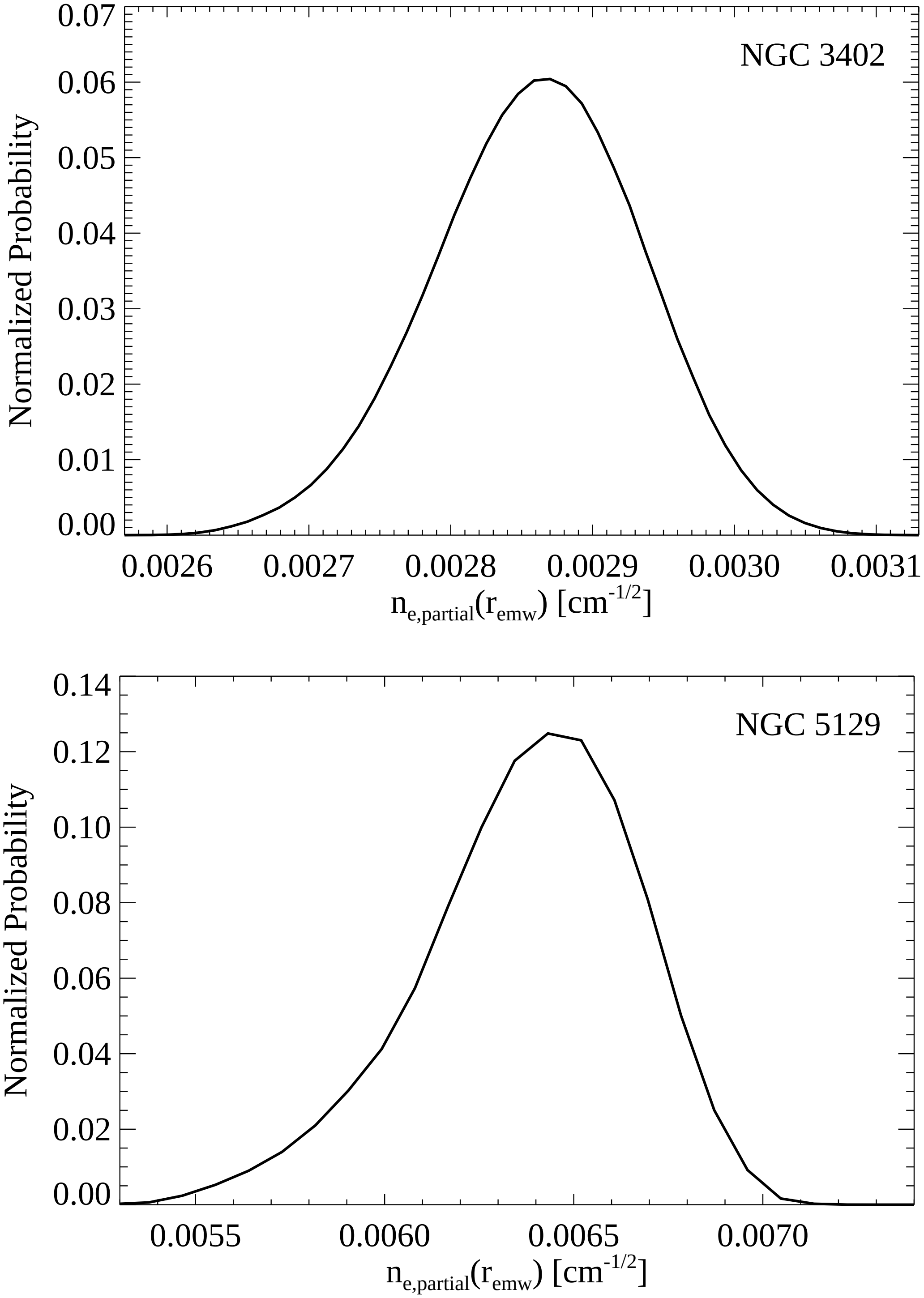

Fig. 4.9.— Normalized probability distributions of the partial quantity for n_e described in Chapter 4.5 at r_{emw}.

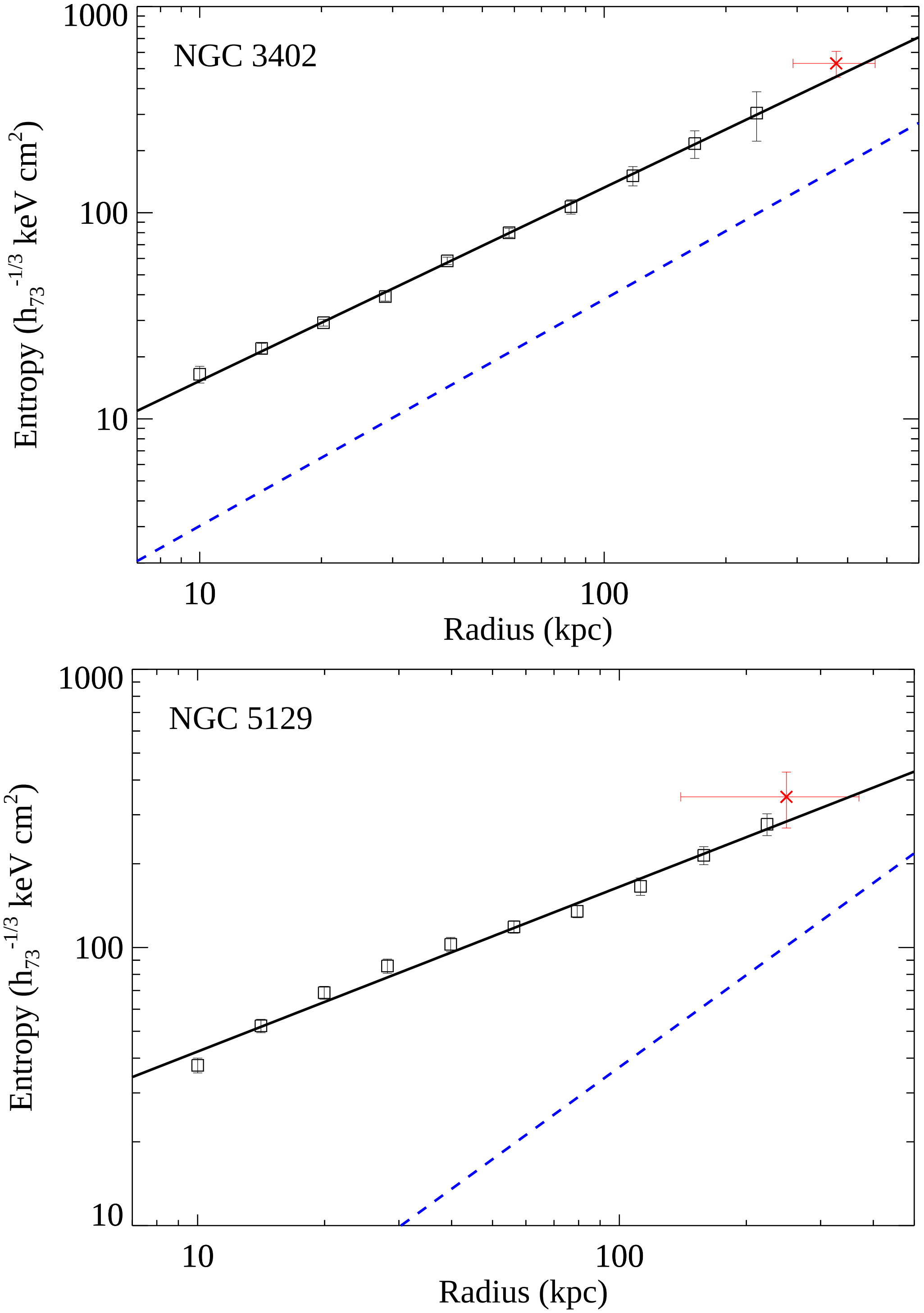

Fig. 4.10.— Entropy profiles in which black squares are Chandra data from Sun et al. [73] (adjusted to the recent version of AtomDB) and red crosses are our *Suzaku* data with radial binsizes overlayed. The solid black lines are power-law fits to the data, whereas the dashed blue lines are the self-similar models as discussed in Chapter 4.6.

Chapter 5

Mass Determination

5.1 Hot Gaseous Halo and Stellar Masses

The gas mass density can be given by $\rho_{gas}(r) = m_p \mu_e n_e(r)$, where m_p is the mass of a proton. Assuming spherical symmetry, we can calculate total gas masses using our 2β–model best-fit parameters out to the emission weighted radii of our *Suzaku* observations. Here we applied the same grid of parameter values and method used to derive the $n_e(r_{emw})$ in Chapter 4.5. In this case, the partial quantity is the gas mass divided by the square root of the *apec k*, since it can be pulled out of the integral. Therefore, uncertainties were found for the gas mass in the same way as $n_e(r_{emw})$. The gas mass for NGC 3402 was $M_{gas,3402} = (9.3 \pm 1.1) \times 10^{11} M_\odot$ and $M_{gas,5129} = (6.1 \pm 1.2) \times 10^{11} M_\odot$ for NGC 5129. Figure 5.1 depicts the normalized probability distributions of the partial quantity representing the gas masses for each group. Similar to the distributions for $n_{e,partial}(r_{emw})$, both are relatively symmetric with the one for NGC 5129 being slightly asymmetric. Again, the peaks of the distributions match with the mean value for $M_{gas,partial}$.

For estimating the stellar mass component of both groups, we used the 2MASS K_s-band apparent magnitude of each member galaxy, since emission in the near-infrared (NIR) is less affected by interstellar extinction and the stellar mass-to-light (M/L) ratios in this band vary relatively little over a large range of star formation histories [8, 9]. To determine the galactic membership, we implemented the SIMBAD Astronomical Database to obtain papers analyzing group membership. For NGC 5129, Mahdavi & Geller [47] found 19 member galaxies out of $N_{obs} = 33$ total galaxies in the observation field. However, NGC 3402 was unique in that there

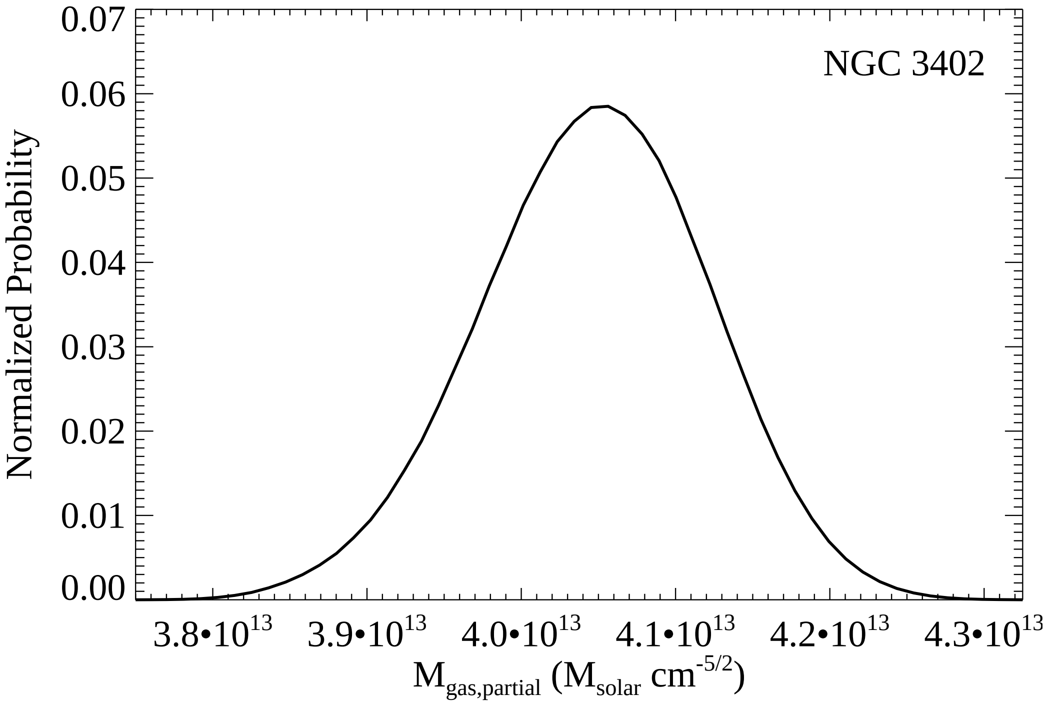

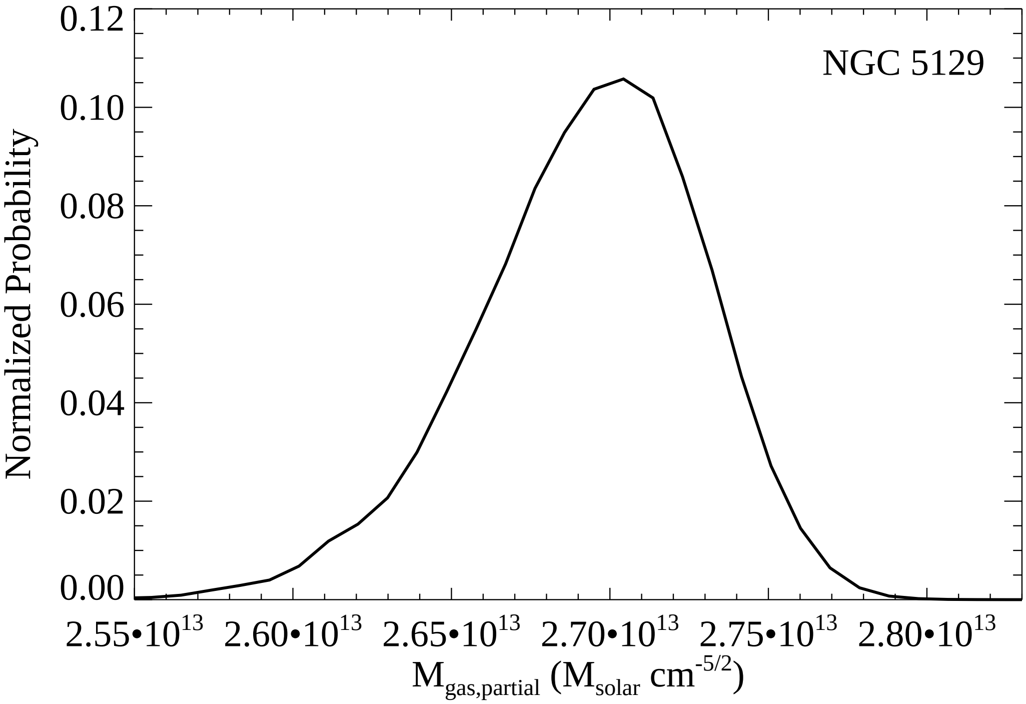

Fig. 5.1.— Normalized probability distributions of the partial quantity used to obtain the gas mass.

were two differing sets of galaxies considered to be possible group members: 6 from Crook et al. [16] and 4 from Guzzo et al. [31]. Two of these galaxies overlap, one being the brightest group galaxy (NGC 3402), which resulted in 8 different member candidates. Using the most current radial velocity data from each paper, we further narrowed down the membership criteria using a redshift cutoff based on the velocity dispersion of the groups. To obtain the velocity dispersion, σ_{disp}, we used the scaling relation for groups and clusters, $\sigma_{disp} = 309$ km s^{-1} $(k_BT/1\ \mathrm{keV})^{0.64}$ [85], where k_BT is the global temperature adjusted for AtomDB as stated in the Introduction. The resulting velocity dispersions were: $\sigma_{disp,3402} = 285$ km s^{-1} and $\sigma_{disp,5129} = 289$ km s^{-1}.

Constraining each galaxy to be within twice that dispersion of its group's radial velocity (redshift times the speed of light), the remaining galactic memberships were: $N_{3402,czcut} = 5$ and $N_{5129,czcut} = 19$, matching the findings in Mahdavi et al. [48] and Mahdavi & Geller [47], respectively. This method is similar to the "sigma clipping" procedure used by Mahdavi et al. [48]. Furthermore, to be consistent with the other mass measurements, we restricted the membership criteria such that each galaxy must lie within r_{emw}. This resulted in $N_{3402} = 4$ and $N_{5129} = 5$. Also, we adopted a stellar K_s mass-to-light ratio of $\Upsilon = 0.9$, in which a 30% 1σ uncertainty inferred from Figure 18 in Bell et al. [9] was applied. Thus, the uncertainty of the mean is $0.3\Upsilon/\sqrt{N}$, where N is the number of member galaxies in each group.

Combining this with the K_s-band apparent magnitudes of each member galaxy (m_K), we simply converted to absolute K_s magnitude (M_{absK}) and then directly transformed to K_s luminosity (L_K), with $M_{absK\odot} = 3.39$ [73] and the K_s solar luminosity of $L_{K\odot} = 4.801 \times 10^{25}$ W. Here we used the standard equations to relate these quantities:

$$M_{absK} = m_K - 5\log_{10} D_L + 5 \tag{5.1}$$

$$L_K = L_{K\odot} \cdot 10^{0.4(M_{absK\odot} - M_{absK})} \tag{5.2}$$

In this case, D_L is the luminosity distance in parsecs and we have ignored the extinction and K-correction terms since they are negligible due to the high Galactic latitudes and very low redshifts of our groups. This resulted in $M_{*,3402} = (2.87 \pm 0.43) \times 10^{11} M_\odot$ and $M_{*,5129} = (7.11 \pm 0.96) \times 10^{11} M_\odot$. As expected, the stellar masses are dominated by the central elliptical galaxies. To illustrate this, composite *J*-*H*-K_s band images derived from *2MASS* Atlas observations are shown in Figure 5.2. Clearly, the brightest group galaxy (BGG) dominates the stellar component for both groups. Assuming a 30% 1σ uncertainty, these masses are: $M_{*BGG,3402} = (2.23 \pm 0.67) \times 10^{11} M_\odot$ and $M_{*BGG,5129} = (3.8 \pm 1.1) \times 10^{11} M_\odot$. In addition, we extrapolated the hot gas and stellar masses for both groups out to characteristic radii, r_{500} and r_{200}. For the stellar masses, we simply extended the distance criteria for the group member candidates out to those radii. These quantities are listed in Table 5.1, along with other mass components and parameters.

The contribution of cold gas is considerably less than that of hot gas in these types of systems. Combining this knowledge with the large uncertainties in the other mass components, the effect of the cold molecular gas is negligible here and is not considered in our analysis.

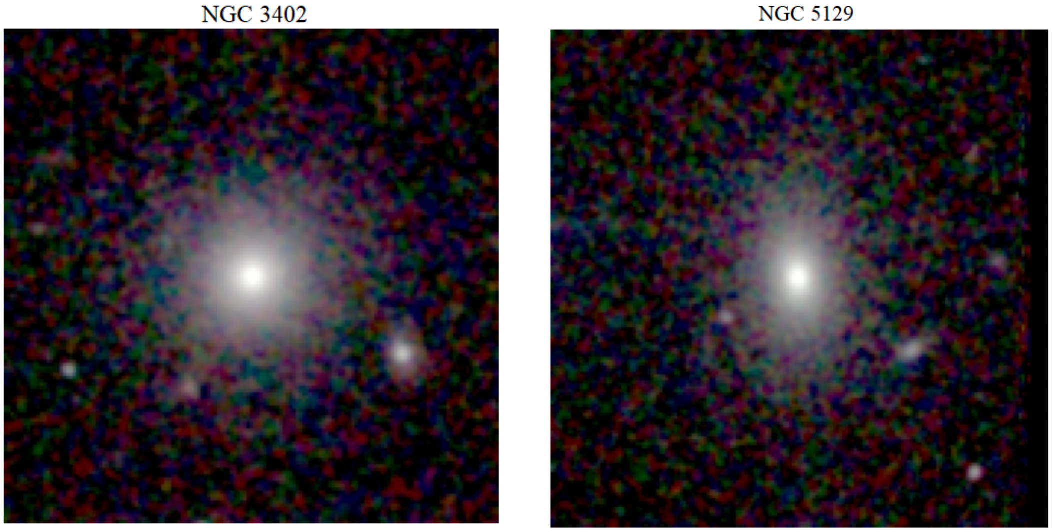

NGC 3402

NGC 5129

Fig. 5.2.— Composite J-H-K_s images of the groups' central galaxies.

5.2 Total Gravitational Mass

Under the assumption of hydrostatic equilibrium, the total mass enclosed within a certain radius (in this case r_{emw}) is,

$$M_{tot}(< r_{emw}) = \frac{-k_B T(r) r^2}{G \mu m_p} \left(\frac{\mathrm{d} ln \rho_g(r)}{\mathrm{d}r} + \frac{\mathrm{d} ln T(r)}{\mathrm{d}r} \right), \qquad (\mathbf{5.3})$$

where G is the gravitational constant and the best-fit 2β–models are used in the first term. Assuming isothermality, the second term in Equation **5.3** is eliminated and the $k_B T(r)$ in the first term is replaced with the adjusted global temperature given in the Introduction. By observing the temperature profiles one can see that assuming isothermality is acceptable for NGC 3402. However, this assumption is not valid for NGC 5129, where it resembles that of a universal temperature profile. Therefore, we utilized a profile from Sun et al. [73], specifically their Equation 5,

$$\frac{T}{T_{2500}} = (1.22 \pm 0.02) - (0.79 \pm 0.04) \frac{r}{r_{500}}, \qquad (\mathbf{5.4})$$

where T_{2500} is the projected temperature with its uncertainty at R_{2500} for NGC 5129, which was obtained from Table 3 in Sun et al. [73] and adjusted for the change in AtomDB. Thus, after applying the 2β-models and $T(r)$, Equation **5.3** becomes

$$M_{tot}(< r_{emw}) = \frac{3k_B T(r) r^3}{G\mu m_p} \left(\frac{\Sigma_{12} LI_2 \xi_1 + LI_1 \xi_2}{\Sigma_{12} LI_2 \zeta_1 + LI_1 \zeta_2} - \frac{s}{T(r)} \right), \qquad (\mathbf{5.5})$$

where s is the derivative of Equation **5.4** with respect to r and

$$\zeta_i = \left(1 + \left(\frac{r}{r_{ci}} \right)^2 \right)^{-3\beta_i} \text{ and } \xi_i = \frac{\beta_i}{r_{ci}^2} \left(1 + \left(\frac{r}{r_{ci}} \right)^2 \right)^{-3\beta_i - 1}. \qquad (\mathbf{5.6})$$

Using the same grid method and parameters to obtain $n_e(r_{emw})$ and M_{gas}, we found the probability distributions for a quantity that included all values except $k_B T(r)$ in Equation **5.5**, called $M_{partial}$ (see Figure 5.3). Yet again, the distributions were symmetric for NGC 3402 and slightly asymmetric for NGC 5129 and the peaks both matched their best-fit mean values. Then, we multiplied this partial quantity with $k_B T(r)$ and performed the usual propagation of errors to determine the error in M_{tot}, including the uncertainties in Equation **5.4**. We obtained total dynamical masses within the emission weighted radii of $M_{tot,3402} = (1.750 \pm 0.013) \times 10^{13} M_\odot$ and $M_{tot,5129} = (1.39 \pm 0.12) \times 10^{13} M_\odot$, which are typical values for poor groups. Furthermore, we computed the total enclosed masses out to r_{500} and r_{200}, as done for many other derived properties (see Table 5.1).

Table 5.1. Derived Group Properties

Property	NGC 3402	NGC 5129
$M_{*,emw}$ ($10^{11} M_\odot$)	2.87 ± 0.43	7.11 ± 0.96
$M_{*,500}$ ($10^{11} M_\odot$)	2.87	7.99
$M_{*,200}$ ($10^{11} M_\odot$)	4.12	10.6
$M_{gas,emw}$($10^{11} M_\odot$)	9.3 ± 1.1	6.1 ± 1.2
$M_{gas,500}$($10^{11} M_\odot$)	9.9	19
$M_{gas,200}$($10^{11} M_\odot$)	30	46
$M_{tot,emw}$($10^{13} M_\odot$)	1.750 ± 0.013	1.39 ± 0.12
$M_{tot,500}$($10^{13} M_\odot$)	1.80	2.05
$M_{200,M-T}$[a] ($10^{13} M_\odot$)	2.95	3.06
$M_{tot,200}$($10^{13} M_\odot$)	2.85	2.63
$f_{g,emw}$	0.0530 ± 0.0063	0.0438 ± 0.0091
$f_{g,500}$	0.0551	0.0911
$f_{g,200}$	0.104	0.175
$f_{b,emw}$	0.0693 ± 0.0068	0.095 ± 0.014
$f_{b,500}$	0.071	0.13
$f_{b,200}$	0.118	0.216
r_{emw}(kpc)[b]	375	249
Δ[c]	530	1430
r_{500}(kpc)	386	402
r_{200}(kpc)	610	593
K_{emw} (keV cm^2)	530 ± 76	348 ± 79
$L_{X,bol,emw}$(10^{42} erg s^{-1})	7.00 ± 0.15	3.157 ± 0.074
$L_{X,bol,500}$(10^{42} erg s^{-1})	7.02	3.23
$L_{X,bol,200}$(10^{42} erg s^{-1})	7.21	3.35
L_{ROSAT}(10^{42} erg s^{-1})	6.77 ± 0.15	3.042 ± 0.071
F_X(10^{-12} erg cm^{-2} s^{-1})	9.09 ± 0.20	1.790 ± 0.042

Note. — All quantities derived are based on $h = 0.73$ and are related to the Hubble constant by $M_* \propto h^{-2}$, $M_g \propto h^{-5/2}$, $M_{tot} \propto h^{-1}$, $L_X \propto h^{-2}$, $\Sigma \propto h^{-1/3}$ and $r \propto h^{-1}$.

[a] This value for M_{200} was derived from the Poisson fit to the M_{200}–T relation in Dai et al. [17].

[b] The r_{emw} here is the emission weighted radius.

[c] Δ is the constant term that when multiplied by ρ_{crit} gives the average mass density of the group.

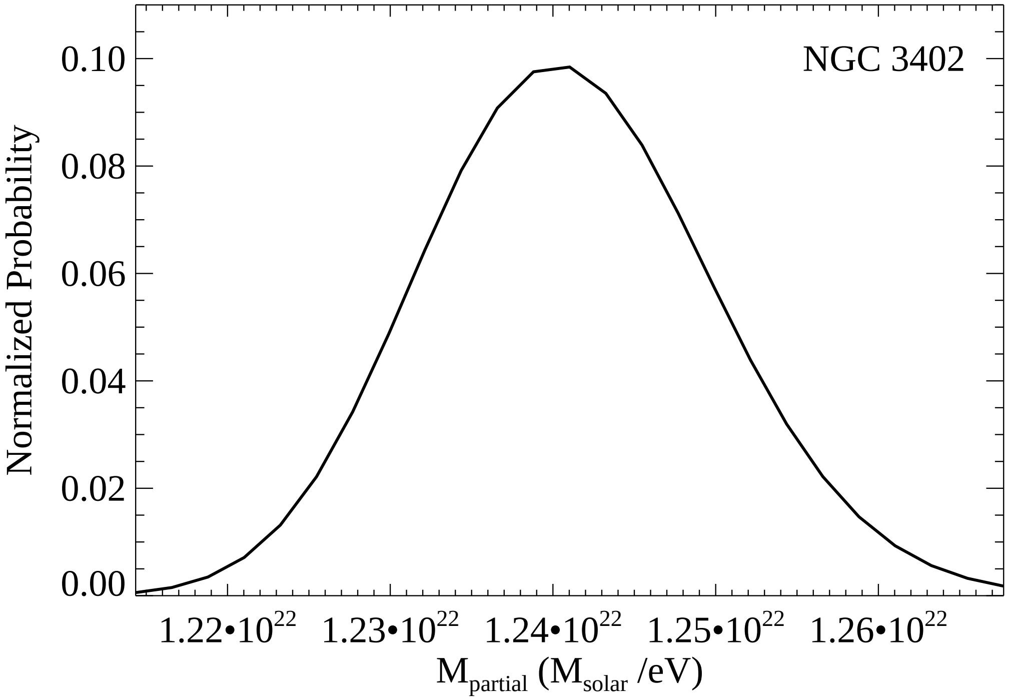

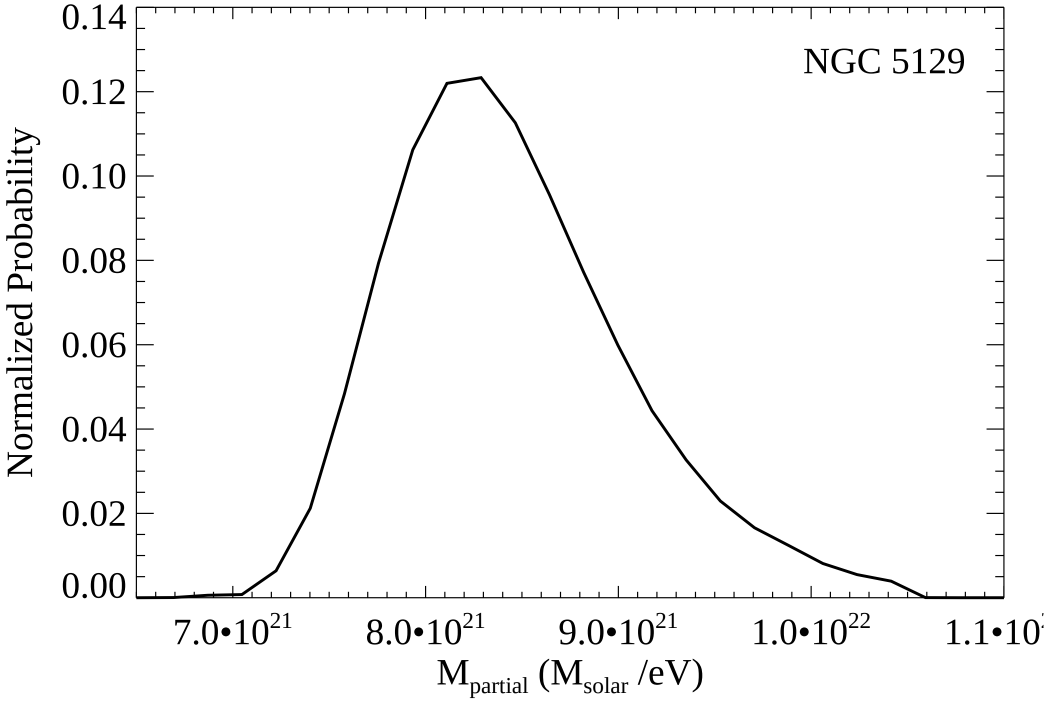

Fig. 5.3.— Normalized probability distributions of the partial quantity used to obtain the total mass (in solar mass/eV).

Chapter 6

Discussion and Conclusions

Using *Suzaku* observations of two low-temperature poor galaxy groups, NGC 3402 and NGC 5129, we measured a range of properties for these groups out to r_{530} and r_{1430}, respectively. These properties include the surface brightness, flux, temperature, electron number density, entropy, gravitational mass and gas halo mass. Thus, we have added NGC 3402 to the small sample of poor groups with well-measured X-ray properties out to approximately r_{500}.

One area of interest lies in how the L_X–T relation differs between galaxy groups and clusters. We first compare the bolometric X-ray luminosities determined in this work for our groups and their global group temperatures to the L_X–T relations of other works in Figure 6.1. Plotted are our data and the relations from Xue & Wu [85], Osmond & Ponman [58], Dai et al. [17] and Sun [74], in which we have adjusted the relations to our cosmology. We plotted the Poisson model fit for Dai et al. [17] and the group fits for the remaining L_X–T relations. The chosen relations were fit based on limited data from galaxy groups and thus vary widely in slope and normalization.

Our data agrees best with the shallow sloped relations by Sun [74] and Osmond & Ponman [58], showing no breaks in the L_X–T relation down to temperatures of 0.9 keV. Therefore, X-ray selected (bright) clusters and groups may show universal scaling relations without breaks. Accurate measurements for even lower temperature groups are needed to test if the L_X–T relation breaks at $T \lesssim 0.8$ keV. The optically selected groups, i.e., Dai et al. [17], have X-ray luminosities below the L_X–T relations established from the X-ray selected groups (all other relations in Figure 6.1). Recently, this was independently measured in the group regime by

Anderson et al. [4].

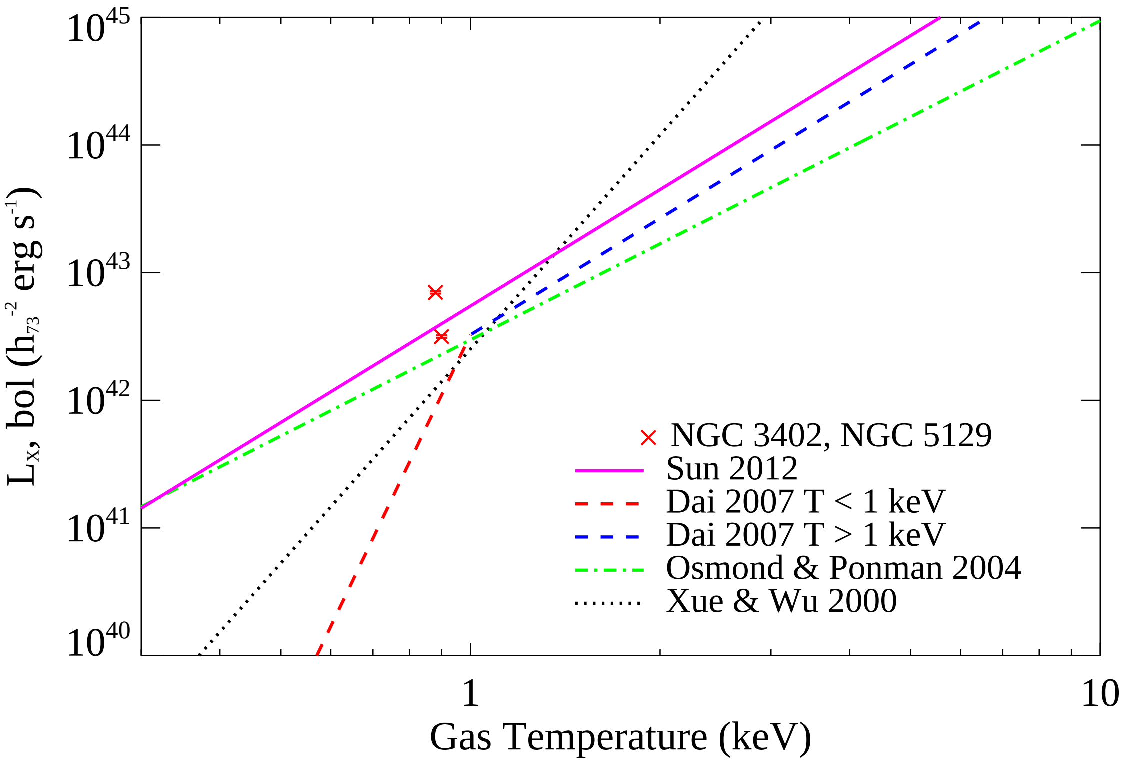

Fig. 6.1.— Bolometric X-ray luminosity (0.1–100 keV) plotted versus global gas temperature for NGC 3402 and NGC 5129, along with their 1σ uncertainties. Also plotted are various L_X–T relations from the literature, corrected for our cosmology.

As for the entropy profiles, one can see that the profile for NGC 3402 lies at nearly a constant value above the $r^{1.1}$ self-similar model [84], representing the entropy purely due to gravitational processes. On the other hand, the profile for NGC 5129 appears to rapidly converge with the self-similar model at large radii. Clearly, the effect of non-gravitational processes dominates in these systems, in the central regions of both groups and beyond for NGC 3402. That is to be expected if NGC 3402 has indeed recently undergone a merger (which would contribute to stellar feedback) or re-heating due to an AGN outflow near the core. Increased energy injection not due to gravitational effects has most likely occurred in the outskirts of this group as well. Possible causes for this excess entropy could be AGN feedback that has reached the outer radii, which has been seen in other groups [73]. As for NGC 5129, the offset in the central regions could also be a product of strong merging or AGN activity, which has radiated vast amounts of energy over its evolution. These results are expected for the significantly weaker gravitational potential wells of poor galaxy groups. Furthermore, the fact that our entropy contributions from this work both lie above the fits instead of flattening out, suggests additional key differences between the group and cluster regimes.

Another property of extreme interest is the baryon fraction. Through normal propagation of errors and assuming no covariances, we combined measurements of the gas, stellar and gravitational masses and obtained the baryon fractions, $f_b = (M_* + M_{gas})/M_{tot}$. Measured out to r_{emw}, we found $f_{b,3402} = 0.0693 \pm 0.0068$ and $f_{b,5129} = 0.095 \pm 0.014$. To compare our data with previous authors' work (Figure 6.2), we first chose to convert Figure 10 in Dai et al. [19] from the circular velocity (V_{cir}) at r_{200} to the total gravitational mass enclosed within r_{200} (M_{200}). This was done to provide a more intuitive representation of the physics. Here we used M_{200} described in terms of the average mass density, $\rho_{ave} = 200\,\rho_{crit}$, where $\rho_{crit} = 3H^2(z)/8\pi G$ is the critical density of the Universe and 200 is the commonly referenced over-density value. Since the objects in Figure 6.2 are relatively low redshift, we used $H(z) \approx H_0$. With this, we rewrote M_{200} in terms of the circular velocity independent of r,

$$M_{200} = \frac{V_{cir}^3}{10 H_0 G}. \tag{\textbf{6.1}}$$

For our data, we generated M_{200} by extrapolating Equation **5.5** out to r_{200} (as mentioned in Chapter 5.2), which we computed from the 2β–model fits. Next, we compared the M_{200} estimates for stacked and individual clusters and our groups with the M_{200}–T relation in Table 3 from Dai et al. [17], $M_{200} = Y_0(T/X_0)^k$, where $logY_0 = 13.58 \pm 0.05$, $X_0 = 1$ keV and $k = 1.65 \pm 0.12$. Many systems, including

NGC 5129, had percent errors from the relation larger than 16%. Thus, we utilized the M_{200}–T relation to approximate the M_{200} values for stacked and individual clusters, as well as our data. Then, we combined all data and fit with a broken power-law model of the same form as in Dai et al. [18, 19],

$$f_b = \frac{0.109\,(M_{200}/6.41\times 10^{13}M_\odot)^a}{(1+(M_{200}/6.41\times 10^{13}M_\odot)^c)^{b/c}}, \tag{6.2}$$

where $a = -0.369$, $b = 0.252$ and $c = 2$ (fixed at a smooth break). Above the break, the baryon fraction, f_b, scales as $f_b \propto M_{200}^{a-b=-0.621}$ and $f_b \propto M_{200}^{a=-0.369}$ below the break. Figure 6.2 depicts the baryon fraction for all systems compiled in Figure 10 of Dai et al. [19], plus our data with the best-fit broken power-law model overlayed. Table 5.1 provides all mass components and baryon fractions for the two groups, as well as their emission weighted radii in familiar over-density forms. Also shown in Table 5.1 are the values determined for the baryon fractions out to r_{500} and r_{200}, along with another useful quantity, the gas fraction, f_{gas}. We derived the gas fraction for our groups out to r_{emw}, r_{500} and r_{200}.

The extrapolated baryon fraction out to r_{200} indicates a significant increase towards the cosmic value for NGC 3402. As for NGC 5129, it reached the cosmic fraction between r_{500} and r_{200}. We further extrapolated the baryon fraction of NGC 3402 to r_{100}, the virial radius for the current cosmology. This resulted in $f_{b,100} = 0.184$, where the stellar, gas and total masses are: $M_{*,100} = 5.91\times 10^{11}\ M_\odot$, $M_{gas,100} = 6.81\times 10^{12}\ M_\odot$ and $M_{tot,100} = 4.03\times 10^{13}\ M_\odot$. Thus, the f_b overtook the cosmic fraction between r_{200} and r_{100} for NGC 3402. These findings strongly imply that much of the expected baryon content lies well outside r_{500} but within the virial radii for these groups. Yet this is solely based on extrapolation and should not be over-emphasized.

To glean a further understanding of the baryon fractions of galaxy groups with

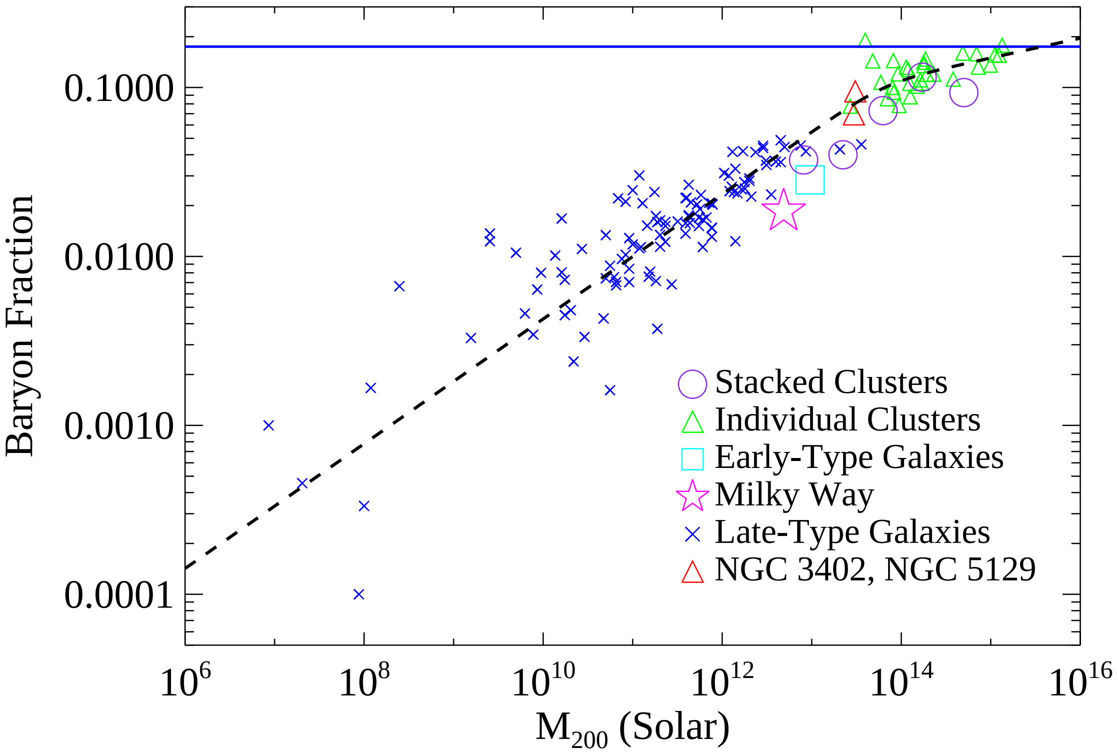

Fig. 6.2.— Baryon fraction as a function of M_{200}, or mass enclosed by r_{200}. Plotted are the measurements from Sakamoto et al. [65], McGaugh [49], Flynn et al. [24], Vikhlinin et al. [79], Gavazzi et al. [29], Walker et al. [82], Stark et al. [72], Sun et al. [73], Dai et al. [18], Anderson & Bregman [3] and this work, converted from circular velocity to M_{200}. The blue solid line is the cosmological baryon fraction measured from the CMB and the black dashed line is the best-fit broken power-law model for baryon losses.

low temperatures ($k_BT \lesssim 1.3$ keV) and measured at large radii, we combined our data with that of a previous work. There are three other groups, all from Sun et al. [73], whose adjusted global temperatures are measured out to a significant fraction of r_{500}. We combined their gas fractions extrapolated or measured out to r_{500} with stellar estimates obtained using the redshift cut-off method used in Chapter 5.1 to determine baryon fractions out to r_{500}. Listed in Table 6.1 are the f_b at r_{500}, global k_BT and measurement radii, where we symmetrized their uncertainties. Then, we plotted these groups with our extrapolated $f_{b,500}$ for NGC

3402 and NGC 5129 and computed the Bayesian average, $\overline{f_{b,500}} = 0.0912 \pm 0.0050$, which is shown in the solid blue region of Figure 6.3. We have made the prior assumption of a Gaussian distribution for the mean $f_{b,500}$ being determined. The averaged $f_{b,500}$ falls significantly below the cosmological value for $\Omega_m = 0.26$ and $\Omega_\Lambda = 0.74$, $f_{b,CMB} = 0.175 \pm 0.012$. For Planck 2018 cosmology, the cosmic baryon fraction is $f_{b,CMB} = 0.157$ [62].

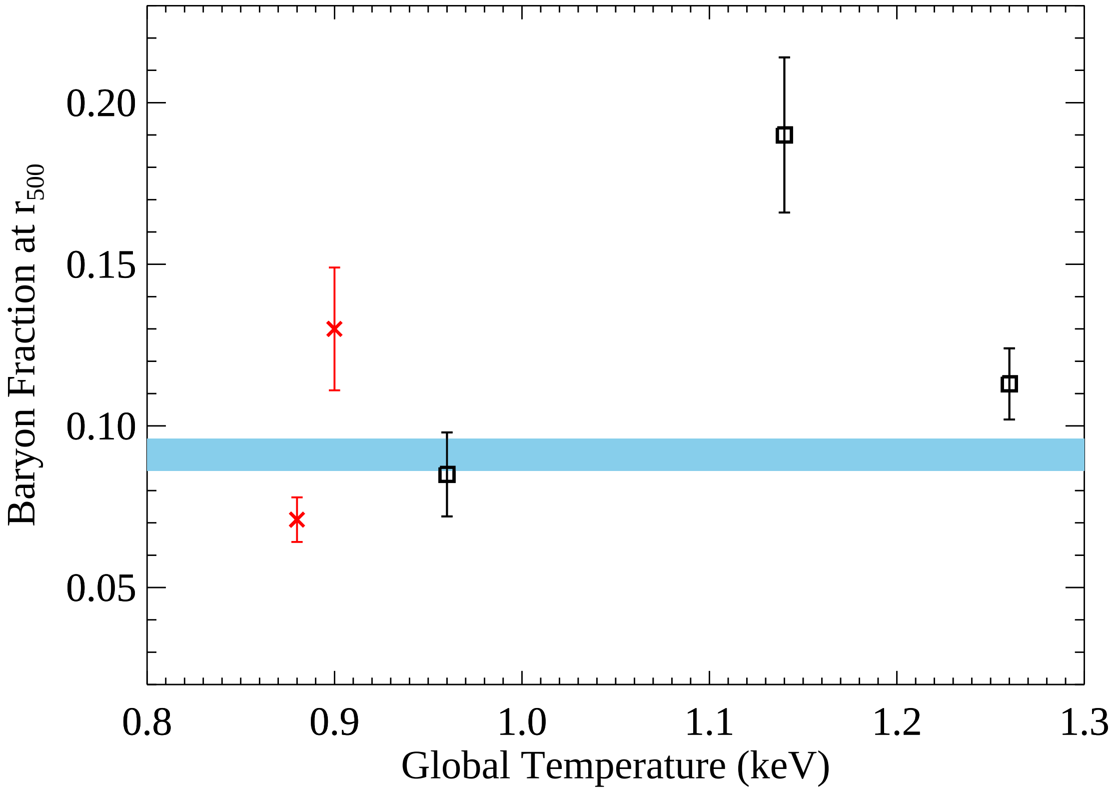

Fig. 6.3.— Baryon fraction out to r_{500} versus temperature, plotted for five galaxy groups with global gas temperatures less than 1.3 keV and whose baryon fractions were determined within $r \geq 0.62\, r_{500}$. The solid blue region is the Bayesian averaged f_b and 1σ uncertainty, whereas the red crosses are the results from this work and black squares are the data from Sun et al. [73].

We conclude that, on average, significant baryon deficits exist for poor groups within r_{500} with temperatures between 0.8–1.3 keV. Other recent studies also found deficits of baryons in galaxy groups, although at higher temperatures of 2–3 keV

[45, 66]. These results reinforce our conclusion that the galaxy group regime is where baryon deficits become significant, insofar as the baryons were able to be detected. Through extrapolation of our mass estimates, we found that our poor groups most likely contain the cosmic proportion of baryons within the virial radius. However, this conclusion is hindered by the radial extent of our measurements and future observations to even larger radii are needed to confirm this assessment.

This sample brings the X-ray community another step closer to understanding key differences between various galactic systems, which in turn should assist in constraining numerical simulations for both cosmology and the formation and evolution of these objects, e.g., Vikhlinin et al. [80], Kravtsov, & Borgani [44] with references therein and Henden et al. [33]. This includes identifying the mechanism for which the missing baryon problem occurs in different systems of galaxies. To achieve this, more outskirts observations of similar systems are needed. In order to improve measurements of the baryon fractions and other derived quantities, we need to observe ever closer to the virial radius. Doing so will better constrain the surface brightness and electron number density profiles, and ultimately the baryon fractions. However, longer exposure times will be needed to improve the photon statistics in such low signal-to-noise regions, along with improvements in instrumentation and data analysis software. Yet, with the end of *Suzaku*'s mission and the tragic loss of its successor, *Hitomi*, this cannot be achieved at present. The planned launch of the X-ray Imaging and Spectroscopy Mission, *XRISM*, in early 2022 is projected to be equipped to fulfill these goals.

Table 6.1. Sun et al. [73] Groups and Properties

Galaxy Group	r_{obs}/r_{500}	f_b	k_BT (keV)
NGC 1550	0.76	0.113 ± 0.011	1.26 ± 0.02
NGC 5098	1.06	0.190 ± 0.024	1.14 ± 0.05
UGC 5088	0.87	0.085 ± 0.013	0.96 ± 0.04

Note. — Properties of the groups measured out to or near r_{500} in Sun et al. [73], adjusted for the change in AtomDB.

References

[1] Akamatsu, H., Hoshino, A., Ishisaki, Y., et al. 2011, PASJ, 63, 1019

[2] Anders, E., & Grevesse, N. 1989, Geochim. Cosmochim. Acta, 53, 197

[3] Anderson, M. E., & Bregman, J. N. 2011, ApJ, 737, 22

[4] Anderson, M. E., Gaspari, M., White, S. D. M., Wang, W., & Dai, X. 2015, MNRAS, 449, 3806

[5] Andrae, R., Schulze-Hartung, T., & Melchior, P. 2010, arXiv:1012.3754

[6] Arnaud, M. 2005, Background Microwave Radiation and Intracluster Cosmology, 77

[7] Bautz, M. W., Miller, E. D., Sanders, J. S., et al. 2009, PASJ, 61, 1117

[8] Bell, E. F., & de Jong, R. S. 2001, ApJ, 550, 212

[9] Bell, E. F., McIntosh, D. H., Katz, N., & Weinberg, M. D. 2003, ApJS, 149, 289

[10] Benson, A. J. 2010, Phys. Rep., 495, 33

[11] Bregman, J. N. 2007, ARA&A, 45, 221

[12] Bristow, P. D., & Phillipps, S. 1994, MNRAS, 267, 13

[13] Bryan, G. L., & Norman, M. L. 1998, ApJ, 495, 80

[14] Cavagnolo, K. W., Donahue, M., Voit, G. M., et al. 2009, ApJS, 182, 12

[15] Cravens, T. E., Robertson, I. P., Snowden, S., et al. 2009, American Institute of Physics Conference Series, 1156, 37

[16] Crook, A. C., Huchra, J. P., Martimbeau, N., et al. 2007, ApJ, 655, 790

[17] Dai, X., Kochanek, C. S., & Morgan, N. D. 2007, ApJ, 658, 917

[18] Dai, X., Bregman, J. N., Kochanek, C. S., & Rasia, E. 2010, ApJ, 719, 119

[19] Dai, X., Anderson, M. E., Bregman, J. N., & Miller, J. M. 2012, ApJ, 755, 107

[20] Dai, X., Griffin, R. D., Kochanek, C. S., Nugent, J. M., & Bregman, J. N. 2015, ApJS, 218, 8

[21] Dickey, J. M., & Lockman, F. J. 1990, ARA&A, 28, 215

[22] Eckert, D., Vazza, F., Ettori, S., et al. 2012, A&A, 541, A57

[23] Eckmiller, H. J., Hudson, D. S., & Reiprich, T. H. 2011, A&A, 535, A105

[24] Flynn, C., Holmberg, J., Portinari, L., Fuchs, B., & Jahreiß, H. 2006, MNRAS, 372, 1149

[25] Fujimoto, R., Mitsuda, K., Mccammon, D., et al. 2007, PASJ, 59, 133

[26] Fujita, Y., Tawa, N., Hayashida, K., et al. 2008, PASJ, 60, 343

[27] Fukugita, M., Hogan, C. J., & Peebles, P. J. E. 1998, ApJ, 503, 518

[28] Gastaldello, F., Buote, D. A., Humphrey, P. J., et al. 2007, ApJ, 669, 158

[29] Gavazzi, R., Treu, T., Rhodes, J. D., et al. 2007, ApJ, 667, 176

[30] George, M. R., Fabian, A. C., Sanders, J. S., Young, A. J., & Russell, H. R. 2009, MNRAS, 395, 657

[31] Guzzo, L., Schuecker, P., Böhringer, H., et al. 2009, A&A, 499, 357

[32] Helsdon, S. F., & Ponman, T. J. 2000, MNRAS, 319, 933

[33] Henden, N. A., Puchwein, E., Shen, S., et al. 2018, MNRAS, 479, 5385

[34] Hoshino, A., Henry, J. P., Sato, K., et al. 2010, PASJ, 62, 371

[35] Hudson, D. S., Mittal, R., Reiprich, T. H., et al. 2010, A&A, 513, A37

[36] Humphrey, P. J., & Buote, D. A. 2006, ApJ, 639, 136

[37] Humphrey, P. J., Buote, D. A., Canizares, C. R., Fabian, A. C., & Miller, J. M. 2011, ApJ, 729, 53

[38] Humphrey, P. J., Buote, D. A., Brighenti, F., et al. 2012, ApJ, 748, 11

[39] Ichikawa, K., Matsushita, K., Okabe, N., et al. 2013, ApJ, 766, 90

[40] Ishisaki, Y., Maeda, Y., Fujimoto, R., et al. 2007, PASJ, 59, 113

[41] Jones, L. R., Ponman, T. J., Horton, A., et al. 2003, MNRAS, 343, 627

[42] Kawaharada, M., Okabe, N., Umetsu, K., et al. 2010, ApJ, 714, 423

[43] Kravtsov, A. V., Vikhlinin, A., & Nagai, D. 2006, ApJ, 650, 128

[44] Kravtsov, A. V., & Borgani, S. 2012, ARA&A, 50, 353

[45] Laganá, T. F., Martinet, N., Durret, F., et al. 2013, A&A, 555, AA66

[46] Laganá, T. F., Durret, F., & Lopes, P. A. A. 2019, MNRAS, 484, 2807

[47] Mahdavi, A., & Geller, M. J. 2004, ApJ, 607, 202

[48] Mahdavi, A., Finoguenov, A., Böhringer, H., Geller, M. J., & Henry, J. P. 2005, ApJ, 622, 187

[49] McGaugh, S. S. 2005, ApJ, 632, 859

[50] Miller, E. D., Tsunemi Hiroshi, Bautz, M. W., et al. 2008, PASJ, 60, S95

[51] Miller, E. D., Bautz, M., George, J., et al. 2012, American Institute of Physics Conference Series, 1427, 13

[52] Mizuno, T., Kamae, T., Godfrey, G., et al. 2004, ApJ, 614, 1113

[53] Moretti, A., Campana, S., Lazzati, D., & Tagliaferri, G. 2003, ApJ, 588, 696

[54] Mori, H., Iizuka, R., Shibata, R., et al. 2005, PASJ, 57, 245

[55] Mulchaey, J. S. 2000, ARA&A, 38, 289

[56] Mushotzky, R. F., Serlemitsos, P. J., Smith, B. W., Boldt, E. A., & Holt, S. S. 1978, ApJ, 225, 21

[57] Nicastro, F., Kaastra, J., Krongold, Y., et al. 2018, Nature, 558, 406

[58] Osmond, J. P. F., & Ponman, T. J. 2004, MNRAS, 350, 1511

[59] O'Sullivan, E., Vrtilek, J. M., Harris, D. E., & Ponman, T. J. 2007, ApJ, 658, 299

[60] Ota, N., Nagayoshi, K., Pratt, G. W., et al. 2014, A&A, 562, A60

[61] Persic, M., & Salucci, P. 1992, MNRAS, 258, 14P

[62] Planck Collaboration, Aghanim, N., Akrami, Y., et al. 2018, arXiv:1807.06209

[63] Reiprich, T. H., Hudson, D. S., Zhang, Y.-Y., et al. 2009, A&A, 501, 899

[64] Rykoff, E. S., Evrard, A. E., McKay, T. A., et al. 2008, MNRAS, 387, L28

[65] Sakamoto, T., Chiba, M., & Beers, T. C. 2003, A&A, 397, 899

[66] Sanderson, A. J. R., O'Sullivan, E., Ponman, T. J., et al. 2013, MNRAS, 429, 3288

[67] Sato, T., Sasaki, T., Matsushita, K., et al. 2012, PASJ, 64, 95

[68] Sekiya, N. 2014, Ph.D. Thesis

[69] Shen, S., Kauffmann, G., von der Linden, A., White, S. D. M., & Best, P. N. 2008, MNRAS, 389, 1074

[70] Simionescu, A., Allen, S. W., Mantz, A., et al. 2011, Science, 331, 1576

[71] Simionescu, A., Werner, N., Mantz, A., et al. 2017, MNRAS, 469, 1476

[72] Stark, D. V., McGaugh, S. S., & Swaters, R. A. 2009, AJ, 138, 392

[73] Sun, M., Voit, G. M., Donahue, M., et al. 2009, ApJ, 693, 1142

[74] Sun, M. 2012, New Journal of Physics, 14, 045004

[75] Takei, Y., Akamatsu, H., Hiyama, Y., et al. 2012, American Institute of Physics Conference Series, 1427, 239

[76] Tawa, N., Hayashida, K., Nagai, M., et al. 2008, PASJ, 60, S11

[77] Truong, N., Rasia, E., Mazzotta, P., et al. 2018, MNRAS, 474, 4089

[78] Vikhlinin, A., Markevitch, M., Murray, S. S., et al. 2005, ApJ, 628, 655

[79] Vikhlinin, A., Kravtsov, A., Forman, W., et al. 2006, ApJ, 640, 691

[80] Vikhlinin, A., Burenin, R. A., Ebeling, H., et al. 2009, ApJ, 692, 1033

[81] Voit, G. M. 2005, Reviews of Modern Physics, 77, 207

[82] Walker, M. G., Mateo, M., Olszewski, E. W., et al. 2007, ApJ, 667, L53

[83] Walker, S. A., Fabian, A. C., Sanders, J. S., & George, M. R. 2012, MNRAS, 424, 1826

[84] Wong, K.-W., Irwin, J. A., Wik, D. R., et al. 2016, ApJ, 829, 49

[85] Xue, Y.-J., & Wu, X.-P. 2000, ApJ, 538, 65

[86] Yamaguchi, H., Nakajima, H., Koyama, K., et al. 2006, Proc. SPIE, 6266, 121

[87] Zabludoff, A. I., & Mulchaey, J. S. 1998, ApJ, 496, 39